TOHOKU
UNIVERSITY

博 士 学 位 論 文

Doctoral Thesis

論文題目/ **Title**

Two-dimensional and Three-dimensional Imaging of Superficial Micro Vessels with Advanced Singular Value Decomposition Filtering of Ultrafast Ultrasound

超高速超音波の先進的特異値分解フィルタリングによる

表層微小血管の 2 次元および 3 次元イメージング

提 出 者　東北大学大学院医工学研究科

医工学専攻

Student /ID NO **C1WD9001**

氏　名/Name **Anam Bhatti**

Supervisor at Tohoku Univ.	Professor Yoshifumi Saijo
Dissertation Committee Members Name marked with "O" is the chief Examiner	○ Professor Yoshifumi Saijo 1 Professor Shin Yoshizawa 2 Professor Kennichi Funamoto

Author's Profile	
Name Anam Bhatti	Date of Birth
Nationality	Citizenship
Curriculum Vitae	
Educational Background	
Work Experience	

Two-dimensional and Three-dimensional Imaging of Superficial Micro Vessels with Advanced Singular Value Decomposition Filtering of Ultrafast Ultrasound

超高速超音波の先進的特異値分解フィルタリングによる

表層微小血管の 2 次元および 3 次元イメージング

A dissertation submitted in partial fulfillment for the degree of Doctor of Philosophy
Graduate School of Biomedical Engineering

by

Anam Bhatti

(ID. No. C1WD9001)

January 2024

Dedication

In the loving memory of my beloved father (Late) Shaman Bhatti

Abstract

Visualization of superficial vasculatures in response to any pathology is crucial for diagnosing skin diseases. The morphology of these vessels is characterized as tortuous and branched structures of different dimensions anastomosed around the diseased tissue. To observe dermis tissue conditions, high-frequency ultrasound (HFUS) has been used, however its limited Doppler sensitivity hampers micro-vessel visualization. This study addresses Doppler sensitivity limitation by using ultrafast acquisition techniques and advanced clutter filtering based on singular value decomposition (SVD) for efficient mapping of micro-flow signal in 2D and 3D imaging fields. A novel region-based SVD clutter filter was proposed to extract blood flow signal with different vascular diameters and densities and blood flow speed in various skin layers. In addition, to visualize superficial vasculatures in multi-dimensional view, a 3D volumetric imaging framework was proposed to scan the imaging area via continuous mechanical translation and extracts the signal via section-wise region-based SVD processing. Post-processing denoising filters such as top-hat and non-local means were implemented to enhance the image contrast. The efficacy of the proposed 2D and 3D imaging frameworks were tested with custom-made micro-flow phantoms that resemble superficial straight and bifurcated micro-vessels. Moreover, *in-vivo* experiments imaged superficial vasculatures in 2D and 3D and visualized micro-vessels of minimum 51 μm in diameter in the dermis layer. This study demonstrated that the proposed approaches have a strong potential to facilitate precise diagnoses of cutaneous diseases.

和文アブストラクト

皮膚疾患の診断には、あらゆる病状に応じた表在血管構造の視覚化が不可欠である。これらの血管の形態は、病変組織の周囲に吻合する、異なる寸法の曲がりくねった分岐構造として特徴付けられる。高周波超音波（HFUS）は皮膚組織の状態を観察するために皮膚科で使用されているが、ドップラー感度が限られているため、微小血管の視覚化が困難である。この研究では、超高速取得技術と特異値分解（SVD）に基づく高度なクラッター フィルタリングを使用して、2D および 3D イメージングにおけるマイクロフロー信号の効率的なマッピングを行うことで、ドップラー感度の制限に対処する。皮膚の各層で血管径、密度、血流速度の異なる血流信号を抽出するため、Region-based SVD clutter filter を新たに提案した。さらに、表在血管系を多次元ビューで視覚化するために、イメージング領域を連続的に機械走査し、部位ごとの領域ベースの SVD 処理を介して信号を抽出する 3D ボリュームイメージングフレームワークを開発した。このフレームワークは、画像のコントラストを高めるための top-hat や non-local means などの後処理ノイズ除去フィルターも実装されている。提案法の性能を、表面微小血管を模擬したマイクロフローファントムで評価したのち、ヒト皮膚の表在血管構造を 2D および 3D で可視化したところ、真皮微小血管で最小直径 51 μm の微小血管の視覚化を実現した。これらの結果により、提案手法の皮膚疾患の精密診断への貢献が強く期待される。

Table of Contents

Chapter 1. INTRODUCTION

Chapter 2. DEVELOPMENT OF AN IMAGING FRAMEWORK TO VISUALIZE SUPERFICIAL MICRO-VESSELS

Chapter 3. FABRICATION OF MICRO-FLOW PHANTOM

Chapter 7. CONCLUSION AND FUTURE PERSPECTIVES

List of Figures

List of Tables

Chapter 1
Introduction

1.1. Background

Microvasculaturs are considered as an important constituent of circulatory system, holding a significant importance[1]. These intricate vessels are tasked with the critical function of supplying oxygen and essential nutrients to the body's tissue-cells while simultaneously aiding in the removal of metabolic waste generated by these cells. Additionally, microvasculature play a key role in fueling both the normal tissues and the diseased tissues such as diseased tissues caused by any inflammatory or malignant diseases. These deformed tissues such as cancerous tissues persistently grows under nutrients supply from surrounding healthy tissues and vasculatures in any malignancy results in metastasis (progression of cancer) of diseases, which unfortunately contributes to the severity of the cancer in patients. Due to the widespread distribution of vasculatures in the circulatory system, these vessels are responsible for nourishing nearly every organ in the body[2]. Any deviations from the normal growth and appearance of these vessels can result in a multitude of diseases. For instance, in largest organ of human body which is skin, an insufficient growth or maintenance of vasculatures in superficial cutaneous layers can lead to various skin disorders such as vasculitis (remodeling of vasculatures)[3], Raynaud's phenomenon (narrowing and occlusion of vasculatures)[4], and malignant melanoma (angiogenesis)[5]. Skin and subcutaneous diseases are highly prevalent and represent a significant contributor to global disease morbidity.

According to a survey on the global burden of diseases (GBD)[6], there was a substantial 46.8% increases in the prevalence of skin diseases between 1990 and 2017. These conditions now rank fourth in terms of incidence among all disease categories[7]. In the Fig1.1[8], provided the Disability Adjusted Life Years (DALYs) report which illustrates a comparison of various skin diseases across different age groups. It highlights that dermatitis is responsible for the most substantial global burden in terms of disease impact. Furthermore, as individuals age, the incidence of skin cancers such as keratinocyte

carcinoma and melanoma also rises. In Japan, an epidemiological study[9] focusing on different types of skin cancer reveals that older individuals, aged 55 – 95 years, are more susceptible to skin cancer compared to individuals with other age group. Skin melanoma ranks as the third most common form of cutaneous malignancy. It involves an abnormality in melanocytes, which are located in the basal layer of the epidermis and are responsible for producing melanin, the pigment that imparts color to the skin[10]. In the progression of tumor development, malignant melanocytes cells undergo metastasis, leading to the formation of new blood vessels (angiogenesis) derived from the existing vascular network to nourish the tumor. As melanoma extends into the dermis layer, it causes deterioration of the surrounding tissue and the cutaneous vascular network. Detecting melanoma at an early stage is crucial for preventing its spread, as it can help to reduce the adverse consequences of the disease and hinder its progression.

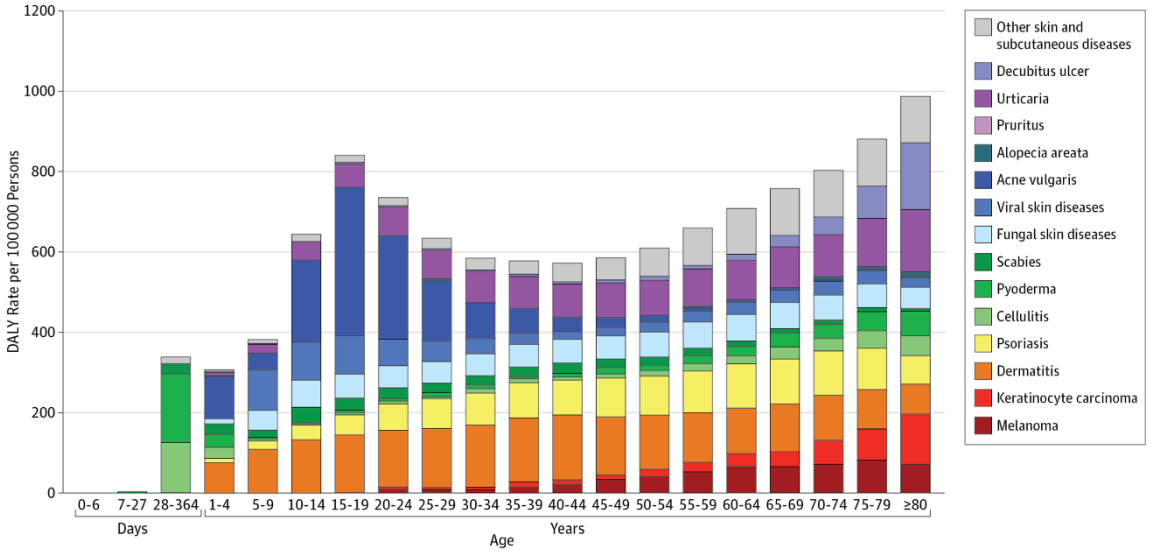

Fig. 1.1. Age Distribution of Skin and Subcutaneous Disease Burden This figure shows disability-adjusted life year (DALY) rate per 100 000 persons from 15 skin disease categories throughout the human life span. Source [8] © JAMA.

Regular examination of skin is conducted mainly by optical imaging modalities such as OCT, dermatoscope, and magnifying mirrors[11]. These clinical methods are well-suited for diagnosing surface level skin conditions. However, when it comes to observing the deeper layers of the skin to assess cutaneous disorders and pathologies, the traditional

approaches involves invasive skin excisional biopsies are commonly performed. However, this method has certain limitations that often results in inconclusive disease diagnosis. These limitations include inadequate tissue sampling and a lack of comprehensive information about the *in-vivo* biopsy sample and the surrounding tissue[12]. These challenges underscore the need to develop more advanced and non-invasive imaging techniques for improved diagnosis of the deeper skin structures.

1.1.1. Anatomy of skin and blood vessels

In vivo healthy human skin consists of three primary layers[1]:

Epidermis: It is the outermost layer of the skin, typically 0.06 – 0.6 mm in thickness, provides protection to the inner layers from germs and makes it difficult for bacteria and viruses to enter in the body.

Dermis: It is the intermediate and thick layer of skin, typically 1 – 4 mm in thickness and comprises fibrous and connective tissues below the epidermis containing sweat glands, hair follicles, nerve endings and blood capillaries.

Hypodermis/Subcutaneous tissue: It is the deepest section of the skin typically 5 – 20 mm in thickness and comprised mainly adipose tissues. Larger blood vessels and nerve endings are found in this layer of skin which is hypodermis.

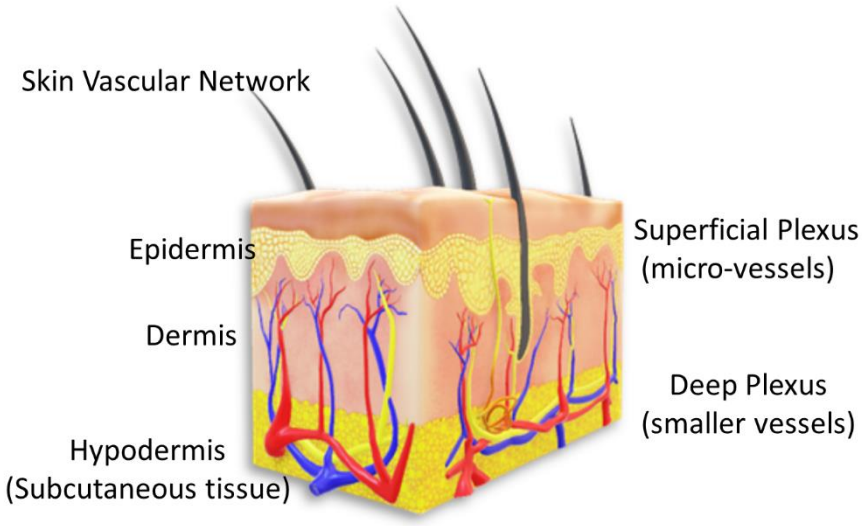

Fig. 1.2. Representation of skin layers: epidermis, dermis, and subcutaneous

The blood vessels in skin are mainly found in the dermis and hypodermis layer of the skin. There are three major types of blood vessels. Arteries: which carries blood away from the heart. Veins: which carries blood back to the heart from different body parts. Capillaries: these are the smallest vessels which help to exchange oxygen, water, waste substances, and other nutrients between the blood and tissue.

Microvascular circulation has been defined as the circulation of blood within arterioles less than 300 μm in diameter, adjoining capillaries, and subsequent venules. Vascular network in skin consists of two primary plexuses: the superficial primary papillary plexus, which is located in the papillary dermis and serves the above epidermis layer comprised on arterioles (10 – 100 μm), capillaries (8 – 10 μm), and venules (10 – 200 μm), and the second a more substantial one is reticular plexus located at the junction of the dermis layer and the hypodermis layer of skin to provide the blood to the hair follicles and the sweat glands.

1.1.2. Ultrasound imaging of skin

Medical ultrasound has been recognized as one of the non-invasive imaging technique in clinical medicine for several decades[13]. Its significance in medical research, particularly gained widespread used imaging tool in general medicine around 1950, its application in dermatology was officially recognized in 1979[14,15]. In clinical diagnostic ultrasound imaging, a center frequency typically ranging from 3-7 MHz is commonly used to visualize the internal structures in the human body. However, when it comes to ultrasonography of superficial parts or skin, high-frequencies exceeding 7 MHz are required to observe the morphology and internal structures such as different layers of the skin and the subcutaneous tissues. Mainly in skin imaging, high-frequency ultrasound (HFUS) has privileged itself from other non-invasive imaging modalities due to its higher resolution, easy to use and in-depth imaging capabilities. It excels at visualizing the various layers of the skin, including its morphology and subcutaneous structures in deeper regions of skin[16]. HFUS is also instrumental in examining the diseased tissues as morphology of tumor and assessing the inflammatory response associated with various pathological conditions[17]. Also, HFUS is characterized by its higher spatial resolution

which can effectively delineate the structural details of the skin through B-mode imaging. However, when dealing with pathological abnormalities due to some disease, mere morphological information may not suffice to fully understand the underlying cause. Therefore, the visualization of vascularization becomes crucial for both diagnosing the disease and assessing the effectiveness of the proposed treatments[18]. For example, skin conditions like Raynaud's phenomenon, a rare arterial disorder affects the skin due to narrowed blood vessels in the fingers. Observing these affected vasculatures could benefit in earlier and proper diagnosis of this disease which might reduce the adverse events of the diseases. Likewise, observing angiogenesis responses during tumor development also aides in the early diagnosis and prognosis of skin cancer.

Doppler ultrasound is a widely used ultrasound imaging technique for assessing blood flow signals, offering valuable insights into the dynamics and structure of blood vessels. It provides various modes for characterizing flow, including color Doppler, power Doppler, and spectral Doppler. These methods harness the Doppler effect, which encompasses alterations in the transmitted frequency relative to the received frequency of ultrasound[19]. This shift in frequency, referred to as the Doppler shift, is instrumental in determining both the speed as well as the direction of blood flow within the vessels. In the process of mapping the blood flow signal, ultrasonic pulses are directed through the blood vessels, while echo signals are captured through the backscattering of these pulses by red blood cells. The flow signal originating from red blood cells is analyzed by observing the temporal variations present within the successive backscattered signals during each pulsed emission. The sensitivity of Doppler ultrasound primarily relies on the number of temporal samples acquired during each event to detect the flow signal accurately. Specifically, for mapping micro-circulation in micro-vessels and detecting slow-moving blood flow signals, higher sensitivity of Doppler ultrasound is required[20]. Traditionally, Doppler ultrasound has exhibited limited sensitivity in mapping microcirculation due to its conventional line-by-line signal acquisition approach. In this method, focused pulse waves are transmitted, and backscattered echoes are received from a single line within the imaging area. The entire imaging area is sequentially scanned by the focused beam to construct a complete image. However, this sequential line-by-line acquisition results in a restricted number of acquired temporal frames and at constrained

acquisition time for gathering a few frames per line across the entire imaging area. Resultantly, in the conventional Doppler sequence, the imaging field is partitioned into several blocks, each having a limited number of temporal frames. Each block undergoes scanning a few times at a specific sampling frequency before moving to the next block within the imaging area. This process yields acquisition of asynchronized signals between each block of the imaging area, coupled with a limited number of Doppler frames, ultimately leading to reduced Doppler sensitivity. To effectively map slow-flow signals and estimate the mean intensity of the flow signal, it is imperative to enhance the system's Doppler sensitivity. This sensitivity is contingent upon the quantity of temporal samples collected during the imaging process. In conventional Doppler techniques, the typical acquisition includes 10-15 samples per pixel in each acquisition, which subsequently impacts Doppler sensitivity when detecting slow-flow signals.

In contrast, the emerging technique of ultrasound signal acquisition known as high-frame rate (ultrafast) plane wave imaging[21] represents a remarkable advancement in the mapping of micro-circulation in micro-vessels through its highly sensitive Doppler technique. In ultrafast imaging, instead of using a focused beam in acquisition event, plane waves are transmitted to insonify the entire imaging area. The returning backscattered echoes received from every point within the imaging area, and the image is constructed through parallel beamforming. This approach possesses an exceptional rapid acquisition time for comprehensive scanning of the imaging area, enabling the acquisition of a larger number of frames in Doppler ultrasound imaging. Furthermore, by employing a single transmission of plane waves and parallel beamforming during reception of signal, the acquisition time extended to allow for the capture of multiple frames. This significantly elevates the frame rate, achieving rates of up to 10 kHz and thereby enhancing temporal resolution. This is why this approach is often referred to as ultrafast ultrasound imaging. However, it’s worth noting that this imaging technique exhibits lower spatial resolution in terms of signal-to-noise ratio (SNR) due to the absence of focus during both transmission and reception of the ultrasonic signal. To address this limitation and improve the imaging performance of plane wave imaging, a solution involves utilizing multiple tilted plane waves during the transmission event. The returning echoes from these waves are coherently summed to produce a high-quality image with improved

resolution[22,23]. Due to its higher temporal resolution and ability to acquire frames at impressively higher rates supports to implement an advanced clutter filters to distinguish the flow signal of micro-vessels and tissue signal efficiently. Demene et all[24] proposed in their study that an advanced spatio-temporal singular value decomposition (SVD) based clutter filtering of ultrafast ultrasound data outperforms than the conventional temporal clutter filters such as FIR (finite impulse response) and IIR (infinite impulse response). They also demonstrated that SVD clutter filter has capability to truncate the clutter (tissue) signal significantly and extract the slow-time blood flow signal from ultrafast compound Doppler data in visualization of micro-vasculatures.

Ultrafast acquisition technique of ultrasound imaging brings a breakthrough in the visualization of microvasculature's in different applications. The concept of ultrafast was reported date back in 1977[21], since then progressive advancements in the technique represents a genuine change in the medical ultrasound paradigm. Montaldo et al[22] demonstrated in their study that the implementation of coherently compounded plane wave imaging in ultrafast ultrasound enhances the imaging performance in terms of SNR which is equivalent to the conventional focused ultrasound imaging but with the advantage of acquisition of signal at higher frame rate. Later, Jeremy Bercof et al[20], shown in their study that using coherently compounded plane wave imaging in imaging framework of Doppler ultrasonography allows to acquire large number of Doppler ensembles which enhances the Doppler sensitivity to detect the slow-moving blood flow signal. Ultrafast Doppler ultrasound provides full blood flow information from large interest of area which leverage the quantification of blood flow under wide range of velocity content. To further extend the utility of this technique, many research studies have been reported in a wide range of applications. as illustrated in Table 1.1. It ranges from small animal imaging[25,26,28,29] to *in-vivo* human micro-vessels imaging of thyroid[20,32], breast[31], kidney[30], liver[30], and skin[27]. These advancements have brought a new era of micro-vessels imaging. This intensive review summarized in Table 1.1 has shown the applicability of ultrafast ultrasound imaging and advanced SVD based clutter filters in visualization of vasculatures in two-dimensional (2D) imaging plane. In 2D imaging this combined techniques retains the capability to image the vasculatures of different size and dimensions at different depth position in various applications ranging from deep perfused

vascular imaging of human kidney[30] to small animal imaging where vasculatures are featured at superficial depths. The insight from this literature review is that imaging of very superficial vasculatures such as in case of rat brain[25] and skin[27], ultra-higher frequency of 40 MHz has been utilized to image the micro-vessels at depth of 0.5 mm. Instead of using ultra-higher frequency of ultrasound, in this study we aimed to devise an imaging framework with center frequency of 30 MHz to image the superficial vasculatures at depth of less than 0.5 mm. To fulfill this gap and to validate the devised imaging framework in visualization of micro-vessels at very superficial depth and advanced signal and image processing algorithms has been proposed.

1.1.3. Three-dimensional ultrasound imaging

The combined approach of ultrafast ultrasound and SVD based clutter filter has shown its impressive advancements in 2D ultrasound imaging in visualization of micro-vasculatures. However, the morphology of these vasculatures in normal and in diseases tissues are characterized as tortuous and branched structures which appear in anastomose manner surrounding the diseased tissue. Imaging of these complex vascular in two-dimensional imaging plane becomes cumbersome using 1D linear array transducer. These transducer capable to image a single cross-sectional region of the imaging area and unable to provide the vascular information outside the insonified imaging region. Imaging of vascular network which are featured to be in wide spread area becomes difficult with 1D array transducer. To observe these complex vasculatures the two-dimensional approach of ultrafast ultrasound imaging would be extended to three-dimensional imaging.

Traditional mechanical scanning approaches has been used in ultrasound three-dimensional volumetric imaging, such as step-by-step mechanical scanning[79,80] and continuous mechanical scanning[73]. Each scanning approach has certain advantages and limitations. In this research study, we implemented both approaches 3D mechanical scanning to perform the 3D volumetric imaging and observe the signal characteristics.

Table 1.1. Literature summary of micro-vessels visualization with ultrafast technique of ultrasound imaging.

Imaging Object	Imaging Depth [cm]	Center Frequency [MHz]	Micro-vessel Imaging	Reference
Rat brain	1.2	14.4		2011, [25]
Human thyroid	2 – 2.2	8	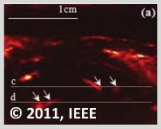	2011, [20]
Pig brain	1	15	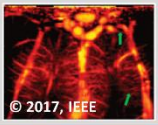	2017, [26]
Rabbit kidney	2	8		2017, [26]
Skin Keloid	0.5	40		2017, [27]
Zebra Fish	0.5	40	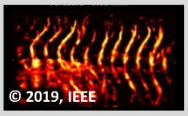	2018, [28]
Rat brain	0.3	40		2019, [29]
Human kidney	5	5	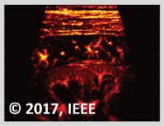	2017, [30]
Human Liver	5	5		2017, [30]
Breast	2	8.5	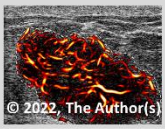	2022, [31]
Thyroid nodules	2	8.5	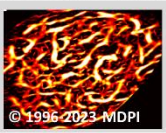	2013, [32]

Also, to visualize the superficial micro-vasculature in three-dimensional view, an efficient 3D volumetric image processing framework has been proposed to overcome the limitations in 3D volumetric imaging and enhance the visibility of vasculatures.

1.1.4. Motivation

Building upon a comprehensive literature review and prior research on microvasculature visualization, this study developed an HFUS imaging framework for visualization of superficial microvasculature in two dimensional and three dimensional imaging. High-frequency ultrafast ultrasound Doppler imaging, centered at 30 MHz, was employed to visualize the vasculature within the skin, consisting of small vessels and microvessels. To distinguish between high-flow and low-flow in vasculatures for visualization of complete cutaneous vascular network, we introduced a novel region-based clutter filtering method based on singular value decomposition. The primary objective of this research is to comprehensively observe the cutaneous vascular network, encompassing both small and microvessels., in two dimensional and three dimensional view to facilitate an effective and efficient diagnosis of cutaneous disorders.

In the pursuit of this goal, we conducted an *in-vitro* phantom study to optimize the HFUS imaging framework for enhanced visualization of superficial microvessels. Subsequently, we performed *in-vivo* imaging at three different positions of the dorsal hand to visualize the superficial cutaneous vascular network. To evaluate the sensitivity and resolvability of the devised HFUS imaging framework in two dimensional and three dimensional high-frequency ultrafast Doppler imaging, we designed and created phantoms with straight micro-channel and complex bifurcated channel at superficial depth of 4 mm, featuring core (micro-channel) dimensions of 200, 300 and 220 μm in diameter respectively. To visualize the superficial vasculatures in multi-dimensional view, HFUS two-dimensional imaging framework extended to three-dimensional volumetric imaging. For that we performed 3D volumetric imaging *in-vitro* and *in-vivo* via step-by-step scanning approach as well as with continuous mechanical scanning approach to validate HFUS imaging framework in visualization of superficial micro-vessels in *in-vivo* 3D volumetric imaging.

1.2. Research Objectives

This research aims to devise an imaging framework, which enables the visualization of superficial skin in two-dimensional and three-dimensional ultrasound Doppler imaging. The idea is to evaluate the imaging performance of the devised framework under configurations of high-frequency ultrasound with ultrafast Doppler imaging and efficiency of clutter filtering and denoising algorithms in *in-vitro* and *in-vivo* experiments. To achieve our objective the following approaches have been considered in a sequential manner:

1. Optimize an imaging sequence of high-frequency ultrasound (HFUS) ultrafast Doppler imaging in detection of micro-flow signal.
2. Design and fabricate a novel superficial micro-flow flow phantom with wall-less micro-channel in Y-shape geometry to mimic superficial intricate microvasculature.
3. Visualize the superficial microvasculature at the depth of less than 5 mm with a devised imaging framework.
4. Design a novel SVD based clutter filter to extract the flow signal from small vessels and micro-vessels of cutaneous vascular network efficiently.
5. Visualize complete cutaneous vascular network (*in-vivo*) with combined approach of proposed region-based SVD clutter filter and top-hat morphological filtering of high-frequency ultrafast ultrasound.
6. Volumetric imaging of superficial micro-structure via step-by-step and continuous mechanical scanning approach (Phantom).
7. Denoising of 3D volumetric data obtained from continuous mechanical scanning by implementing non-local means (NLM) filter.
8. Three dimensional *in-vivo* visualization of complete cutaneous vascular network with proposed imaging framework.

1.3. Outline

This thesis dissertation is divided into seven chapters, which comprise on the

optimization of two-dimensional and three-dimensional imaging framework in *in vitro* phantom imaging and *in-vivo* superficial micro-vasculature imaging. This chapter presents the general background as an introduction to the thesis. It summarizes the background, motivation, and significance of this dissertation. The subsequent chapters can be summarized as follows:

Chapter 2: Development of an imaging framework to visualize superficial micro-vessels.

This chapter presents an overview of the high-frequency ultrasound imaging framework. In-detail discussion about the optimization of high-frequency ultrasound imaging sequence in visualization of superficial micro-structures. In this chapter, I have completed the research objective 1.

Chapter 3: Fabrication of micro-flow phantom to simulate superficial complex micro-vessels.

Moving towards the research objective 2, this chapter presents a novel phantom fabrication protocol for superficial micro-flow phantoms to simulate the superficial intricate microvasculature and performed high-frequency ultrafast ultrasound imaging to visualize the fabricated Y-shaped micro-channel at depth of less than 5 mm.

Chapter 4: Two-dimensional imaging of superficial micro-vessels.

This chapter presents the research objective 3, the imaging of superficial micro-vessels at depth of less than 5 mm *in-vivo* at the tip of index finger using a devised imaging framework of high-frequency ultrasound ultrafast Doppler at the center frequency of 30 MHz.

Chapter 5: Region-based SVD processing of ultrafast ultrasound.

This chapter presents a novel clutter filtering approach based on singular value decomposition (SVD) for an efficient extraction of flow signal to visualize a complete cutaneous vascular network with high-frequency ultrafast ultrasound Doppler imaging. In this chapter, I have accomplished the research objectives 4 and 5.

Chapter 6: Three dimensional volumetric imaging of superficial micro-vessels.

This chapter elaborates about the significance of continuous mechanical translation approach in 3D volumetric imaging, implementation of non-local means (NLM) as a denoising filter, and processing of volumetric data in section wise approach to visualize the micro-flow tract efficiently. Here, I have accomplished the research objectives 6,7 and 8.

Chapter 7: Conclusion and future perspectives.

This chapter provides the concluding remarks and offers a summary of the research study. Discussion about the research findings, conclusions, and the potential future directions for this research.

Chapter 2

Development of an Imaging Framework to Visualize Superficial Micro-vessels

This chapter presents the development of an imaging framework comprised on high-frequency ultrafast ultrasound (HFUS) Doppler imaging and spatio-temporal singular value decomposition (SVD) based clutter filtering. Various *in-vitro* phantom experiments were conducted to optimize the parameters of HFUS imaging sequence and to extract the slow-time signal of micro-flow signal from micro-flow channel of phantom efficiently. Straight channel micro-flow phantom was developed [63] featuring the wall-less micro-structure at the depth of 4 mm. It is fabricated as straight micro-flow channel in tissue mimicking material (TMM) of polyvinyl alcohol (PVA), the TMM was prepared by following the protocol [59]. The developed micro-flow phantom was utilized in the experimental setup which mimics the superficial micro-vessels to optimize the HFUS imaging sequence. HFUS ultrafast ultrasound Doppler imaging was performed *in-vitro* (micro-phantom) and later *in-vivo* (index finger) to observe the efficacy and resolvability of the devised imaging framework.

2.1. Basic Principle

Ultrasound imaging is widely used as a non-invasive imaging modality in medical diagnostics. This technique utilizes the high-frequency sound waves to create a detailed images of the internal structures of the human body. The frequency of sound waves in ultrasound imaging varies from 1 MHz to 25 MHz depending on the specific medical application and the type of human tissue/targeted object being examined. Additionally, it plays a quite important role in observing the flow of blood within the arteries and veins of the circulatory system. By utilizing the Doppler effect in ultrasound imaging, it becomes possible to measure the hemodynamics in blood vessels, enabling the

visualization and observation of blood vessels morphology (small vessels and micro-vessels).

2.1.1. High frequency ultrasound

High-frequency ultrasound (HFUS) refers to ultrasound waves with a center frequency exceeding the 20 MHz. The sound waves at higher frequencies are identified by their shorter wavelengths, making them susceptible to absorption by objects in the surrounding medium during imaging and resulting in restricted penetration depth. Therefore, high-frequency ultrasound (center frequency > 20 MHz) is particularly well-suited for superficial imaging[33]. Also, the features of shorter wavelength and narrower beam of ultrasound waves associated with higher frequencies results in enhanced image resolution (the ability of the system to image the possible minute (small) structures).

As depicted in Fig. 2.1, as the number of ultrasound waves increases the distance between the compression and rarefaction phases of waves also increases, which enhances the absorption and differentiation of the targeted object as the waves propagate axially in the imaging field. Subsequently, it results with enhanced image quality and resolution with limited depth penetration.

Imaging resolution is considered as one of the important factor in determining the image quality, encompassing both axial and lateral resolution. Axial resolution refers to the system's ability to differentiate between two scatterers in the medium that are aligned parallel to the direction of the ultrasound beam. Conversely, lateral resolution pertains to the system's capability to distinguish between two scatterers situated perpendicular to the direction of the ultrasound beam[34]. High-frequency ultrasound excels in axial resolution, making it adept at distinguishing between two targeted objects within the imaging field.

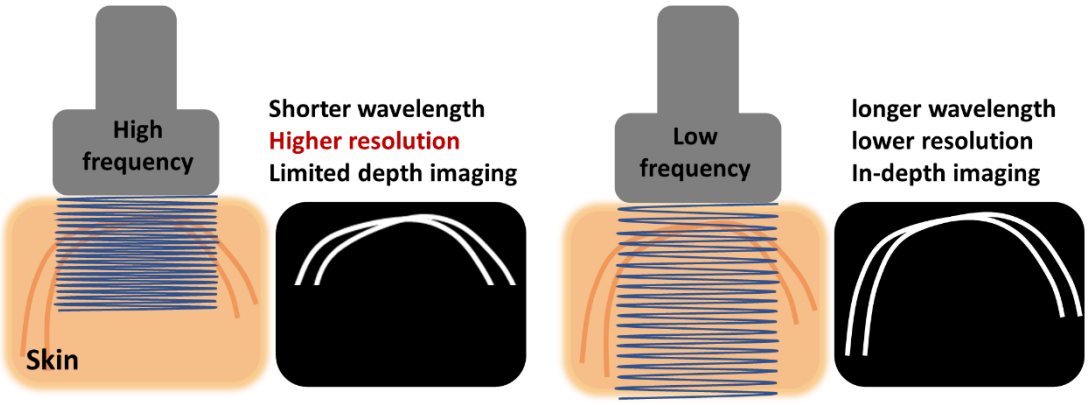

Fig. 2.1. Representation of high-frequency and low-frequency of ultrasound imaging.

2.1.2. Ultrafast Ultrasound

Ultrafast Ultrasound, also known as plane wave imaging[21], represents an emerging ultrasound acquisition technique in which plane waves are used to scan the imaging plane. This emerging approach of ultrasound allows the creation of an entire image of the imaging area with just a single transmission of an acoustic pulse as shown in Fig. 2.2(b). In this technique, a single plane wave of an acoustic pulse is emitted from all the elements of a linear array transducer. The transmitted, non-focused pulse interact with the scatterers in the imaging medium, generating a backscattered signal that is received by the transducer's elements as an echo signal. Due to the lack of focus in plane wave transmission results an image with poor resolution. Consequently, images obtained through this broad insonification of the imaging area have been characterized by poor resolution, contrast, and signal-to-noise ratio. However, this acquisition technique retains the unique features such as synchronized acquisition of the ultrasonic backscattered signal at ultra-high framerate. On the contrary, conventional ultrasound acquisition technique shown in Fig. 2.2(a) involves the sequential transmission of the focused pulses along the imaging area in a line-by-line scheme. While this focused wave transmission scheme yields higher spatial resolution, it results in acquisition of signal asynchronously at lower frame rate with poor temporal resolution.

The influential features of ultrafast ultrasound in Dopler imaging are its ultra-high

framerate and synchronous acquisition of backscatter signal, which enables to locate the fastest motion of blood flow signal as well as assist in mapping the slow-moving blood flow signal in micro-vessels. To address the limitation of poor image quality in terms of resolution associated with the lack of focus in plane wave transmission, the concept of ultrafast compounding (Fig. 2.2(c)) was proposed [cite a paper] to enhance the credibility of ultrafast imaging. In that approach, multiple plane waves are transmitted at various steering angles and coherently summed at the reception of the backscattered signal. The obtained images from different steering angles allowed to reconstruct a compounded image with improved image quality and resolution.

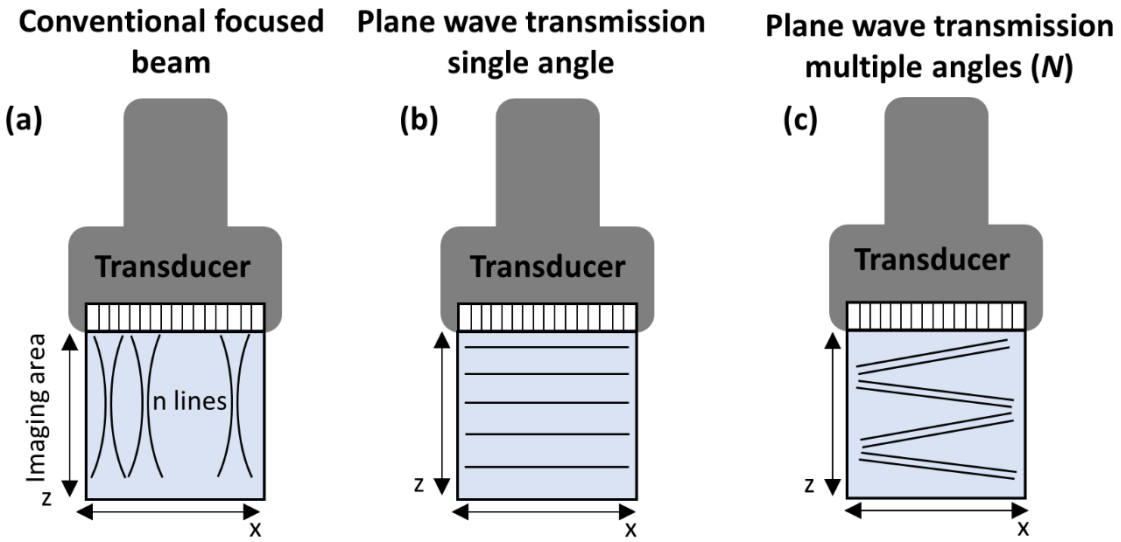

Fig. 2.2. Comparison between (a). Conventional ultrasound imaging. (b). Emerging technique of plane wave ultrafast ultrasound imaging. (c). Ultrafast compounded plane wave imaging.

2.1.3. Doppler Ultrasound

Doppler ultrasound is a widely utilized technique for assessing blood flow signals, providing valuable insights into the hemodynamics and morphology of blood vessels. To measure the blood flow signals, ultrasonic pulses are emitted through the blood vessels, and echo signals are received through backscattering from the red blood cells. The flow signal from red blood cells is analyzed by examining the temporal variations in the

successive backscattered signals during each pulsed emission.

Traditional Doppler imaging employs a repetitive, focused pulse beam aimed at a single position within the medium to capture echo signals from each transmission event. This process is then replicated at various positions across the imaging area to comprehensively understand the blood flow variations within each location or block. Subsequently, the entire imaging area is sequentially scanned using the focused beam to generate a complete image[20]. While this technique effectively quantifies blood flow in larger vessels, its limitations become evident when detecting slow-flow signals within micro-vessels. To address this challenge and estimate the mean flow signal intensity, enhancing the system's sensitivity is crucial. Sensitivity to slow flow signal depends on the number of temporal samples (Doppler ensembles) collected during the imaging process. Conventional focused ultrasound typically acquire 10-15 samples per acquisition, subsequently impacting the Doppler sensitivity for slow-flow signals.

In contrast, ultrafast imaging revolutionizes in Doppler imaging by utilizing a single transmission event to instantaneously scan the entire imaging field and receive the backscattered echo signals at an ultra-high frame rate. This innovation significantly enhances the system's Doppler sensitivity, enabling the detection of even the slowest flow signals emanating from micro-scale structures (micro-vessels). Furthermore, it facilitates the implementation of an efficient clutter filtering approaches, enabling to differentiate between the tissue signal and the blood flow signal. Leveraging these attributes of ultrafast acquisition approach in Doppler imaging, it becomes possible to visualize and map the micro-circulation in microvasculature by optimizing the system's sensitivity for detecting the slow-flow signals.

2.1.4. Tissue motion (Clutter) in Ultrasound Flow Imaging

In ultrasound flow imaging, the term “clutter” refers to undesired echo signals generated by stationary and slowly moving tissue structures within the imaging plane. The presence of these tissue-generated signals poses a challenge in detection of blood flow signal within micro-vessels. This challenge arise from the fact that tissue signals generally have a significantly higher backscattering strength than the blood signal, mainly

due to its higher acoustic impedance mismatch[35]. Additionally, tissue motion tends to be slower than blood flow, leading to the dominance of low-frequency components in the Doppler spectrum[36]. In contrast, the rapid variation in blood flow generates signals with a wide range of frequencies. As shown in Fig. 2.3 in the presence of tissue motion, clutter echoes become broadband and overlap the slower blood flow signal. This problem of tissue and blood echoes sharing similar spectral characteristics is particularly significant in ultrasound micro-vessels imaging. Additionally, when aiming to detect slow flow within tumor micro-vasculature, a critical aspect of cancer diagnosis[37], the frequencies of blood signal in these cases closely align with those of tissue clutter. This overlapping of frequencies hinders the clear visualization of vascular structures.

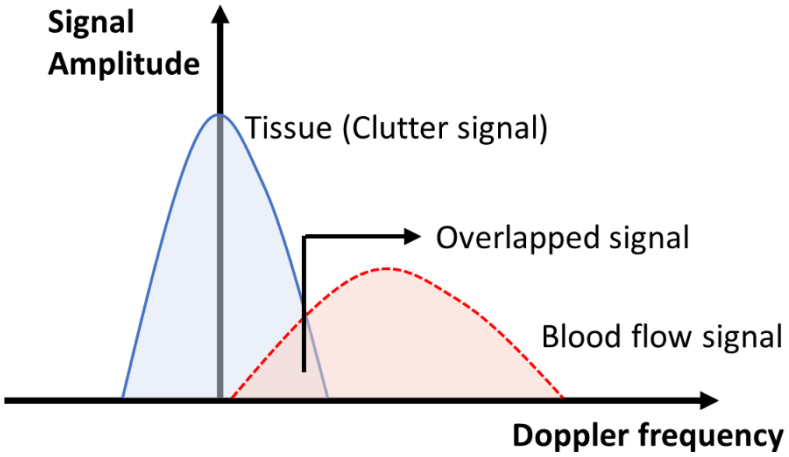

Fig. 2.3. Doppler spectral characteristics

2.1.5. Conventional Methods of Clutter Filtering

Conventionally, the filtering of blood flow signal from clutter (tissue) signal was performed by temporal filters. These filters includes high pass filtering methods such as finite impulse response (FIR) filter[38], infinite impulse response (IIR)[39] filter, and polynomial filters[40]. These techniques focused solely on the temporal aspect of the Doppler signal and performed filtering under the assumption that the tissue signal and blood flow signal had distinctly different spectral characteristics. Based on these

assumptions temporal filters failed to differentiate between the tissue signal and blood signal when their Doppler frequency spectrums significantly overlapped as shown in Fig. 2.3. Consequently, temporal filtering methods often led to the removal of tissue clutter at the cost of filtering out the slow velocity blood flow signal as well. Adaptive filters, such as based on clutter downmixing matrix, were also employed to suppress the tissue signals. However, they faced the limitations related to the accuracy of the downmixing matrix and the relatively small number of Doppler samples available, especially in focused transmission schemes. These limitations can be overcome by utilizing unfocused ultrafast ultrasound imaging, which enable to acquire the synchronous acquisition of data from the entire imaging field at a very high frame rate. This imaging technique plays a decisive role in the design and implementation of clutter filters that function across both spatial and temporal dimensions. Such filters are designed to extract the flow signal at a wide range of velocities while effectively mitigating the influence of clutter signals.

2.1.6. Eigen-based Clutter Filtering

The emergence of eigen based clutter filtering has addressed the limitations of traditional temporal clutter filtering methods by leveraging both the spatial and temporal characteristics of signal to differentiate the tissue clutter and blood subspace more effectively[41-43]. Eigen based filtering has intensely benefited from the long Doppler ensembles obtained by ultrafast plane wave imaging.

The process involves the implementation of singular value decomposition (SVD) to the raw ultrasonic data, resulting in generation of singular values. The gradual decrease in the amplitude of these singular values facilitates the removal of high-energy clutter component. Singular vectors produced by SVD contain spatiotemporal information that is influential in identifying and removing the tissue clutter from the blood flow signal. Demene et al have proposed a method involving the implementation of SVD on ultrafast data to eliminate clutter signal, demonstrating a notable improvement in the ability to detect overlapped slow-time blood flow signals within the Doppler spectrum while effectively eliminating the tissue signal.

2.2. Methodology

An experimental setup (Fig. 2.4) was devised to optimize the sensitivity of imaging sequence in detection of slow-time slow flow signal of superficial micro-vessels. It is comprised on Vantage Verasonics 256 channel research purpose ultrasound system equipped with L38-22v CMUT (KOLO SiliconWave, USA) linear array high-frequency transducer. A micro-flow phantom (Fig. 2.4(b)) with flow channel of 200 µm in diameter up to the depth of 4 mm was developed and utilized to mimic the superficial micro-vessels. A flow circuit assembly (Fig. 2.4(c)) was connected with micro-flow phantom to infuse the flow under different flow rate settings to observe and evaluate the Doppler sensitivity of devised imaging framework.

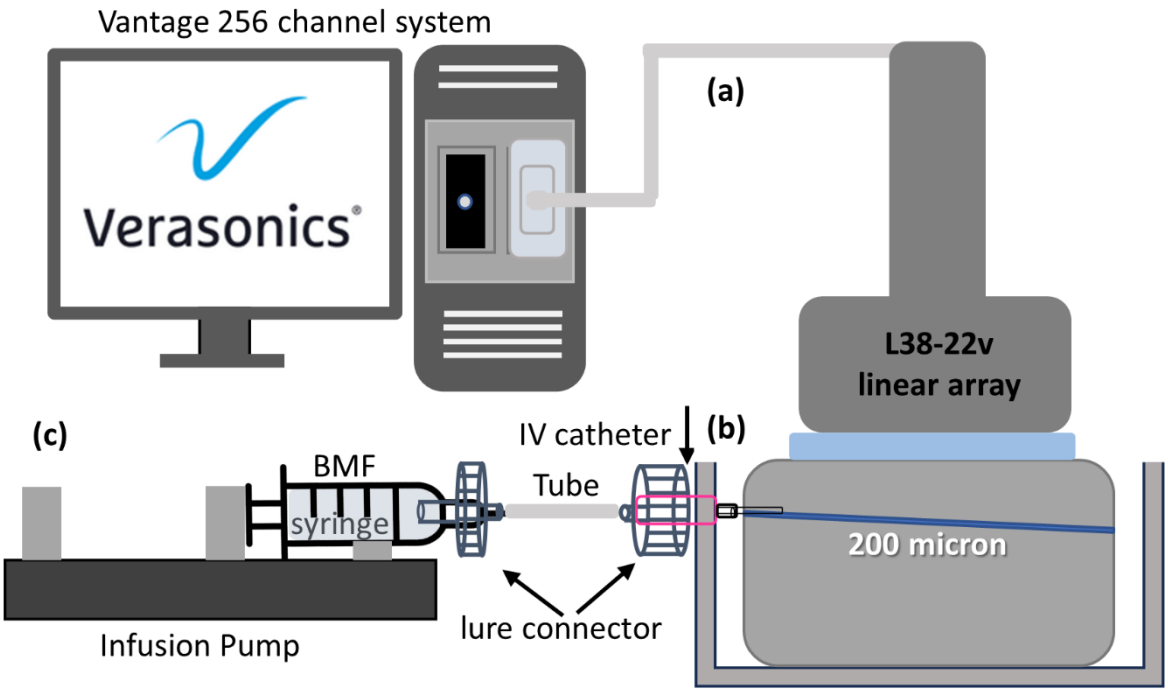

Fig. 2.4. Experimental setup. (a). High-frequency ultrasound research purpose platform. (b). Micro-flow phantom. (c). Flow circuit assembly.

2.2.1. Imaging platform

A research purpose ultrasound imaging system vantage Verasonics 256 channel with

high-frequency configuration (Verasonics Inc., Kirkland, WA, USA) was used to transmit and receive the ultrasonic signal. L38-22v CMUT (KOLO silicon, USA) high-frequency linear array transducer was equipped with the system. The transducer was manufactured with capacitive micro-machined ultrasound transducer (CMUT) technique and had an aperture size of 17.6 mm consisted of 256 elements.

The vantage 256 channel system is comprised on data acquisition hardware unit connected to the host controller computer. The host PC contains software modules implemented within MATLAB programming environment. The acquisition hardware contains electronic modules for generation of transmit waveform, analog receive signal, signal amplification, filtering, digital processing, and scan sequencing [26]. MATLAB programming environment allows to execute the sequences as per respective application. It has 14 bits analog to digital converter with programmable sample rate of up to 62.5 MHz. Vantage system has specified high frequency configuration settings which enable the system to use high frequency transducers with center frequencies of up to 50 MHz. Noted, due to the limited sampling rate of vantage system of approximately 62.5 MHz which is insufficient for acquiring 30 MHz echo signal under Nyquist sampling rate. We introduced the bandwidth sampling approach[44] under vantage high-frequency configurations to acquire the signal with a controlled sampling rate of 41.6 MHz.

2.2.2. Ultrasound Signal Acquisition and Processing (Imaging sequence)

The linear array transducer consisting of 128 elements were excited at a center frequency of 31.5 MHz to acquire the IQ demodulated signal from micro-flow channel. To acquire the signal, 3 pulse cycles at seven plane waves were transmitted at different steering angles (-10 degree to 10 degree). All the obtained IQ images were coherently compounded to enhance the overall image quality. The pulse repetition frequency (PRF) between plane wave emissions was 7 kHz. 75 Doppler ensembles were acquired for plane wave transmission to assess the subtle flow signal competently. Acquisition parameters are described in Table 2.1 used to acquire Doppler signal under four different flow velocity settings.

To extract the desired micro-flow signal of blood mimicking fluid in micro-flow

phantom. SVD clutter filtering was performed to extract the flow signal from HFUS ultrafast Doppler data. To perform the SVD [24] filtering, the obtained three dimensional ultrafast ultrasound data matrix ((n_x, n_z, n_t) was rearranged in to two-dimensional ($n_x \times n_z$, n_t) Casorati matrix ***S,*** later the SVD was implemented on the rearranged matrix which results in decomposition of three different matrices as shown in equation 1.

$$\boldsymbol{S} = \boldsymbol{U}\Delta\boldsymbol{V}^{*} \qquad (1)$$

where, ***U*** and ***V*** are orthogonal matrices with respective spatial and temporal dimensions and Δ is a diagonal matrix which corresponds to singular values λ_i. To extract the slow signal of micro-flow, clutter rejection was performed arbitrary based on the assumption that the flow signal and noises reside in the lower singular values and tissue signal lies in the higher singular values. For filtering an optimal threshold value (from the diagonal singular values) was obtained arbitrary to extract the desired signal as in equation 2.

$$s_{blood}(x,z,t) = s(x,z,t) - \sum_{i=1}^{n} \lambda_i \, . \boldsymbol{U}_i(x,z)\, \boldsymbol{V}_i(t) \qquad (2)$$

where $s_{blood}(x,z,t)$ is a matrix of filtered signal, in which first diagonal singular values were rejected (zeros) resulted in a matrix with filtered data of desired flow signal (ones). Finally, each pixel intensity of a power Doppler image $PW(x,z)$ was generated by computing energy per pixel as in equation 3.

$$PW(x,z) = \int | s_{blood}(x,z,t)|^2 \, dt \qquad (3)$$

Table 2.1. Acquisition parameters of HFUS ultrafast ultrasound imaging.

Parameter	Value
Probe	L38-22v CMUT Probe
Number of elements	128
Pitch	0.0690 mm
Central frequency	31.5 MHz
Sampling frequency	41.6 MHz
Excitation pulse	3 cycles
Speed of sound	1540 mm/s
Pulse repetition frequency (PRFmax)	7000 Hz
Doppler angle	10°
Doppler Ensemble	75
Compounding transmissions	7

2.2.3. Experimental setup

To evaluate the performance of high-frequency ultrafast ultrasound imaging sequence, various experiments were performed on 200 µm flow phantom to optimize the imaging sequence for superficial micro-vessels visualization.

An experimental setup shown in Fig. 2.5 was utilized to perform *in-vitro* experiments was comprised on a micro-flow phantom, with slightly tilted 200 µm straight micro-channel at the superficial depth of 4 mm. A flow circuit assembly which includes an infusion pump, IV catheter (ethylene tetrafluoroethylene (ETFE). 26 G), plastic tubing and luer connectors (1.5 mm inner diameter) was connected with micro-flow phantom to infuse the flow in the micro-channel. A micro-flow of blood mimicking fluid (ATS Laboratories, Doppler Test Fluid Model 707) was infused at four different flow rate settings (56, 37, 28, and 18 µl/min) with respective velocities (approximately 30, 20, 15 and 10 mm/s) as presented in Table 2.2 to evaluate and observe the system's sensitivity in detection of micro-flow signal from slightly tilted straight 200 µm flow channel.

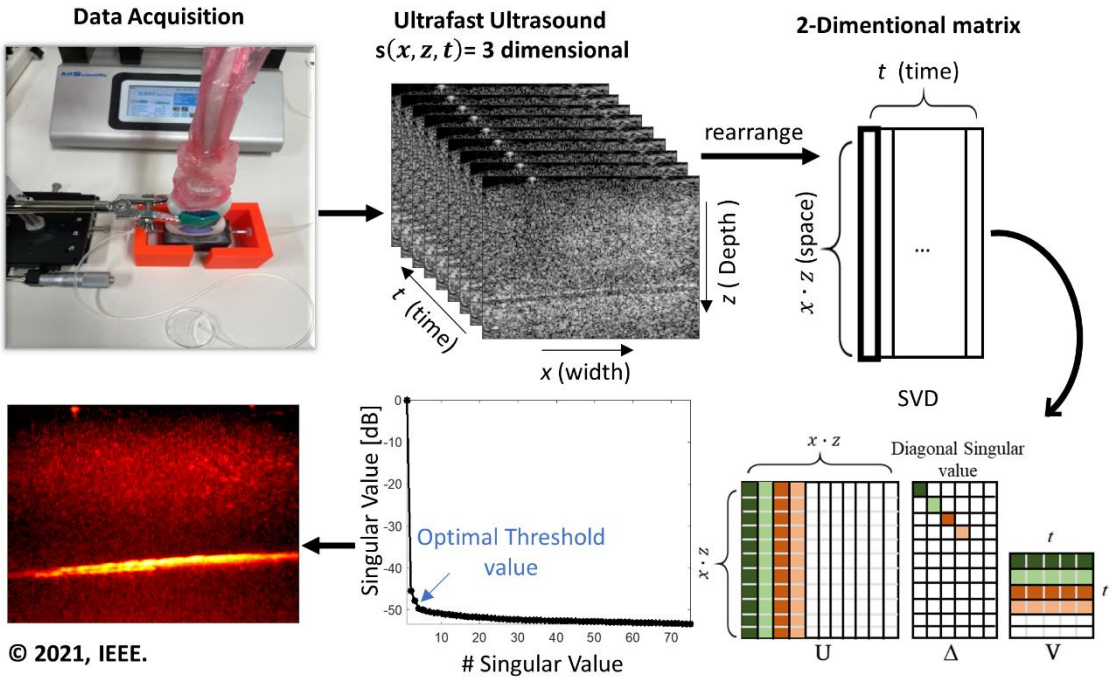

Fig. 2.5. Acquisition and processing of ultrafast ultrasound data.

Table 2.2. Infusion pump flow rate settings under four different flow velocities

Infusion Pump Settings				
	Setting 1	Setting 2	Setting 3	Setting 4
Syringe	20 ml			
Flow Rate	4.7 ml/min	3.7 ml/min	2.8 ml/min	1.88 ml/min
Average Flow Velocity	25 mm/s	20 mm/s	15 mm/s	10 mm/s

2.3. Results

Experiments from micro-flow phantom, utilizing the HFUS ultrafast Doppler imaging revealed the visualization of micro-flow channel at the depth of 4 mm under different flow rate settings. The processed power Doppler images with devised imaging framework has depicted the visualization of the micro-structure as shown in Fig. 2.6. The ultrafast compounded data acquired from the micro-flow phantom was processed with the SVD clutter filter. The desired flow signal was extracted from the diagonal matrix of singular values at an optimal threshold as indicated by blue arrow in Fig. 2.5. Later the power Doppler images were generated to visualize the flow channel under respective flow rate settings. The high-intensity signal of blood mimicking fluid (BMF) was meticulously mapped, and clearly discerned the micro-flow tract up to the depth of 4 mm as presented in Fig. 2.6.

In addition to qualitative analysis, quantitatively we assessed the capability of the devised framework in detection of slow-flow signal. The diameter of the visualized flow tract was measured by averaging the intensity profile obtained from micro-flow channel under different flow rate (56 µl/min – 18 µl/min) settings. It was observed that the intensity of signal gradually decreases as the flow rate decreases as shown in Fig. 2.6. The intensity of micro-flow channel was brighter and dense with flow rate of 56 µl/min and decreased with flow rate of 18 µl/min. These findings suggests that the devised imaging framework has sufficient Doppler sensitivity to detect the flow signal under wide range of slow-flow velocities.

Quantitatively, the diameter of the visualized micro-channel was also evaluated. As shown in Fig. 2.7, the axial intensity profiles of detected micro-channel was measured along the lateral direction of slightly tilted flow tract. Full width half maximum (FWHM) at -6dB was calculated from each respective lateral position from the obtained power Doppler images. Intensity profiles from six different position as indicated by different colour lines in Fig 2.7 were included to estimate the system resolvability by measuring averaged diameter of flow tract under different flow-rate settings. All the measured diameters were analysed to calculate the mean average value and the standard deviation. From these quantitative measurements, it was observed that the averaged diameter of the

flow tract with flow speed of 30 mm/s was 170-micron which decreases gradually as the flow rate decreases. Overall, the mean average detected diameter was calculated in the range of (170-micron - 93-micron) as shown in Fig. 2.8. To observed that the detected diameter of the micro-flow tract was from the stream of BMF in the micro-channel or the deformation of the micro-flow channel. To evaluate that phenomenon the axial diameter of the micro-flow tract was measured manually from the obtained B-mode images as shown in Fig. 2.9. The measurement of the micro-channel diameter was calculated from the similar lateral positions which were chosen for the measurement of intensity profiles of flow stream from respective power Doppler images shown in Fig. 2.7. From that analysis, it was observed that the dimension of the micro-channel remains persistent in B-mode images analysis under two different flow rate settings of 30 mm/s and 10 mm/s. The averaged diameter from that measurement were observed to be 209.1 μm with flow speed of 30 mm/s and 200.6 μm with flow speed of 10 mm/s as shown in Fig. 2.9. These findings suggest that the decreasing trend in the diameter of the flow tracts corresponds to the BMF flow in the micro-channel under respective experimental conditions. It also indicates that the devised imaging framework has the potential to visualize the micro-structures with slow-flow circulation from higher to slower flow rate in micro-vessels. At the flowrate of 18 μl/min, imaging framework was deficient at some instance in detecting the signal from the striking particles of BMF flowing in the micro-channel. Also, it is necessary to noted that the flow stream was quite slow in motion to maintain the consistency along the flow-tract of 200 μm. These observations also indicates that the visualization of micro-structures with flow circulation (> 18 μl/min) might be challenging in B-mode imaging. However, in power Dopler images, the high intensity signal of flow leads the significant identification of the micro-structure.

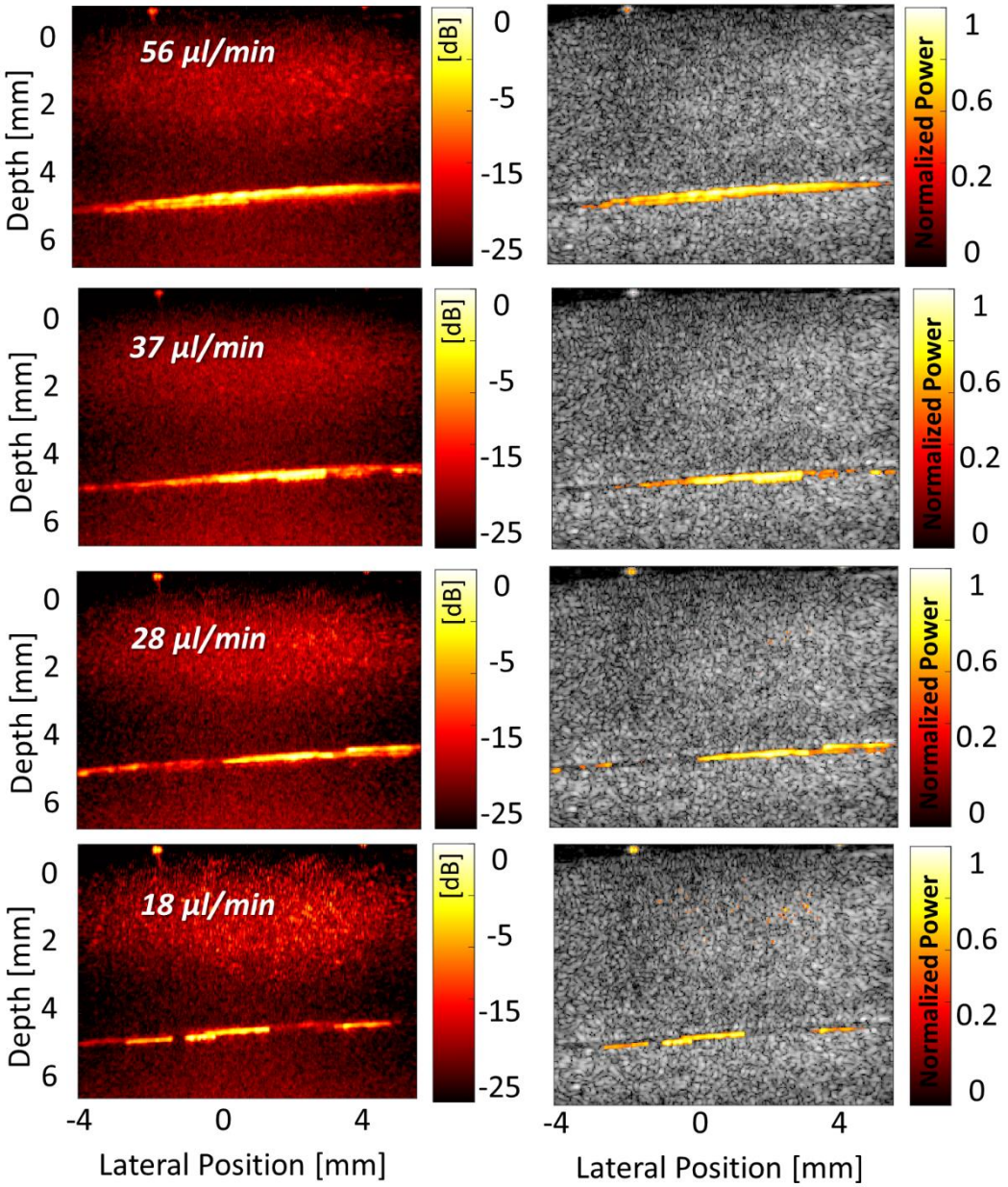

Fig. 2.6. Obtained power Doppler images with respective B-mode superimposed images of micro-flow phantom under different flow rate settings. © 2021, IEEE.

The relation between the sensitivity of the Doppler ultrasound signal in the detection of micro-flow signal and the Doppler ensemble was also investigated. The acquired

HFUS dataset was processed with SVD clutter filter under different number of Doppler ensembles of different sizes such as 75 ensembles, 50 ensembles and 25 ensembles. The obtained power Doppler images from that analysis shown in Fig 2.10. suggests that higher the number of Doppler frames (ensembles) higher the detection of the flow signal. The mapped intensity of flow signal processed with 75 Doppler ensembles was higher than that of 50 ensembles and 25 ensembles as shown in Fig. 2.10.

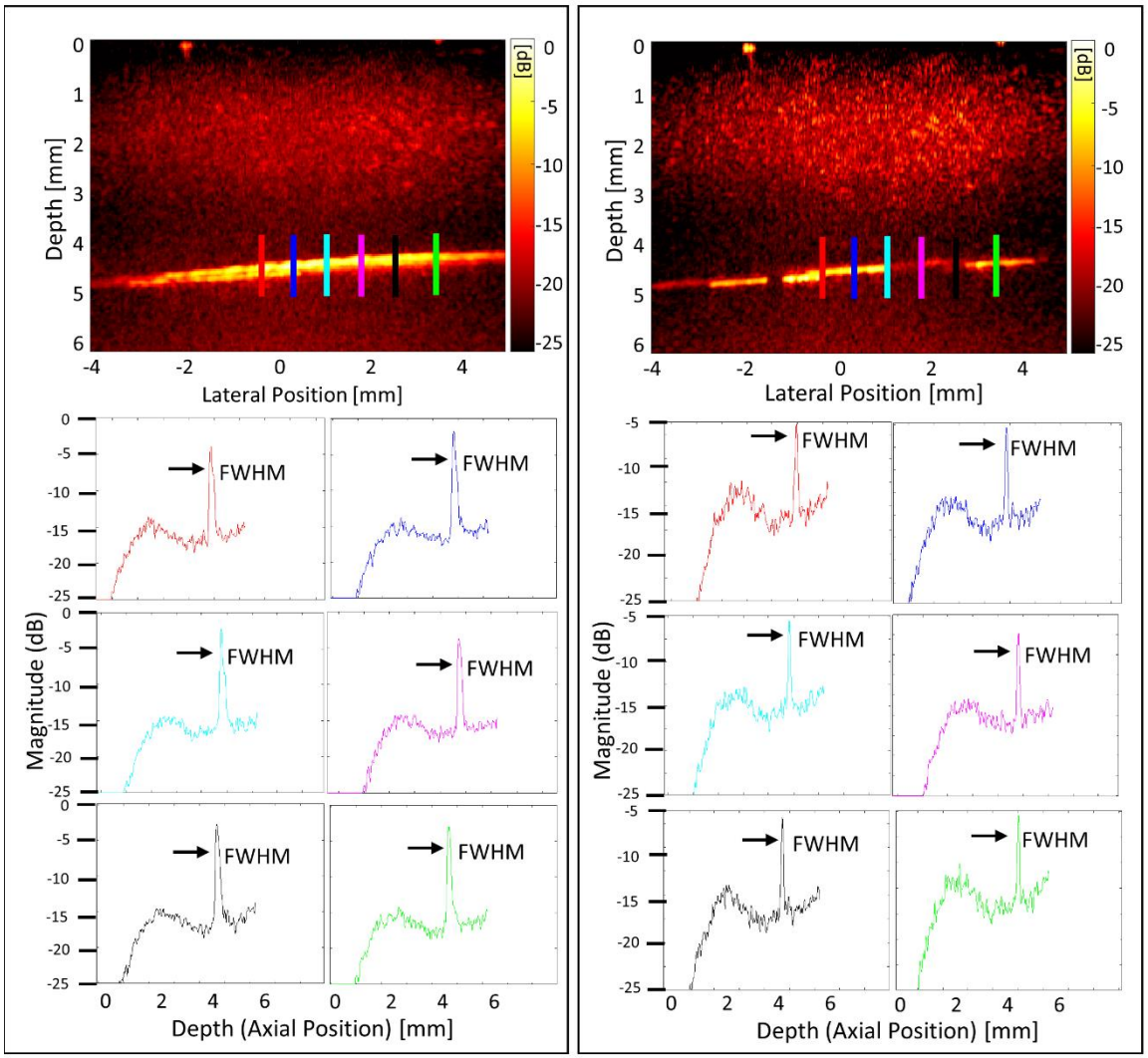

Fig. 2.7. Detected diameter of micro-flow tract under higher 56 µl/min (a) and slower 18 µl/min (b) flow rates. Measured FWHM at six different lateral profiles represented by red, blue, cyan, magenta, black and green color. © 2021, IEEE.

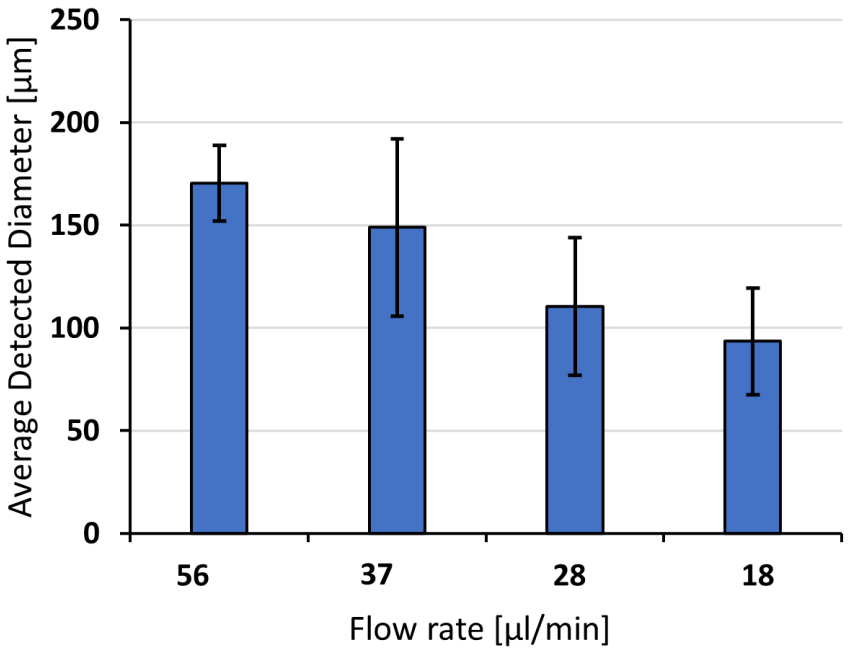

Fig. 2.8. Averaged detected diameter of flow tract under four different flow rate setting. © 2021, IEEE.

2.4. Discussion

Visualization of the micro-structure, using devised imaging framework, with maximum and minimum detected diameter of (170-micron - 93-micron) has been proposed as a potential framework of gaining new insight in superficial micro vessels imaging. In this research study we presented that HFUS ultrafast imaging with centre frequency of 31.5 MHz can visualize the micro-structures, instead of using ultra-higher frequencies[27] of 40 MHz. The resolution of the devised framework which was reported in our previous study [81] was in range of 80 to 160 µm to visualize the superficial micro-structures. Also, the highly sensitive Doppler technique of ultrafast imaging with singular value decomposition (SVD) based spatio-temporal clutter filter revealed that, at centre frequency of 31.5 MHz and with sufficient Doppler ensembles acquired with ultrafast acquisition enhances the sensitivity to visualize the micro-structures with micro-

circulation (slow-flow). In addition, qualitatively and quantitively we demonstrated that the micro-structures can be visualized by mapping the flow signal with combined approach of ultrafast Doppler and SVD clutter filter. The Doppler sensitivity to map the slow-flow signal depends mainly on two factors. One of that is the number of acquired Doppler ensembles or B-mode frames as presented in Fig. 2.10 and the other factor is number of compounding angles which enhances the image quality and resolution in plane wave ultrafast imaging effect. As illustrated in Fig. 2.10 higher the number of Doppler ensembles (frames) higher the detection of slow-flow signal. The mapped intensity of BMF particles in the micro-flow tract was higher when higher number of Doppler ensembles were processed with SVD clutter filter. That phenomenon was observed under higher flow rate of speed 30 mm/s (Fig. 2.10 (a)) and lower flow rate of speed of 10 mm/s

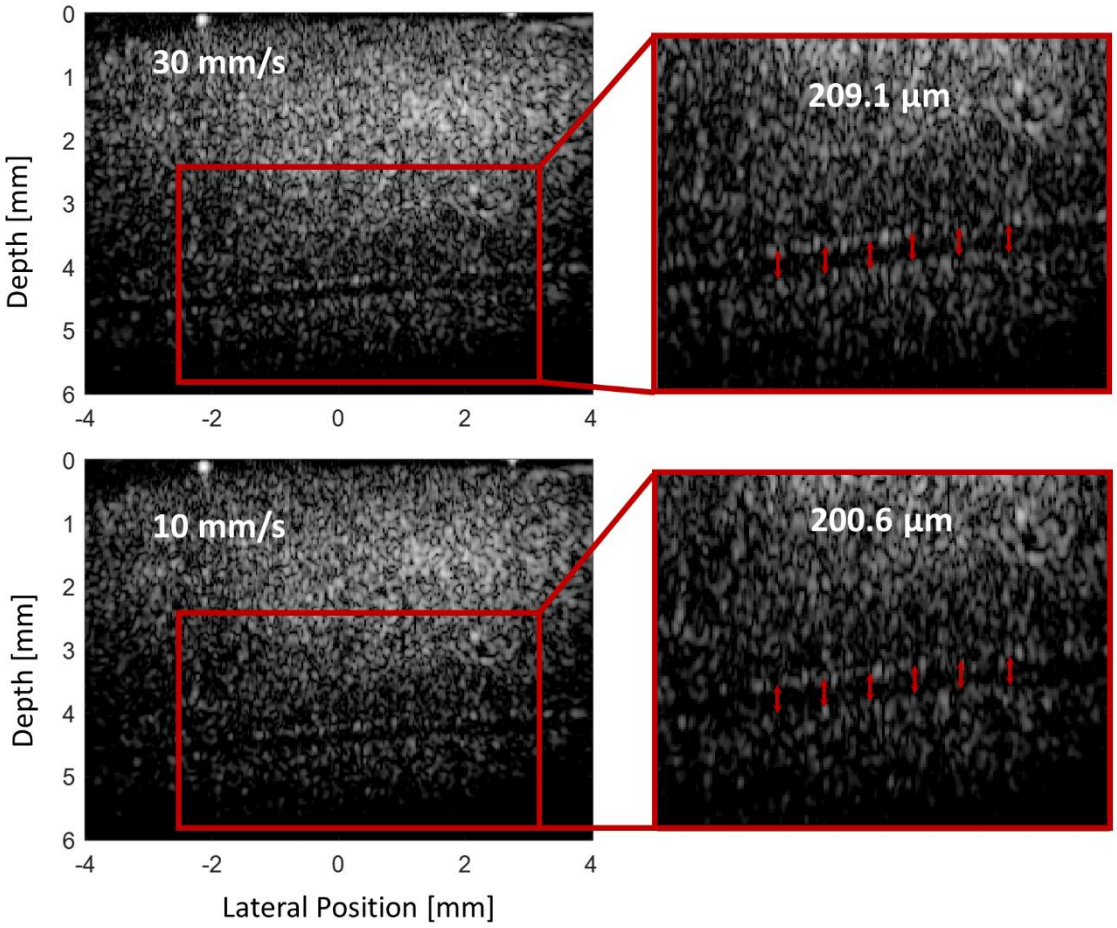

Fig. 2.9. Measurement of averaged detected diameter of micro-flow tract from obtained B-mode images under flow speed of 30 mm/s and 10 mm/s.

Besides, the acquisition parameters such as centre frequency and higher number of Doppler ensembles and implementation of SVD clutter filter, an efficient and robust noise filtering is also required to overcome the background system generated noises. Song et al[26] reported in their study that if the amplitude of slow-flow signal overlapped by the amplitude of clutter or noise signal, it is difficult to extract the flow signal efficiently. Therefore, for robust extraction of slow-time signal in *in-vivo* imaging using SVD clutter filtering, it is essential to eliminate the noise filed, which causes hinderance in extraction of slow-time flow signal and ultimately in visualization of micro-vasculature.

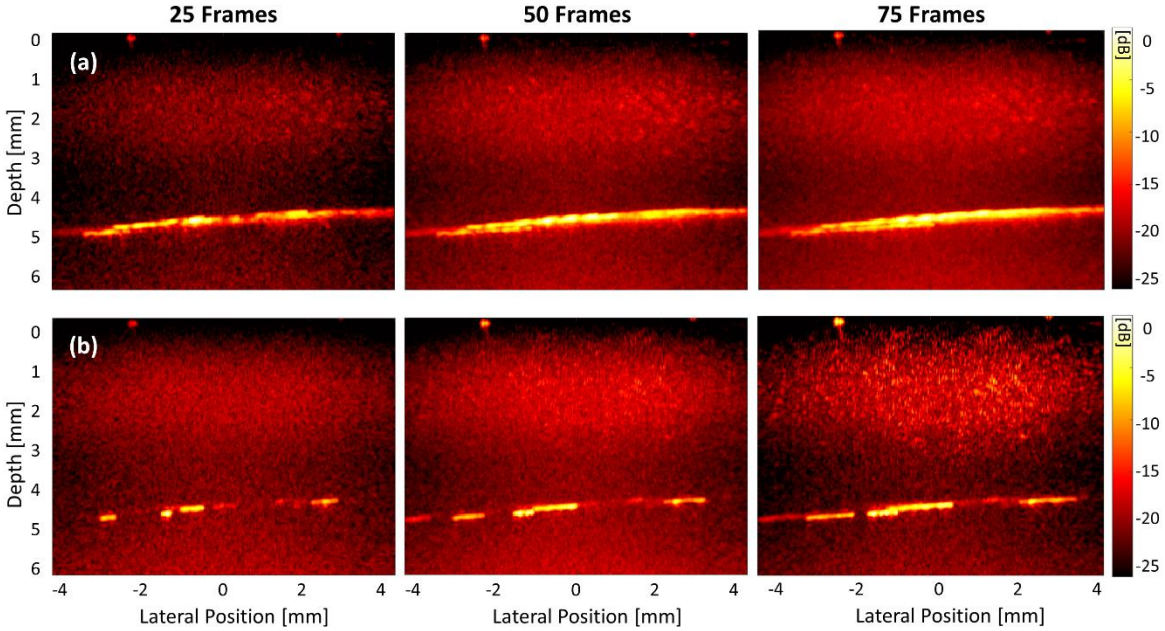

Fig. 2.10. SVD processing of HFUS ultrafast Doppler data under different ensembles size. (a), HFUS ultrafast data acquired from the micro-flow channel with flow speed of 30 mm/s (b). HFUS ultrafast data acquired from the micro-flow channels with flow speed of 10 mm/s.

In conventional Doppler imaging based on focused line-by-line acquisition approach, the major limitation in detection of slow-flow signals is the acquired number of Doppler ensembles which affects the sensitivity and signal ratio. However, the advent of ultrafast acquisition overcome such limitation and enhances the Doppler sensitivity. The number of Doppler ensembles increases so that the conventional temporal clutter filters such as

IIR filter can extract the slow-flow signal. However, these filters rely on the assumption of temporal discrimination of tissue and flow signal, which becomes invalid in terms of slow-flow signal extraction where the tissue signal and the flow signal has overlapped spectra. To compare the processing of ultrafast data with SVD clutter filter and conventional temporal clutter filter, the same dataset was processed with conventional temporal high-pass IIR Butterworth filter as shown in Fig. 2.11, where the spectral content of clutter signal and flow signal can be clearly observed. The higher frequency component represents the clutter signal and lower frequency components represents flow signal. The cut-off frequency for high-pass IIR filter was chosen at the frequency of 140 Hz as shown in Fig. 2.11 to extract the low amplitude flow signal. It was observed that the blood and tissue signal can be separated by conventional temporal clutter filtering, as shown in Fig. 2.11 the energy of the flow signal can be seen as the mapped stream of the BMF in the micro-flow tract. It was also specified to observe that the higher frequency components in the spectral band of (130 – 190 Hz) with low amplitude signal, which is considered as flow signal in power Doppler imaging. However, it can be also observed the energy of the extracted flow signal is lower with degraded image contrast in comparison to the one processed with SVD clutter filter shown in Fig. 2.10. It also shows that some of the flow energy was lost or filtered out by the temporal filter. These observations illustrates that the SVD clutter filter retains the capability to extract the slow flow efficiently with better imaging contrast than the temporal based conventional filters. Quantitatively measurements shown in Fig. 2.12, also supports the findings. The signal to noise ratio (SNR) and contrast to noise ratio (CNR) was measured from both power Doppler images processed with temporal high-pass IIR Butterworth filter and the global SVD filter. These measurements indicates that the signal ratio and image contrast were higher with SVD processing in comparison to the temporal cluster filtering as illustrated in Fig. 2.12.

Although, the presented framework for visualization of superficial micro-vessels successfully visualized the superficial micro-structures in flow phantom experiments. The limitation of present framework is that the imaging sequence encompassing HFUS ultrafast Doppler imaging and spatio-temporal clutter filter was optimized on straight flow micro-channels. However, the morphology of micro-vessels in *in-vivo* conditions are characterized by its tortuosity and branched structures. Therefore, an advanced and

updated micro-flow phantoms with complex vascular structure would be required to optimize the imaging sequences in an efficient visualization of superficial microvasculature. Furthermore, enhancement in signal processing algorithms is yet to be explored by integrating the SVD clutter filter with noise elimination approaches for an efficient visualization of cutaneous vasculatures. In the following chapter, we will discuss about the amendments in the present imaging framework.

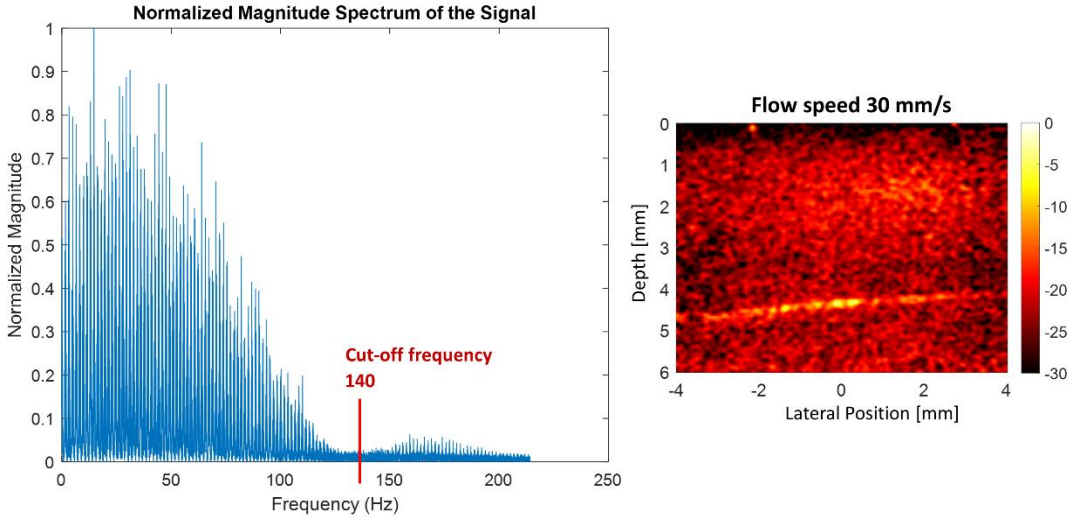

Fig. 2.11. Conventional temporal high-pass clutter filtering of HFUS ultrafast data acquired from micro-flow channels with flow speed of 30 mm/s.

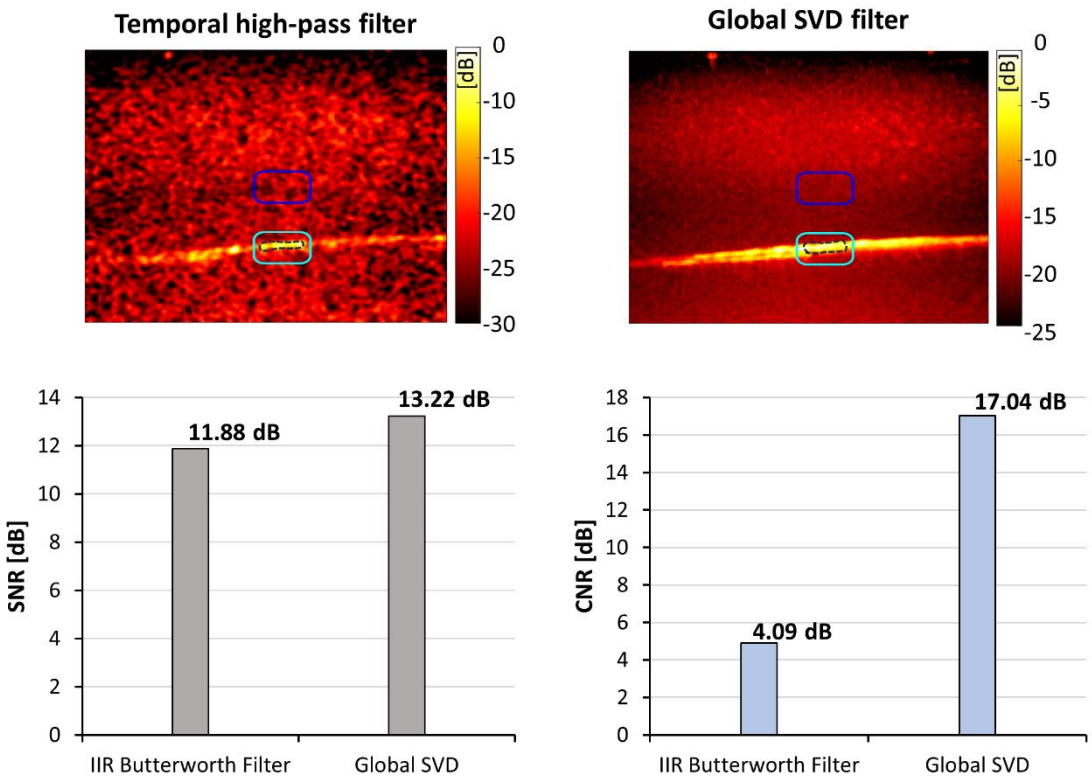

Fig. 2.12. Quantitative comparison between the temporal high-pass filter and global SVD filter in the metric of signal to noise ratio (SNR) and contrast to noise ratio (CNR).

Chapter 3

Fabrication of Micro-Flow Phantom to Simulate Superficial Complex Micro-vessels

This chapter presents a novel fabrication protocol to develop a micro-flow phantom. The phantom was devised to mimic the superficial micro-vessels at shallow depth of 2-5 mm. The proposed Y-shaped geometry of micro-structure simulates the intricate morphology of micro-vessels.

In general, the morphology of micro-vessels are not characterized as straight channels rather these tiny structures recognized by intricate branching and tortuosity. In pathological conditions such as angiogenesis in tumors, neovascularization appeared to nourish the cancerous cells. Those phenomenon led to the development of branched structures of micro-vasculature.

3.1. Importance of Micro-Flow Phantoms/Literature Review

In ultrasound vascular imaging, phantoms are commonly used as investigative tool to characterize and calibrate the imaging system[56]. These simulation test beds usually help to verify the performance of imaging sequences to meet the quality standards. Flow phantoms are considered as a tissue slab with an embedded vascular structure in defined shape and position to mimic the vasculatures in required *in-vivo* investigative conditions. These tools are needed to simulate the controllable experimental conditions, allowing the testing and validation of hypotheses, and optimization of imaging sequence. In different research studies[57-60] of ultrasound imaging, various models of vascular flow phantom with different geometries have been reported to mimic the embedded vascular structures in different applications. However, when it comes to superficial micro-flow phantoms, only straight micro-flow channels have reported[61-65] in literature due to complication in fabrication process. Different approaches have been investigated by several groups to fabricate the micro-flow phantom. Grande-Perret et. al[62] presented homemade phantoms made from silicone materials embedded with straight channel of diameter ranging from

147 – 436 µm. Phantoms made of TMM encapsulating finer micro-tubes ranging from 200 to 700 µm in diameter, was also designed[66-67], but the walls of these tubes produced reflection artifacts in ultrasound imaging. Dialysis cartridge with finer straight channels for the quantitative evaluation of blood perfusion has also been reported as micro-flow phantoms[66]. Cartridge has few hundred capillary-like cellulose tubes, of diameter 200 µm to simulate the physiological conditions of micro vascularization. However, the cellulose tubes of cartridge becomes porous over time as a result only the tubes at the top of the cartridge can be imaged. The summarized illustration of presented approaches for micro-flow phantom fabrication presented in Fig. 3.1.

New research studies[68-69] demonstrated the usage of micro-fluidic chips appears to be a propitious solution to create a microvasculature phantom which mimics the complex microvascular networks. As micro-fluidic chips are based on polydimethylsiloxane (PDMS) material, they encounter two major issues: (i) the speed of the sound in PDMS is 1076 mm/s while speed of sound in human tissue is 1540 mm/s (ii) the highly absorbent material nature which limits the depth penetration. On the other hand, PDMS based devices are difficult to fabricate due to complex procedures involving photolithography.

To characterize and validate the imaging sequences of emerging ultrasound techniques in high-frequency ultrasound, it is necessary to adapt flow phantoms to replicate the intricate morphology of superficial micro-vessels and blood flow patterns. A key consideration in flow phantom design is to ensure that the fabricated vessels are similar in size and positioned at depths comparable to those of vessels under investigation in *in-vivo* conditions. Recently reported[70] medical gelatin, as considerable TMM to cast the vascular model created via soldering micro-wires in complex geometry up to depth of < 20 mm. A major challenge in casting with such a protocol at superficial depth < 5 mm is to remove the wires cautiously without damaging the phantom. In order to create an intricate structure which mimics the superficial micro-vessels, there are two things we need to consider. (i) the depth position, as superficial micro-vessels are considered at shallow depth of <5 mm, and (ii) must be in complex structure not a straight tube.

Here, we present a novel fabrication protocol of micro-flow phantom specifically designed for HFUS imaging of superficial vascular morphologies. Our newly proposed framework addresses the technical limitations and complexities of previous studies. The

flow phantom was designed in bifurcated geometry and physically replicated via resin-based 3D printing. The micro-vascular model was then casted at depth of 2-5 mm in TMM composed of poly-vinyl alcohol (PVA) solution[59] via debossing and bonding approaches to mimic the superficial micro-vasculatures. A determined flow circuit assembly was intact to infuse the blood mimicking fluid (BMF) in the fabricated flow tract to observe the flow dynamics and morphology. HFUS imaging was utilized in both 2D imaging and 3D volumetric rendering to visualize the bifurcated flow channel and evaluate its characteristics. The key technical merit of the proposed protocol is that it is developed as a bifurcated micro-flow phantom in Y-shape geometry at a depth of less than 5 mm resembling the superficial micro-vessels. In addition, it is to be noted that flow tract was wall-less compared to previously reported studies using micro-tubes which create strong echoes from tubing surfaces. These advancements in phantom fabrication will enable more accurate simulation of complex vascular structures in the skin, allowing the calibration and characterization of ultrasound imaging techniques in the visualization of superficial micro-vessels.

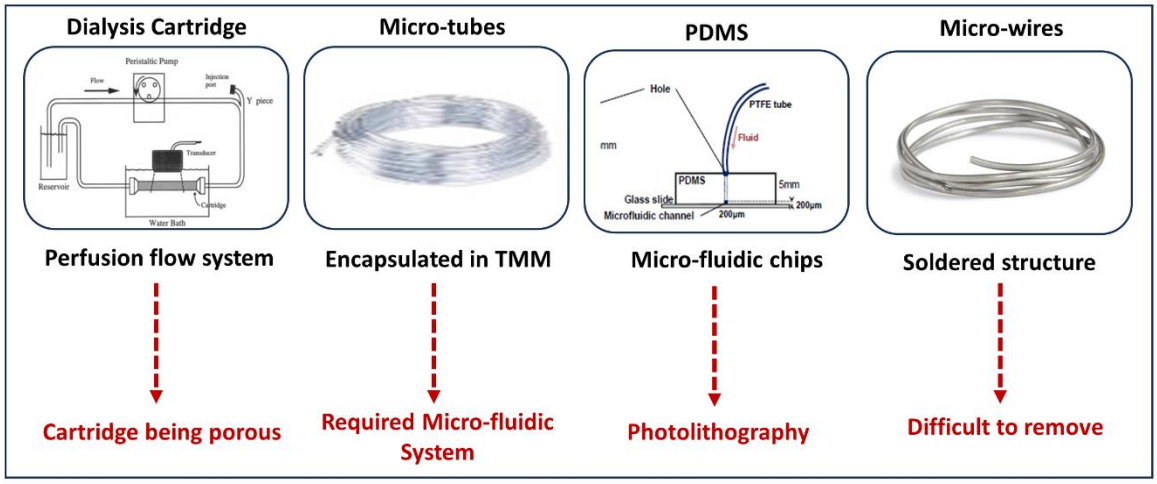

3.1. Literature summary of micro-flow phantom fabrication approaches.

3.2. Development of Bi-furcated Micro-flow Phantom

Designed protocol of bifurcated micro-flow phantom comprised on four main steps

as shown in Fig. 3.2. First, the vascular model in Y-shaped with supporting components such as flow connectors and back support was designed in SolidWorks software as illustrated in Fig. 3.3. Later, the physical replicate of the model was printed by utilizing resin-based 3D printer. After getting the vascular model it was mounted in the 3D printed casting case. Later, the tissue mimicking material (TMM) was prepared by following the recipe by Ho et al based on polyvinyl alcohol (PVA). In the next step the PVA was casted around the vascular model into the casting case and followed to freeze and thaw cycle to solidify it as shown in Fig. 3.4. During the thawing cycles, the resin-based mold was removed from the casting case after the 1st thaw episode and dissected the PVA slab into two parts. After dissecting, the vascular impression of model was debossed on one the PVA slab. We utilized that depression as the flow tract structure and inserted the micro-tubes in the obtained depression with the help of IV catheters as shown in Fig. 3.5. After inserting the catheters, a fine layer of PVA cryogel coating was applied on the other flat slab and placed over the micro-tubes inserted slab as a lid to the micro-tubes placed arrangement. The single composite of PVA slab was later subjected to subsequent freeze and thaw cycles. After three thaw episodes, the inserted micro-tubes were removed as shown in Fig. 3.5 from the PVA resulting in the creation of wall-less Y-shaped micro flow structure. To infuse the flow, a designated flow assembly was connected with the casted PVA slab comprised on lure connectors, tubing and IV catheters as shown in Fig. 3.6. The following section will elaborate each step of fabrication in detail.

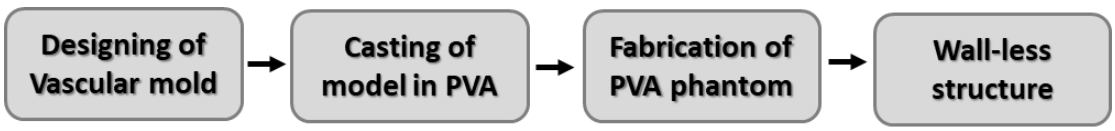

3.2. Flow chart of proposed micro-flow phantom fabrication approach

3.2.1. Preparation of Vascular Model

At first step of fabrication protocol, the vascular model in Y-shape geometry was designed in the SolidWorks software to mimic the intricate micro-vessel morphology. The model was designed into two different diameter dimension (300 micron and 220 micron)

to confirm the reproducibility of the proposed fabrication protocol. The vascular mold structure was comprised on three branches, the parent branch and two daughter branches as depicted in Fig.3.3. The straight parent branch with length of 14 mm was divided into two daughter branches of size 10.5 mm, positioned at a 17-degree of bifurcation angle with length of 6 mm and equal spacing. Also, the supporting components and back support slab was also designed in the model structure. The dimension of supporting connectors was 3 mm on parent branch and 2 mm on daughter branches with a length of 5 mm respectively. The back support slab was included in the vascular model because the printing of vascular structure in micro-dimension was quite cumbersome. The chances of model deterioration were quite high during the printing process due to stand alone of vascular model. Therefore, back support was designed with same dimensions of length as of vascular model, to support the mold in vascular model as shown in Fig.3.3(b)

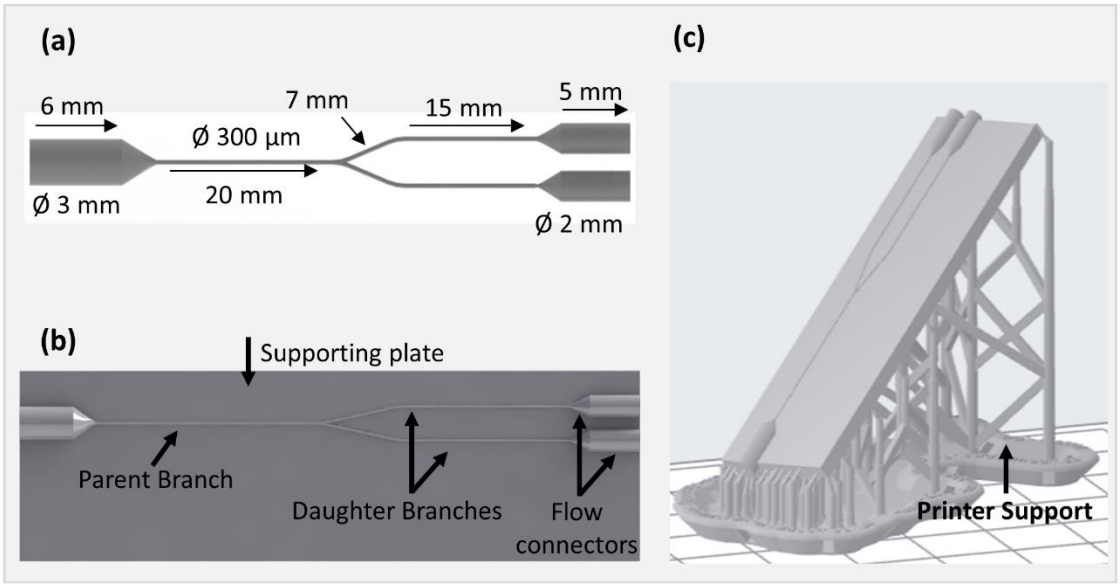

3.3. Designing and 3D printing of bifurcated model. (a). Y-shaped geometrical design of micro-flow tracts accompanied with flow connectors. (b). Size-matched back supporting plate and bifurcated model. (c). Using Preform printing software, a supporting base was added during the printing instructions.

3.2.2. 3D Printing of Vascular Model

The second step in the development of phantom fabrication was 3D printing. The physical replicate of vascular model designed in the respective software was printed by utilized the utility of resin-based 3D printer. To initiate the physical replication process, the SolidWorks software file was exported in STL (stereolithography) format which was later imported to Preform software to determine the printing instructions. The Preform software is the designated printing software accompanied with resin-based Form 3+ printer. To initiate the printing instructions, at first the orientation of the vascular model was adjusted to vertically tilted position in the preform software, specifically with the vascular mold facing upwards to maintain the printing resolution of 3D printer (25 μm). Later, the printing parameters such as layer thickness = 25 μm and resin infill percentage = 100% were selected. To keep the model intact during the printing process, a raft type support was generated to ensure that the printed material adhered to the desired position. That support base from the actual model was easily detached after printing. Once all the parameters was finalized, the printing job was uploaded to the 3D printer for execution. The printer utilized the low force stereolithography (SLA) technique, which involves building the model within a vat of liquid photopolymer resin using ultraviolet light. This process cured each layer of the model as per the loaded file, resulting in a precise printed model. At the end of the printing process, the printed flow tract model underwent an isopropyl alcohol wash for approximately 10-15 minutes to ensure the complete removal of resin particles. After cleaning the process, the model was placed under UV light to further solidify the resin and ensure its stability.

3.2.3. Casting of Model in Tissue Mimicking Material (TMM)

In order to create a tissue slab with acoustic properties similar to that of human tissue with embedded wall-less vasculature, a polyvinyl alcohol (PVA) cryogel mixture was prepared. The composition of the mixture was based on three main components: 10% (by weight) PVA powder (341584; Sigma-Aldrich), 3% fine graphite particles (282863; Sigma-Aldrich), 0.3% potassium sorbate (85520; Sigma-Aldrich). The cryogel mixture

was prepared by taking 500 ml (85%) distilled water in a beaker and lie down on digital hotplate magnetic stirrer. Once the temperature of water reached 80-degree C, PVA powder was added into the beaker in chunks to dissolve it properly in water. Along with PVA, potassium sorbate was also added in the solution as a preservative. The magnetic stirrer mixed the mixture for around an hour to completely dissolve the PVA in water. Later, graphite particles were added in the mixture as ultrasound scatterers. After adding the graphite, set the mixture to stir for around 30 minutes to completely dissolve all the components properly in consistency. Finally, turned off the hotplate and left the cryogel mixture for overnight at room temperature for degassing.

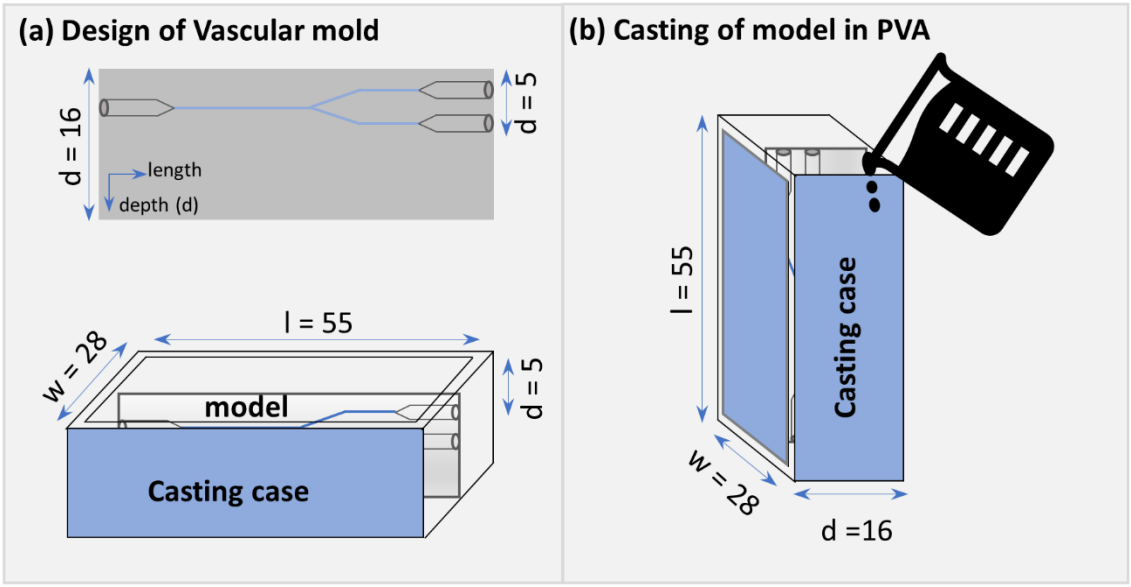

3.4. Design and casting of PVA flow phantom. (a). Illustration of Y-shaped vascular model. (b). Casting of model in PVA cryogel.

In the meantime, the casting case was designed using the same SolidWorks software as described earlier. The dimensions of the casting case were in alignment with the dimensions of vascular model such as depth, height, and width of the case in order to cast the flow tract structure at the depth of 5 mm as shown in Fig. 3.4. The physical replicate of casting case was appeared by 3D printer (Tiertime UP 300), and polylactic acid (PLA) thermoplastic (PolyLite, PolyMark) was used as printing material to print the casting case.

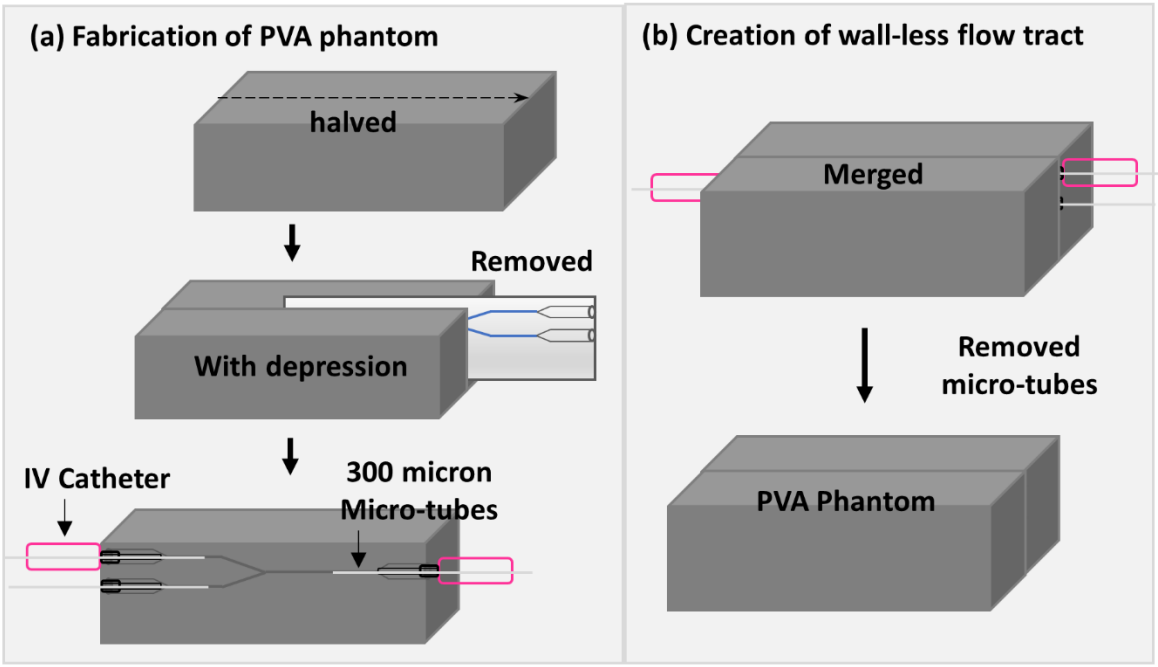

3.5. (a). Fabrication of PVA phantom and (b). creation of wall-less micro-flow tract.

3.2.4. Fabrication of PVA Phantom

Once the vascular model, PVA cryogel mixture, and the casting case was prepared. The model was mounted into the casting process as shown in Fig. 3.4. The prepared PVA cryogel mixture was poured slowly into the casting case around the mounted vascular model as illustrated in Fig. 3.4(b). Later the PVA casted case was underwent through freeze and thaw cycles. In the proposed approach of micro-flow phantom fabrication, after the 1st freeze and thaw cycle, the mounted vascular model was detached from the PVA casted slab and halved the PVA into two corresponding parts as shown in Fig. 3.7(e). By doing so, one of the parts of slab exhibited the bifurcated Y-shape structure of vascular mold debossed on its surface as shown by while arrow in Fig. 3.7(e). By leverage this depression of vascular structure of the flow tract, micro-tubes were inserted in the depressed structure with the help of IV catheter as shown in Fig. 3.7(f). To do so, we designed an alignment tool using the same SolidWorks software and 3D printer. The purpose of using alignment tool Fig. 3.7(h) was to hold the IV catheter securely on

respective inlet and outlet of the PVA slab to precisely insert the micro-tubes into the debossed vascular branches. The tool was featured with sized matched holes on both sides with a diameter of 3 mm to hold the IV catheters as shown in Fig.3.7(h). 300 μm Perfluoro alkoxy (PFA) micro-tubes were inserted into each branch of vascular structure and precisely adjusted into the debossed structure manually. After successfully adjusting the micro-tubes within the slab to retain the vascular flow structure geometry, the other flat slab was layered with fine coating of PVA cryogel mixtures and carefully placed over the top of the debossed PVA slab as depicted in Fig. 3.7(i). The merged PVA composite was later subjected to subsequent freeze and thaw cycles allowing the cryogel to solidify and form a single semi-solid slab that resembled a tissue piece with a Y-shaped vascular structure. As we reached the culmination of three freeze and thaw episodes, the inserted micro-tubes were extracted from each outlet of PVA composite slab after three thaw cycles as shown in Fig. 3.7(j), resulting in the formation of wall-less lumen that resembles the bifurcated shape flow tract to mimic the superficial vasculature at the depth of less than 5 mm.

3.3. Experimental Setup

3.3.1. Imaging system

In order to image a bifurcated micro-flow tract, high-frequency ultrafast Doppler ultrasound imaging was performed. A 256-channel Vantage Verasonics (Verasonics Inc., Kirkland, WA, USA) research purpose ultrasound platform equipped with L38-22v CMUT (KOLO SiliconWave, USA) linear array transducer was used to transmit and receive the ultrasonic signal. The array aperture has a lateral width of 17.5 mm, axial pixel size of 0.25 mm and lateral pixel size (pitch) of 0.0690 mm, the elevational focus and aperture of 8.0 and 8.1 mm respectively. The transducer was mounted on a transducer holder to smoothly acquire the data from fabricated Y-shaped micro-flow phantom.

3.3.2. Flow circuit assembly

To infuse a flow of blood mimicking fluid (BMF) in the fabricated Y-shaped micro-structure, an efficient and reliable flow circuit assembly was established. It was comprised on IV catheter, infusion pump, luer connectors (1.5 mm inner diameter) and tubing (1.5 mm inner diameter). Each component of assembly was securely connected, ensuring a tight fit among all the components of the flow setup to prevent any potential leaks. Using IV catheter, it was connected with the inlet of the PVA phantom as shown in Fig. 3.6(b). An infusion pump (KD scientific legato 200) was used to infuse the flow in the fabricated flow channel. The utilized BMF has the hemodynamic and acoustic properties such as viscosity (4 cP) and speed of sound (1570 m/s) was in resemblance to that of human blood viscosity (3.5 – 5.5 cP) and speed of sound (1578 m/s)[71,72]. The flow was infused at flow rate of 84 µl/min by assuming the flow speed of 20 mm/s and flow diameter of 300 µm.

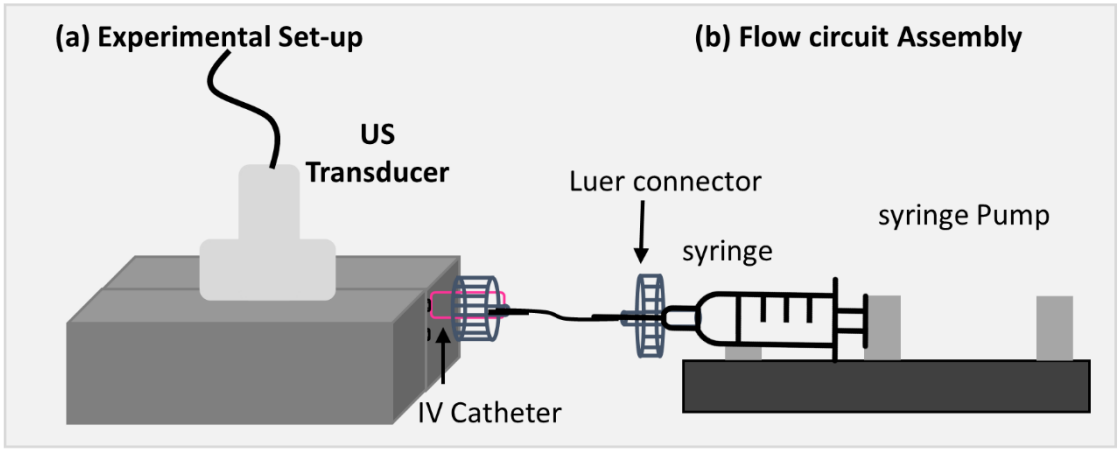

3.6. (a). Schematic of an experimental setup and utilized flow circuit assembly to infuse the blood mimicking fluid into the micro-channel.

3.3.3. Signal Acquisition and Processing

At center frequency of 31.5 MHz, 128 elements of transducer were excited to transmit ultrasonic pulses at pulse repetition frequency of 5 kHz. Ten plane waves with compounding angles ranging from -5 degrees to 5 degrees was chosen to maintain the

image quality. At acquisition time of 0.4 s, 200 beamformed compounded images were acquired to generate a power Doppler image featuring the bifurcated micro-flow tract. The obtained ultrafast dataset of 200 beamformed images were processed with SVD based clutter filtering[24] to extract the desired blood flow signal. Once the signal was filtered, the power Doppler images was generated by computing energy per pixel of detected flow signal.

3.4. Results

Bifurcated wall-less micro-flow phantoms of two different dimensions (300 and 220 μm) were developed. The fabricated flow tract consisted of three branches, a parent branch and two daughter branches, simulating the complex bifurcated vascular morphology. B-mode images shown in Fig.3.8 exhibit insufficient resolution to effectively visualize the minute flow tract. Therefore, to observe the presence of micro-flow tract, BMF was injected into the micro-channel. The passage of flow was clearly discerned upon the activation of syringe pump as shown in the Video 1.

Further, the power Doppler images presented in Fig.3.8(b-e), obtained via SVD-based processing, revealed the visualization of the bifurcated flow tract at depths ranging from 2-5 mm. The high-intensity signal of BMF particles mapped the flow stream and depicted as the bifurcated vascular structure. The intensity profile of the flow exhibited a decreasing trend from the parent branch to the daughter branches as illustrated in Fig. 3.9, demonstrating the nature of hemodynamics.

To quantify the visualized flow tract, the full width half maximum (FWHM) at -6 dB was measured. Intensity profiles were obtained axially at twelve lateral positions of power Doppler image. It was found that the parent branch had averaged diameter of 307 ± 3.7, and 232 ± 18.2 μm and 256 ± 23.3 μm of respective daughter branches 1 and 2 with correspondence to 300 μm of designed structure. In addition, the averaged diameter of designed 220 μm was found to be 232 ± 13 μm of parent branch while 222 ± 9.5 μm and 217 ± 21.8 μm of respective daughter branches 1 and 2 as shown in Fig. 3.9.

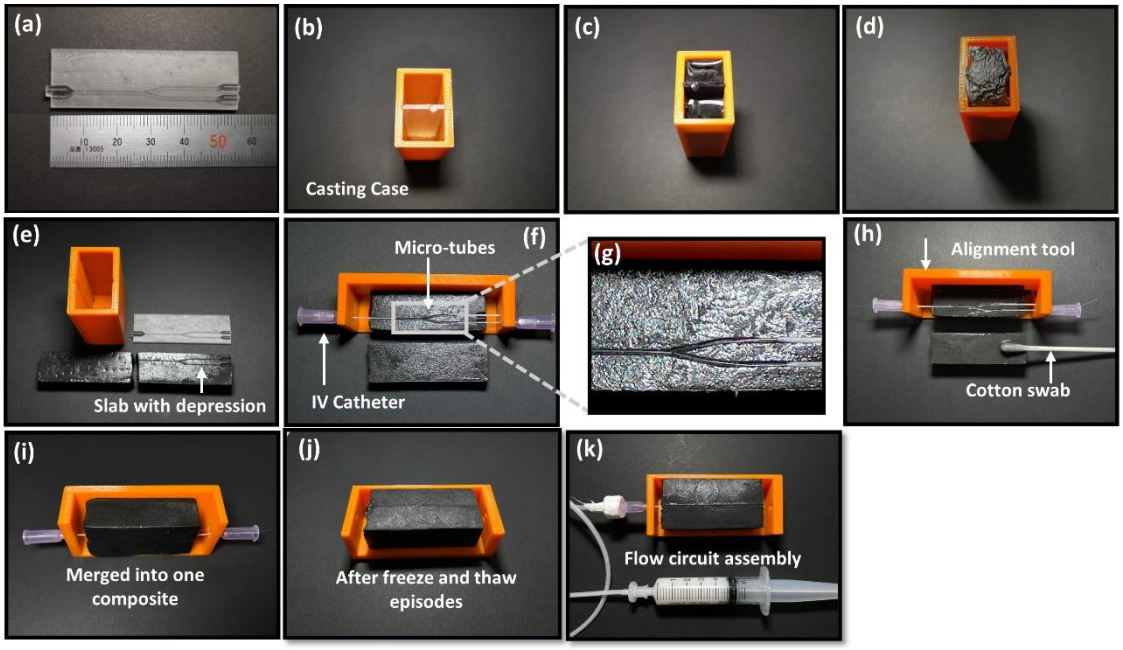

Fig. 3.7. Fabrication process of wall-less bifurcated micro-flow phantom. (a). 3D printed model in Y-shape geometry. (b). Casting case with mounted 3D model. (c). Casting of micro-phantom with PVA mixture. (d). Top view of phantom slab after first freeze and thaw cycle. (e). removing of resin model from PVA slab and appearance of model depression on one of the slabs after dissecting. (f). Fastening IV catheters using an alignment tool for the insertion of micro-tubes. (g). Inserted micro-tubes in the debossed Y-shape structure. (h). Making a specified PVA layer on the other flat slab of Phantom. (i). Merging to create one composite slab embedded with micro-tubes for subsequent freeze and thaw episodes. (j). Removal of micro-tubes after thawing episodes. (k). Connected with flow circuit assembly.

3.5. Discussion

Fabrication of micro-flow phantoms that replicate complex vascular morphology for ultrasound flow studies is widely acknowledged as a challenging endeavor. The development of a bifurcated micro-flow phantom in this study is a significant achievement in the field of micro-vascular modeling. In this study we addressed the concerns of micro-channel fabrication, such as the creation of micro-vessel model and proposed an approach to fabricate a micro-flow phantom for superficial micro-vessels

imaging. We have established the state-of-the-art protocol on how a phantom with a branched micro-channel can be designed and fabricated. This process involves design of vascular model in SolidWorks software, followed by fine 3D printing and casting it in PVA, and fabrication of PVA phantom via inserting micro-tubes to retain debossed micro-structures and removed them to create a void lumen.

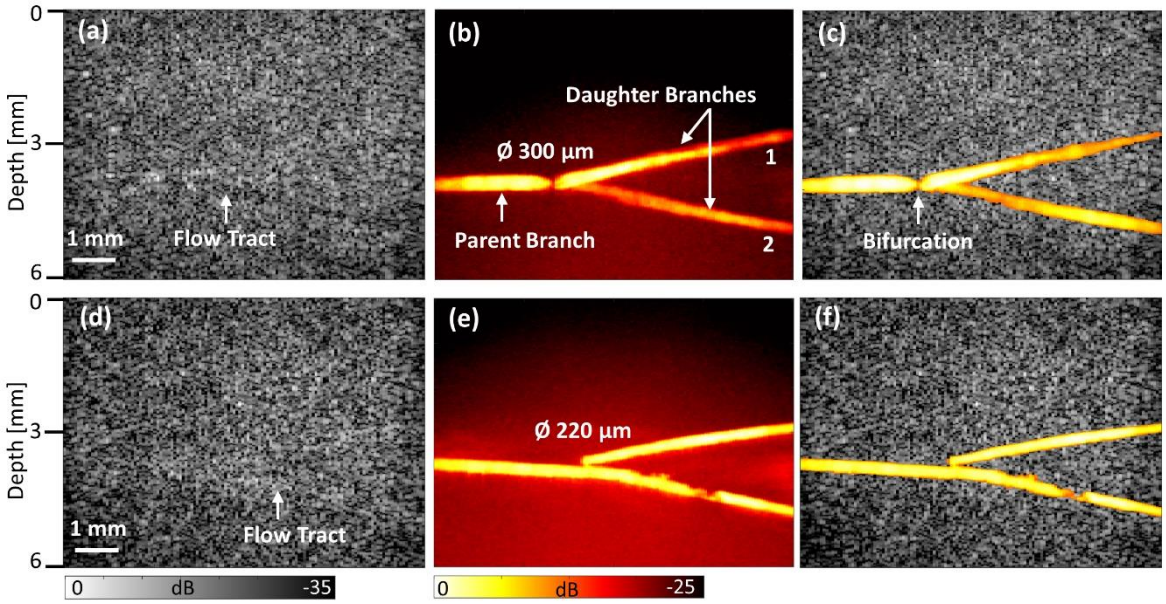

Fig. 3.8. Obtained B-mode, power Doppler, and superimposed images of developed bifurcated micro-flow phantom via high-frequency ultrafast Doppler imaging. (a-c). 300 µm bifurcated flow tract. (d-f). 220 µm bifurcated flow tract.

Traditionally, ultrasound wall-less flow phantoms have been developed by printing a vascular model using PLA printer and casting it in PVA followed by subsequent thaw cycles. Later, the PVA phantom submerged for an allocated time period in some solvent such as chloroform to remove the PLA-based vascular structure, resulting in formation of void flow tract. However, printing vascular model in micron dimension is difficult due to the limitation of PLA-based printers' resolution. Therefore, micro wires and tubes were used in the fabrication process. Some studies proposed PDMS chips as the substitute for the former, due to differences in acoustic properties, PDMS could not be considered as the best choice for ultrasound phantoms. Recently, 3D printing of elastic materials with various mechanical properties has become feasible in creating structures with micron-

dimensions utilizing the SLA techniques. The presented methodology utilized the SLA-based resin 3D printer to create the vascular model in bifurcated geometry with a minimum printing limit of 200 µm in diameter. However, the resin was not dissolved in any solvent to remove the model after casting, to overcome such challenge we proposed an approach to halved the PVA slab after 1st episode of thawing cycle and detached the resin model from the slab resulting in creation of vascular depression on halved slab. Inserting micro-tubes in vascular shaped depression solved the mystery of dissolving resin in any solvent to create a wall-less void lumen with accurately designed dimensions. This strategic insertion of micro-tubes in debossed Y-shaped structure served to preserve the intended shape during the bonding process. After subsequent thaw cycles, inserted micro-tubes were removed from the PVA composite, led to the formation of wall-less micro-structure in the desired Y-shaped geometry. By exploiting the properties of the micro-tubes and the thawing process, the study achieved a seamless transition from the resin vascular model to the desired wall-less micro-structure, providing an advanced solution for the fabrication of intricate vascular structures.

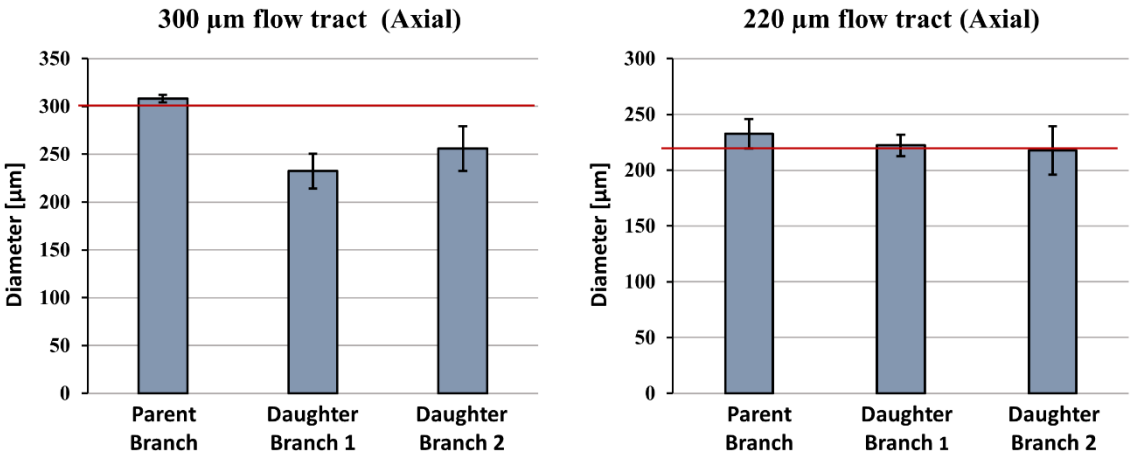

Fig. 3.9. Quantitative measurement of averaged detected diameter axially at 12 different lateral position from respective power Doppler images.

As a proof of concept, our prototypical micro phantom was put into operation with flow circuit assembly, and experiments were performed with HFUS ultrafast imaging. The corresponding flow dynamics at flow rate of 84 µl/min were imaged using an emerging

ultrafast Doppler technique based on plane wave imaging. The passage of flow in bifurcated tract was observed in B-mode (Video 1). To gain more detailed insights into the flow characteristics, power Doppler images were computed using SVD-based filtering algorithm, successfully pictured the presence of bifurcated flow tract at depths ranging from 2-5 mm. Furthermore, the intensity profiles demonstrated a decreasing trend as the flow (BMF) moved from the parent branch to the daughter branches, elucidated the flow transitioning from high-intensity map to low-intensity. The FWHM measurements in Fig.3.9 found to be measured axially average of 307 ± 3.7 μm with correspondence 300 μm of designed model and inserted micro-tubes. It provides the quantitative evidence about the accuracy and reliability of the fabrication protocol. The present fabrication approach faces certain challenges such as shown in Fig. 3.8 power Doppler images, there is slight discontinuity in vascular shape results from errors during the bonding process. Also, designing of more complex multi-branched tortuous geometry needs more attention in inserting micro-tubes in dedicated morphological shape with potential approach in future study.

Conventionally, straight channel micro-flow phantoms used in optimization of imaging sequences lacks the anatomical realistic conditions in visualization of superficial micro-vasculatures. In general, vasculatures are characterized by intricate branching and tortuosity, and pathological conditions such as angiogenesis led to the development of branched structures. To bridge this gap, proposed bifurcated geometry supports the *in vivo* realistic branched vascular morphology. Experimental observations gained from this study substantiate its merit as an investigative tool to measure ground truth measurements in optimization of HFUS ultrasound imaging techniques.

Chapter 4

Two-dimensional Imaging of Superficial Micro-vessels

This chapter presents the imaging of superficial micro-vessels utilizing developed imaging framework. *In-vivo* experiments were performed to visualize superficial micro-vessels in index finger at three different positions to evaluate the performance of the imaging framework. Acquired HFUS data was processed with SVD clutter filter to extract the desired flow signal. Later, a top-hat transform morphological filter was implemented on SVD processed power Doppler images to suppress the system generated background noises and enhances the image contrast and visibility of superficial micro-vessels.

4.1. Experimental Setup

An experiment setup described in chapter 2 was used to perform the *in-vivo* imaging of superficial micro-vessels. Vantage 256 channel system (Verasonics Inc., Kirkland, WA, USA) equipped with high-frequency linear array probe (L38-22v, KOLO Medical, San Jose, CA, USA) was used to transmit and receive the ultrasonic signal at center frequency of 31.5 MHz. 128 elements of transducer was used to transmit ten plane waves at different steering angles (-10 degree to 10 degree). 500 beamformed compound images were generated at pulse repetition frequency of 5 kHz. Acquisition parameters listed in Table 4.1 was used to perform superficial micro-vessels imaging.

To validate the imaging performance of the devised imaging framework *in-vivo* experiments were conducted utilizing the HFUS ultrafast Doppler imaging. *In-vivo* ultrafast data was acquired from three different position of the index finger as shown in Fig. 4.1. Several trial experiments were performed, and among them three datasets were chosen to further processing. Acquired ultrafast datasets from three different anatomical positions of index finger were (1). Doral side of nail bed, (2). Distal phalanx in palmer position. (3). Distal side of phalanx in palmar position. These acquired HFUS dataset were further processed with singular value decomposition (SVD) based clutter filtering.

The processing framework described in chapter 2 was used to extract the desired flow signal in visualization of superficial micro-vessels.

Table 4.1. Acquisition parameters of HFUS ultrafast ultrasound imaging.

Parameter	Value
Probe	L38-22v CMUT Probe
Number of elements	128
Pitch	0.0690 mm
Central frequency	31.5 MHz
Sampling frequency	41.6 MHz
Excitation pulse	3 cycles
Speed of sound	1540 mm/s
Pulse repetition frequency (PRFmax)	5000 Hz
Doppler angle	10°
Doppler Ensemble	**500**
Compounding transmissions	10

Fig. 4.1. Imaging objects for HFUS *in-vivo* ultrafast ultrasound imaging.

4.2. Singular Value Decomposition of Ultrafast Ultrasonic Data

To perform SVD on raw spatio-temporal ultrafast data which is in the form:

$$s(x, z, t) \qquad (1)$$

Where, x stands for lateral dimension, z stands for depth in the medium and t stands for acquired temporal samples. This spatio-temporal matrix corresponds to three dimensional raw ultrafast data which can be represent as:

$$n\_x \times n\_z \times n\_t$$

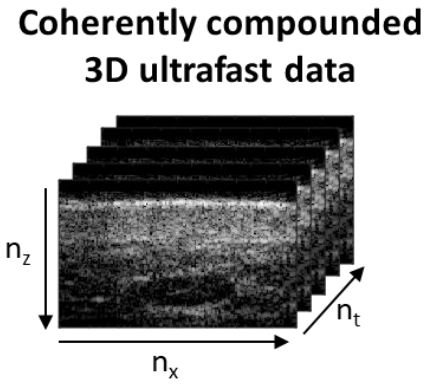

Where n_x, n_z, n_t are the number of spatial samples along lateral direction, depth position and along temporal direction, respectively. To perform SVD on spatio-temporal matrix, of raw ultrasonic data, it should convert into two dimensional casorati matrix by transforming the time series data in to 2-D space-time matrix form as shown in the Fig. 5.2.

$$s(x \cdot z\,,\ t) \qquad (2)$$

Decomposition of 2-D rearranged matrix of ultrafast data by SVD results in the creation of three new matrices as presented in eq. 3.

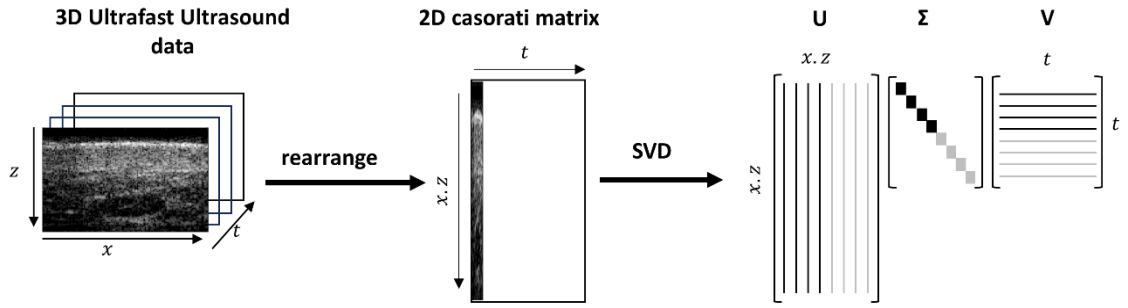

Fig. 4.2. Singular value decomposition of ultrafast data

$$S = U\Delta V^{*} \qquad (3)$$

Where U represents the spatial singular vector and V represents the temporal singular vector and Δ is a non-square diagonal matrix of singular values. SVD is the decomposition of the matrix S in to a weighted, ordered sum of separable matrices A_i which is the outer product of two vectors U_i and V_i as shown in eq. 4.

$$S = \sum_i \lambda_i A_i = \sum_i \lambda_i U_i \otimes V_i \qquad (4)$$

U_i and V_i are the i^{th} columns of corresponding SVD matrices S, and λ_i are the ordered singular values. The main assumption in this approach is that tissue and blood signal leave different signatures on ultrasound data which occupy in different singular values. While the tissue signal is highly spatially coherent and supposed to be quite similar in all the neighboring pixels of the imaging field then the blood signal. Based on that assumption clutter rejection could be performed by setting the specified threshold value in selecting the singular values by assuming that the tissue signal could be gathered in the higher singular values as presented in [21] and the blood signal should be found in the lower singular values.

$$\lambda_1 U_1 \otimes V_1 + \cdots + \lambda_t \lambda_t \otimes V_t \qquad (5)$$

$$PW_{(x,z)} = \int | s_{blood}(x,z,t)|^2 \, dt \quad (6)$$

The filtered signal at specified threshold value is again rearranged to original matrix form and calculated the average intensity per pixel to produce the Power Doppler images as presented in [21].

4.3. Background noise removal

The matrix value decomposition based clutter filtering of rich spatiotemporal data matrix of ultrafast ultrasound effectively discriminate the tissue signal and blood flow signal vis singular value thresholding as presented in chapter 2 and 3 flow phantom experiments. However, apart from the blood flow signal, there is an additional component in the form of additive noise within the weakly correlated sub-space of spatial covariance matrix. These noise components predominantly stem from electronic front-end such as amplifiers and time-gain-compensation (TGC) circuitry[26]. In the computation of power Doppler images, due to statistical independence of noise and blood signal, the local image intensity results from the direct summation of the blood power and background noise power. Consequently, any decrease or increase in the local background noise power is directly reflected as an additive background, subsequently altering the intensity levels at which vessels achieve optimal visibility. When a high TGC is employed in the imaging sequence, there is progressive increase in noise power. This leads to vessels appearing with higher intensities, accompanied by elevated background noises[48]. A method proposed by Pengfei et al[26] suggests noise field truncation using high and low-order singular value thresholding based on local data singular value truncation. However, a study[49] highlights the observations that noise and blood signal exhibit similar energy decay rates in the singular value domain. Consequently, truncation with low-order singular value may inadvertently remove a portion of the valuable blood energy, potentially degrading vessel image contrast. Additionally, when the blood signal has very low amplitude, it can become submerged beneath the noise amplitude. Therefore, in the

filtered image only the noise field is discernible, with no detection of the signal. To address this issue of denoising the system generated noise field from ultrafast ultrasound data, several post-processing algorithms have been reported as summarized in Table 4.1.

In this study, we have implemented a background noise removal technique proposed by Bayat et al[48]. That approach is based on top-hat filtering, which aims to eliminate the slowly varying noises from the power Doppler images processed via singular value decomposition. Top-hat filtering is a morphological filter operation commonly employed in image processing to suppress background noise signals while preserving the desired features of objects in digital images. To enhance the visibility of vascular structures with minimize background noise, we applied top-hat filtering directly to the blood vessel images. The top-hat filtering process is represented as follows:

$$I_f = I - I \circ SE \qquad (7)$$

where I and If denotes the input and output images respectively, SE represents the structuring element that defines the filter property and ◦ denotes the opening operation as an image processing. In this study, we utilized a structuring element with a disk shape of 45 × 45 pixels for all datasets.

Table 4.2. Literature summary of post-processing algorithms for denoising of background noise in SVD processed power Doppler images.

Post-processing (denoising) methods	Reference
High and low order SVT	30
Noise equalization	26
Morphological Filtering	48
Hessian enhancement	50
Non-local means filtering	51

4.4. Results

The power Doppler images shown in Fig. 4.3 were generated after SVD clutter filtering of HFUS ultrafast data obtained from three different positions of index finger. Anatomical identification of skin layers and internal structures was clearly observed in the obtained B-mode images shown in Fig. 4.3. These identification illustrates the outline of the skin layers at the very superficial depths and the prominent visualization of nail bed was observed in Fig. 4.3(a) B-mode at the dorsal side of the index finger as also indicated by white arrows. Also, the morphology of skin layers such as high echogenic epidermis layer and dermis layer were identified and clearly observed in B-mode image. However, it was quite difficult to visualize the any appearance of micro-vessels in the obtained B-mode images. These tiny vessel were clearly observed and perceived as high intensity mapped flow signal of micro-vessels in the dermis layer of skin as shown in processed power Doppler images in Fig 4.3.

Extraction of micro-vessels flow signal and truncation of clutter (tissue) signal with SVD based filter clearly visualize the superficial micro-vessels at the very superficial depths of 3 mm. However, there are certain background noises which retain the processed power Doppler images which degrades the image contrast and the micro-vessels visibility. SVD clutter filter was just utilized to remove the clutter signal, the filtered out matrix was the combination of the flow signal and the noise signal. These noises was suppressed and removed by the implementation of top-hat morphological filter which retain the potential to suppress the linear background noises and preserved the flow signal. As shown in Fig. 4.4, application of top-hat filter significantly removes the noises improved the visibility of superficial micro-vessels.

Further, quantitatively the diameter of the visualized superficial micro-vessels in the dermis layer of skin was calculated from three different vascular points as shown in Fig. 4.5. From these obtained intensity profiles, full-width-half-maximum was measured at -6B. From that measurements the minimum detected diameter of superficial micro-vessels was observed 51 μm as shown in Fig. 4.5.

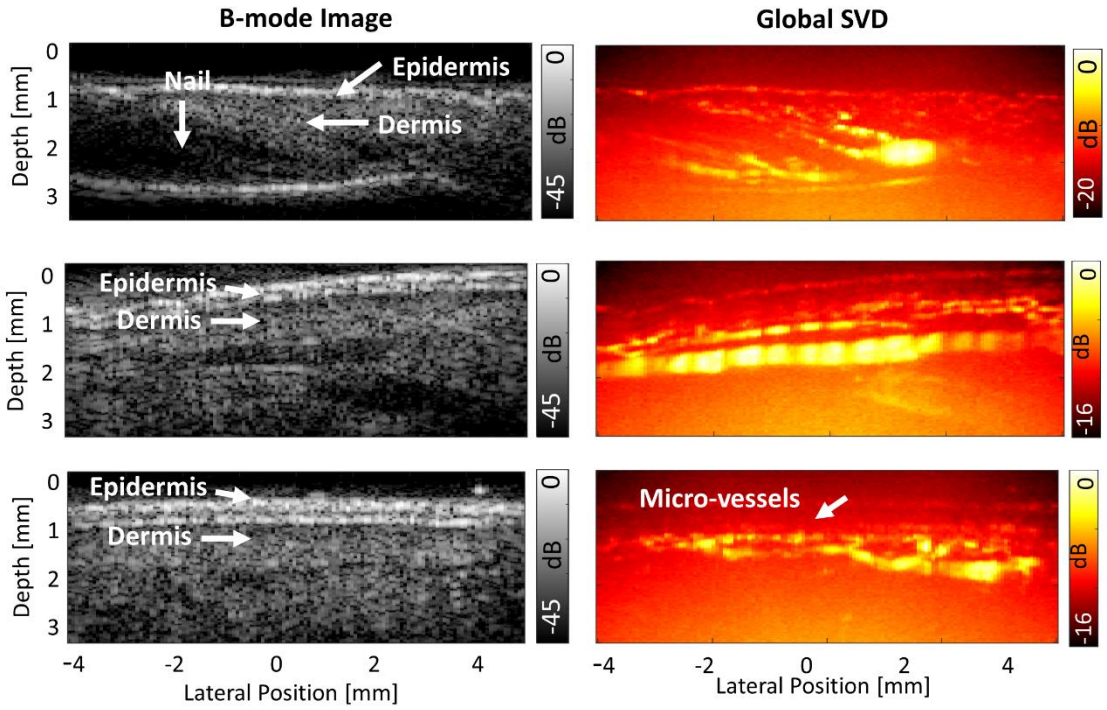

Fig. 4.3. Obtained power Doppler images from three different positions of index finger. (a). Doral side nail bed. (b) Distal phalanx in palmer position. (c). Side distal phalanx in palmar position.

4.5. Discussion

After obtaining an insightful results from *in-vitro* micro-flow phantom experiments presented in chapter 2 and 3, *in-vivo* imaging was performed to evaluate the performance of HFUS imaging system with center frequency of 31.5 MHz. High-frequency ultrafast ultrasound imaging was conducted on tip of index finger to visualize the superficial micro-vessels. In the processed power Doppler images shown in Fig. 4.3 revealed the presence of micro-vessels in the dermis layer of skin up to the very superficial depth of 2 – 3 mm. As indicated by white arrows in B-mode images, the skin morphology was discernible as high-echogenic layer as epidermis and less echogenic layer as dermis layer. However, the tiny micro-vessels were not visualized in B-mode images due to the insufficient resolution. However, these tiny micro-structures were clearly appeared as

mapped micro-circulation in the SVD filter processed power Doppler images. SVD clutter filter truncates the tissue signal via singular value thresholding and filtered out the signal comprised on blood flow signal and noise signal. The weak correlated noise signal appears as background noises, which affects the visibility of micro-vessels and image contract. To remove such noises, top-hat morphological filtering was implemented in the imaging framework. Fig. 4.4 shows the power Doppler images processed with global SVD approach and combined approach of global SVD + top-hat filtering. The visibility of micro-vessels and image contrast was increased significantly after the application of top-hat filter which eventually suppressed the background noises. The present algorithm of image processing comprised on HFUS ultrafast Doppler and global SVD + top-hat filtering efficiently extracts the micro-flow signal and suppressed the background noises in visualization of superficial micro-vessels.

Visualization of micro-vessels in the dermis layer at three different positions of index finger illustrates the potential and resolvability of the proposed imaging framework. The system is capable enough to visualize the micro-vessels with minimum diameter of 51 µm which resembles reported diameters of superficial micro-vessels in skin [1]. However, in the progression of the diseases such as in the case of skin cancer (melanoma) or Raynaud's phenomenon, as the diseases progress it deteriorates the surrounding tissues and the vasculatures. The cutaneous vascular network comprised on the micro-vessels which are present in the dermis layer of the skin, and the smaller vessels which presents in the deeper layers of the skin. Deterioration in the micro-vessels affects the functionality of smaller vessels and vice versa. Visualization of these complete cutaneous vascular network provide a complete information of diseases progression and assist in the diagnosis and treatment of the disease. In the next chapter, advancements in the imaging framework have been implemented to visualize the comprehensive visualization of complete cutaneous vascular network (micro-vessels and smaller vessels).

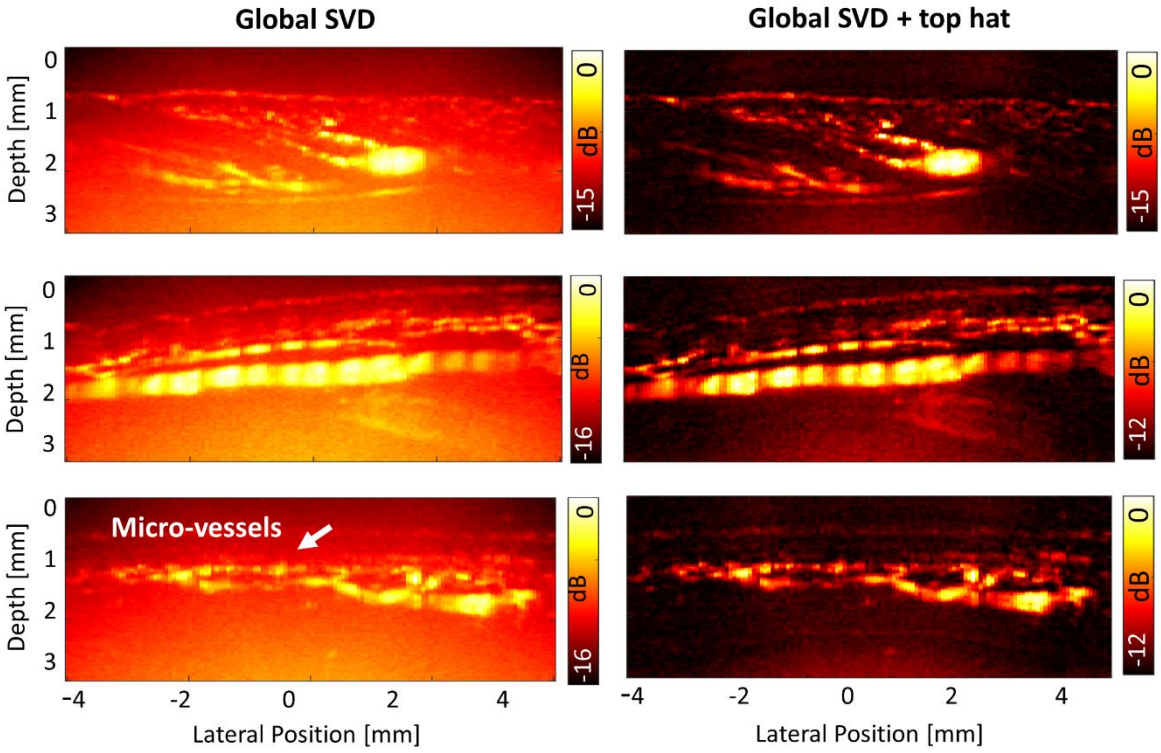

Fig. 4.4. Obtained power Doppler images processed with Global SVD and Global SVD + top-hat morphological filtering.

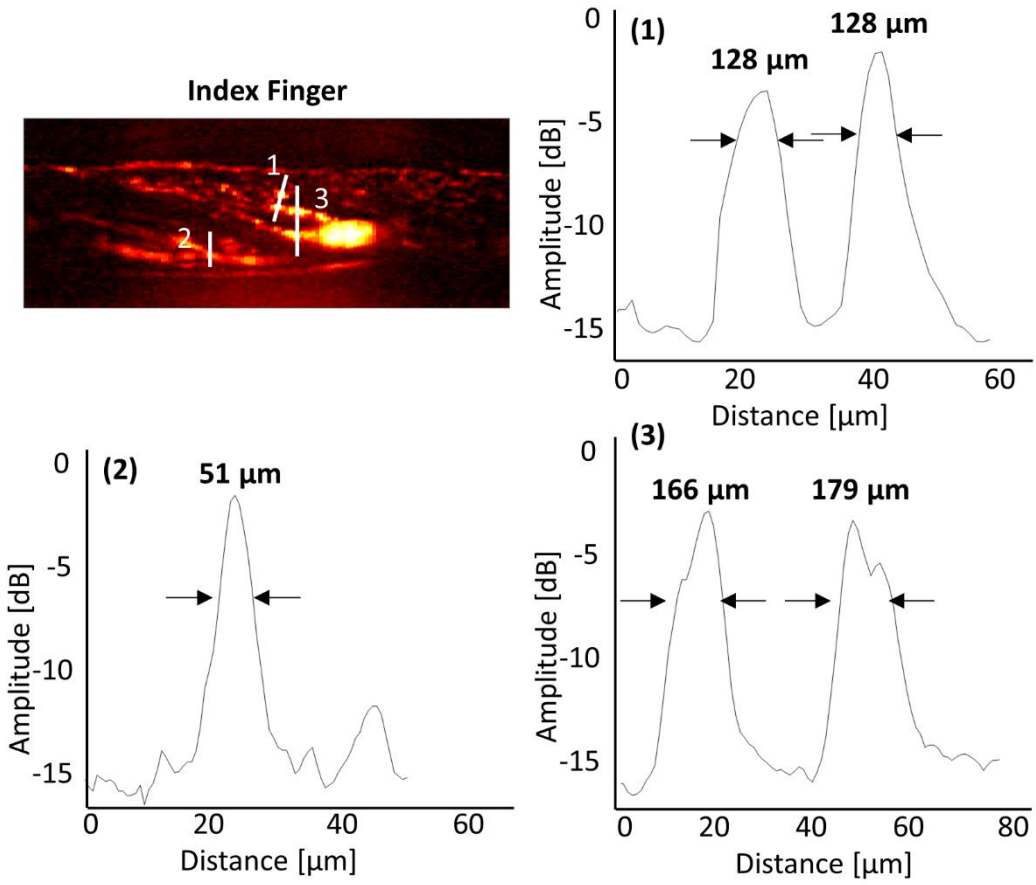

Fig. 4.5. Quantitative measurement of visualized superficial micro-vessels diameter.

Chapter 5

Region-based SVD Processing of Ultrafast Ultrasound

Singular value decomposition (SVD) has been widely used as a clutter filter in ultrafast ultrasound imaging of microvasculature. This filter performs clutter filtering on ultrafast ultrasound data based on spatio-temporal characteristics which makes this filter efficient in extraction of flow signal under wide range of flow velocities. This chapter presents an advanced approach of SVD clutter filtering of high-frequency (HFUS) ultrafast ultrasound to visualize a complete cutaneous vascular network comprised on small vessels and micro-vessels. In the progression of the cutaneous diseases such as skin melanoma and Raynaud's phenomenon, the development of diseased tissues affects the functionality of the micro-vessels in correspondence to the small vessels in vice versa. In order to diagnose the disease in its early stages, it is significant to observe the complete vascular network which provides sufficient information about the spread of the diseases and its adverse events. The proposed approach of SVD clutter filtering relied on the region-based SVD processing of HFUS ultrafast data acquired from the surface of the skin. In the proposed algorithm the regions for SVD processing were chosen based on the prior skin anatomical identification and vascular information obtained from B-mode morphological imaging. Each selected regions was processed individually with SVD to extract the desired flow signal of vasculatures from each layers of skin. The proposed processing approach has shown its merit in visualization of complete cutaneous vasculatures by truncating the epidermal clutter tissue signal efficiently and extracting the desired flow signal significantly from the respective regions of skin layers.

5.1. Basic Principle

Since the emergence of ultrafast acquisition technique of ultrasound imaging, it has brought a breakthrough in visualization of micro-vessels. The ultrafast technique insonify

the whole imaging area at multi-angle plane wave transmissions and acquired a synchronous backscattered signal at high frame rate of about 10 kHz. Acquisition of rich spatio-temporal data with ultrafast acquisition enhances the Doppler sensitivity in mapping of micro-circulation, also it facilitates to implement the advanced clutter filtering algorithms such eigen based clutter filters to distinguish the tissue, flow and noisy signals from the Doppler spectrum.

Previously, in ultrasound Doppler imaging clutter filtering in ultrasound was performed by temporal clutter filters such as FIR (finite impulse response), IIR (Infinite impulse response) and linear regression. Those clutter filters were designed on the assumption that flow signal and tissue signal in Doppler spectra have completely different characteristics. The tissue signal in Doppler spectrum is very slow with higher amplitude and blood flow signal is the fast motion of blood cells scatters with smaller amplitude. In that context, these signals possess a non-overlap Doppler spectra as shown in Fig. 5.1(a). Based on the temporal dynamics of the received Doppler signal, the ultrasonic data was filtered with FIR and IIR temporal filters to remove the tissue signal and extracts the flow signal. Hence in conventional filters, only the temporal characteristics of ultrasound data have been exploited in the clutter filtering. However, Demene et al[24] reported that in relation to temporal characteristic of signal in Doppler spectra, the spatial characteristic of tissue signal in Doppler spectra is also different from that of blood signal. For instance, tissue signals exhibit lower deformability compared to flow signals. Even small tissue movement can manifest as spatial shifts in the speckle pattern, whereas the movement of flow signal involves the rearrangement of blood cell scatterers, resulting in a distinct speckle pattern. In other words, ultrasound imaging indicates that tissue signals generally possess a higher level of spatial coherence compared to that of blood signals. Based on this advanced theory on clutter filtering, Ledoux et al[46] proposed the clutter rejection approach for ultrasound imaging based on singular value decomposition of the successive temporal samples. In their proposed method, both 1D spatial and temporal information were utilized via the diagonalization of the spatio-temporal (depth and time) correlation matrix. Several strategies has emerged from that advanced approach of clutter filtering[41]. However, in all the proposed strategies, the major limitation was the number of Doppler ensembles (Frames). The conventional focused beam transmission adopt a line-by-line

acquisition technique which results in acquisition of limited number of temporal and spatial samples. This impacts the performance of singular value decomposition based clutter filter processing because its full potential can be observed on the large number of dataset.

In comparison to the conventional line-by-line acquisition technique of ultrasound imaging in which the focused beam scans the imaging area in sequential manner, ultrafast acquisition technique impose an unfocused beam (plane wave) to acquire the signal at high frame rate by scanning the wide imaging area in single event of acquisition. From that acquisition technique the image quality and resolution of obtained images becomes poor due to the lack of focus in the transmission beam (plane wave). That limitation of poor resolution was overcome by implementing a multi-angle plane wave transmission scheme to insonify the medium multiple times with plane waves at different steering angles and reconstruct a coherently compounded image at reception, which consequentially enhances the image resolution and image quality. However, due to multi-angle plane waves in a sequence, there is a trade-off between the transmissions of plane waves and the frame rate in ultrafast acquisition technique of ultrasound imaging.

The advent of ultrafast acquisition technique of ultrasound imaging, the limitation of limited number of Doppler ensembles (Frames) was overcome for SVD based clutter filtering. Demene et al[24] reported that in the Doppler spectra of ultrasound data acquired with ultrafast acquisition, the tissue signal and blood flow signal possess overlapped signal characteristics as illustrated in Fig 5.1 (b-c). An approach of SVD based clutter filtering of ultrasound based on spatio-temporal characteristics of spectral signal distinguish the tissue signal and flow signal from the overlapped spectra due to its features of spatio-temporal filtering. They reported that the acquisition of ultrasonic signal with ultrafast technique was in synchronous manner at high frame rate which significantly enhances the performance of SVD based clutter filters in comparison to the conventional temporal based clutter filters.

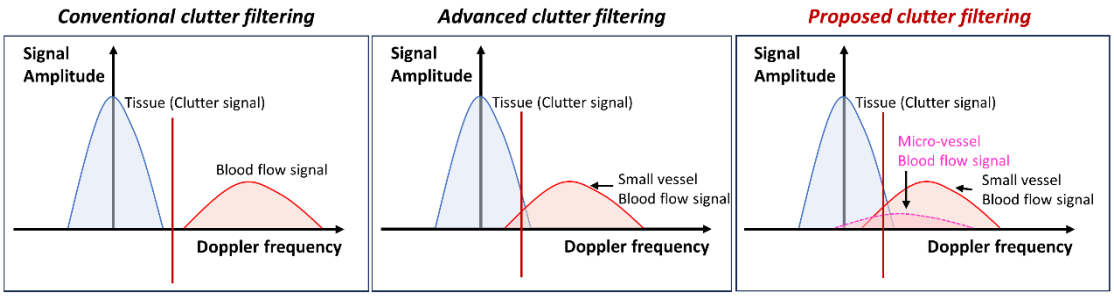

Fig.5.1. Doppler frequency spectrum of tissue clutter and blood flow signal

5.1.1. SVD Clutter Filtering

To perform the SVD clutter filtering on the acquired HFUS ultrafast ultrasound data $s(x,z,t)$, was first converted into two dimensional casorati matrix in the form of $s(x \cdot z,t)$ 2D space-time matrix. Later implementation of SVD on that 2D casorati matrix results in the decomposition of data into three different matrices as

$$S = U\Delta V^{*}$$

Where U represents the spatial singular vectors and V represents the temporal singular vectors and Δ is a non-square diagonal matrix of singular values. As show in Fig. 5.2 the clutter signal was removed by truncating the higher singular values via singular value thresholding results in the filtering of a matrix comprised on the blood flow signal and noisy signal. Later the filtered matrix at specified threshold values was rearranged into the form of original matrix and calculated the average intensity per pixel to create the Power Doppler image[21]. That specified or traditional approach of SVD clutter filtering of ultrafast ultrasound data performs well under the condition when the tissue signal, blood signal and noise signal in ultrasound dataset are uniform in the imaging field, which means that the characteristics of ultrasonic signal acquired from the imaging field retains the signals with uniform spatio-temporal characteristics. Its performance becomes sacrificed when the signals characteristics become non-uniform such as in the case of deep and denser imaging areas (kidney vascular imaging) where the system generated noise field increases also the vascular morphology appears to be as dense and perfused structures. The performance of SVD in traditional global manner becomes compromised

to extracts the flow signal from denser vascular networks, because the signal characteristics varied over the imaging field. To overcome such limitation of global SVD clutter filter, the block-wise approach of SVD was proposed. In that approach, before implementing the SVD, the acquired dataset of ultrasound was divided into multiple blocks of specified dimensions and overlapped ratio. Once the blocks were created, SVD was performed on each block individually to filter out the vascular blood flow signal locally at defined cut-off threshold values. By implementing the SVD in block-wise manner, it extracts the flow signal and remove the clutter signal and noises efficiently due to its feature of local filtering based on local data statistics. However, this approach has also certain limitations such as it is computationally expensive, because SVD was performed locally on each block of the imaging field as shown in Fig. 5.2, beside the filter parameters such as block size and overlap ratio need to be optimized for every acquire dataset.

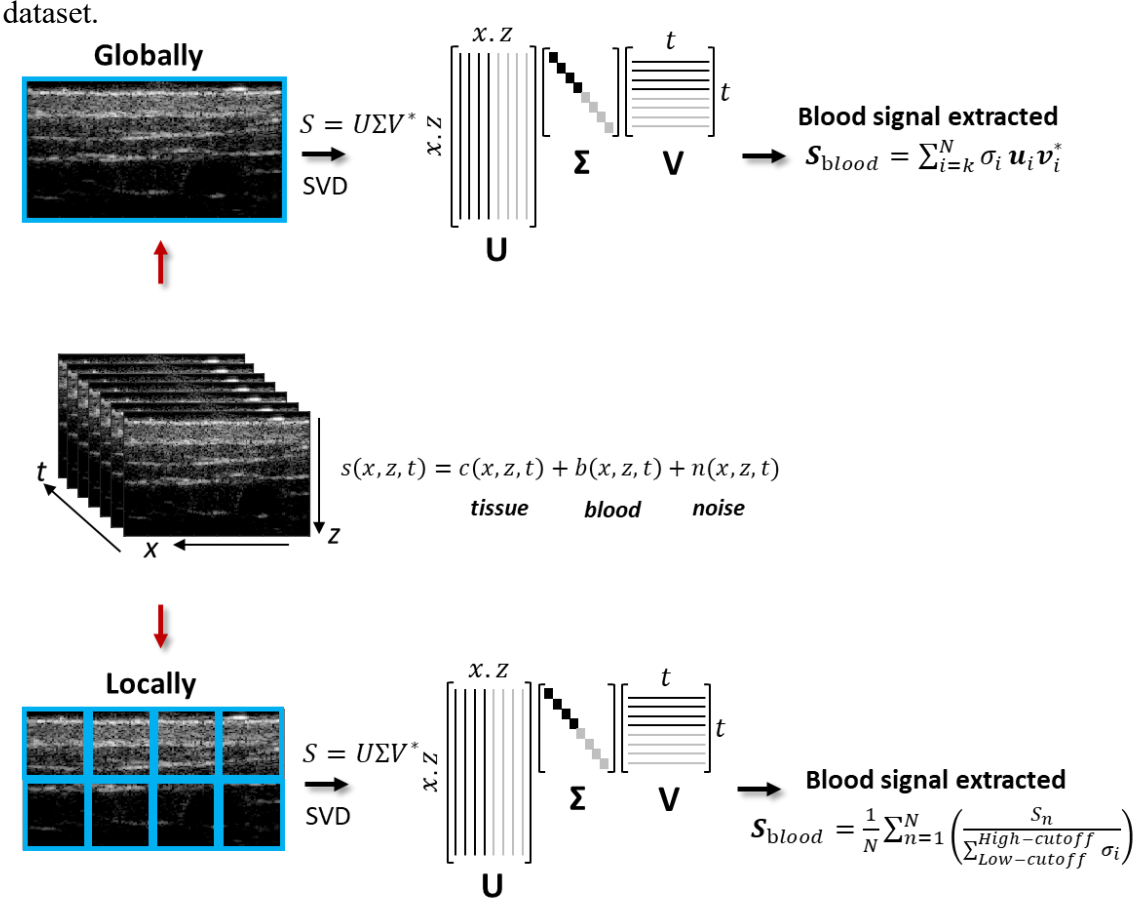

Fig.5.2. Illustration of SVD clutter filtering of ultrasound in global and block-wise processing

5.1.2. Motivation/Problem statement

The processing of ultrafast ultrasound Doppler data through Singular Value Decomposition (SVD) has revealed a significant distinction between the spatial and temporal properties of tissue and blood signals within the backscattered echoes. Notably, tissue signals exhibit a higher degree of spatial coherence as shown in Fig. 5.3(b) compared to blood signals. Leveraging this observation, SVD have been employed globally[24] across the entire imaging area, as well as locally in block-wise processing[30] to eliminate the tissue clutter signal and noises by performing singular value thresholding (SVT). In the context of small-scale vascular imaging, the global SVD approaches demonstrated effectiveness, particularly when the spatial and temporal characteristics of tissue, blood flow and noise components remained consistent throughout the entire imaging area. This was particularly evident in scenarios like functional mice brain imaging[25]. Conversely, block-wise SVD techniques have been introduced to enhance the sensitivity in visualizing deeper and densely packed small vessels, such as those found in the kidney and liver. In these areas, the structural complexity of blood vessels and the characteristics of background noise can vary spatially. However, it's important to note that this approach comes with increased computational demands and requires optimization of several parameters, such as the size and overlap ratio of the blocks, when compared to the global SVD approach. When it comes to cutaneous vascular imaging, employing the global SVD approach for tissue clutter filtering may not be the most suitable option. This is because both tissue and flow signal exhibit non-uniform spatial and temporal characteristics in different layers of skin at different depth position. For instance, there is a higher tissue intensity in the dermis layer and faster blood flow in the subcutaneous layer. Additionally, high intensity flow signal of arteries in subcutaneous layer overwhelm the image dynamic range and limits the visibility of micro-vessels in the dermis layer. Furthermore, the micro-vessels in the dermis layer are less densely distributed (sparse) in comparison to those within internal perfused organs (such as kidney and liver). This disparity in distribution complicates the process of determining optimal parameters for the block-wise SVD approach, as local data statistics vary significantly across different points of the skin. In this regard, If the filter is not implemented

appropriately, clutter may not be sufficiently attenuated, or parts of the blood signal may be concomitantly removed in the filtering process. Given these unique challenges, the objective of this study was to develop a new approach of tissue clutter filtering. This approach aimed to robustly extracts the blood flow signals from the intricate vascular network present in different layers of the skin.

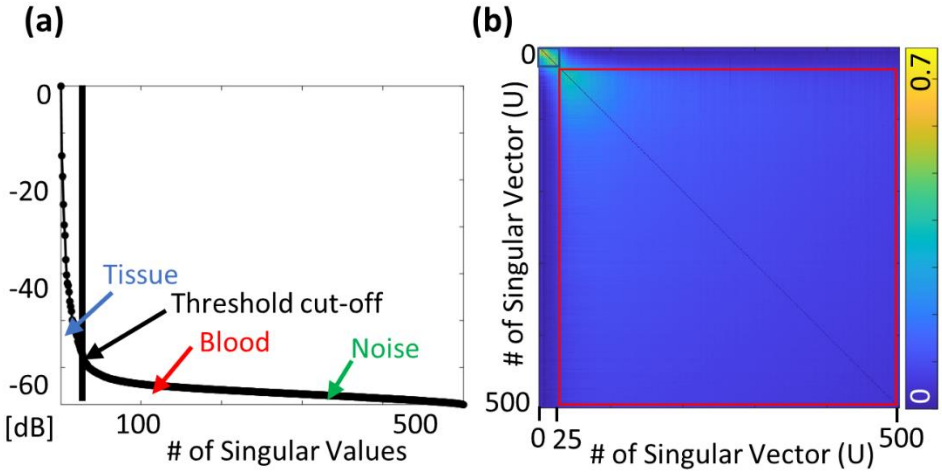

Fig. 5.3 (a). Selection of optimal threshold cut-off from singular value. (b). Covariance matrix of spatial vectors.

5.1.3. Proposed Approach

In this study we introduced a novel approach of SVD clutter filtering based on the region-based SVD processing (Fig. 5.4). The ultrafast data of acquired B-mode frames, presented as three-dimensional complex In-phase and Quadrature (IQ) data of s (x, z, t), where x, z, and t representing the lateral, depth, and temporal dimensions of the data respectively, was implicit to comprise on three distinct signal components: clutter signal $c(x, z, t)$, blood signal $b(x, z, t)$, and noise $n(x, z, t)$ as in Equation 1.

$$s(x,z,t) = c(x,z,t) + b(x,z,t) + n(x,z,t) \qquad (1)$$

In the traditional global SVD filtering approach, it was hypothesized that the spatio-temporal characteristics of each component in Eq. (1) remained consistent across the entire imaging area. However, in the cutaneous imaging, these characteristics can vary between the different layers of skin. For instance, the dermis layer is composed of collagen and elastic fibers, making it relatively more hyperechoic compared to the deeper subcutaneous layer. Additionally, the speed and pulsatility of peripheral blood flow within the dermis layer are relatively lower than those in the subcutaneous layer. To effectively extracts the blood vessel signals within their respective layers, we hypothesized that the blood signal b can be divided into two regions at a specific depth of z_{th},

$$b = \begin{cases} b_{\text{dermis}}(x,z,t), & z \in [0, z_{th}] \\ b_{\text{subcutaneous}}(x,z,t), & z \in (z_{th}, z_{max}] \end{cases} \qquad (2)$$

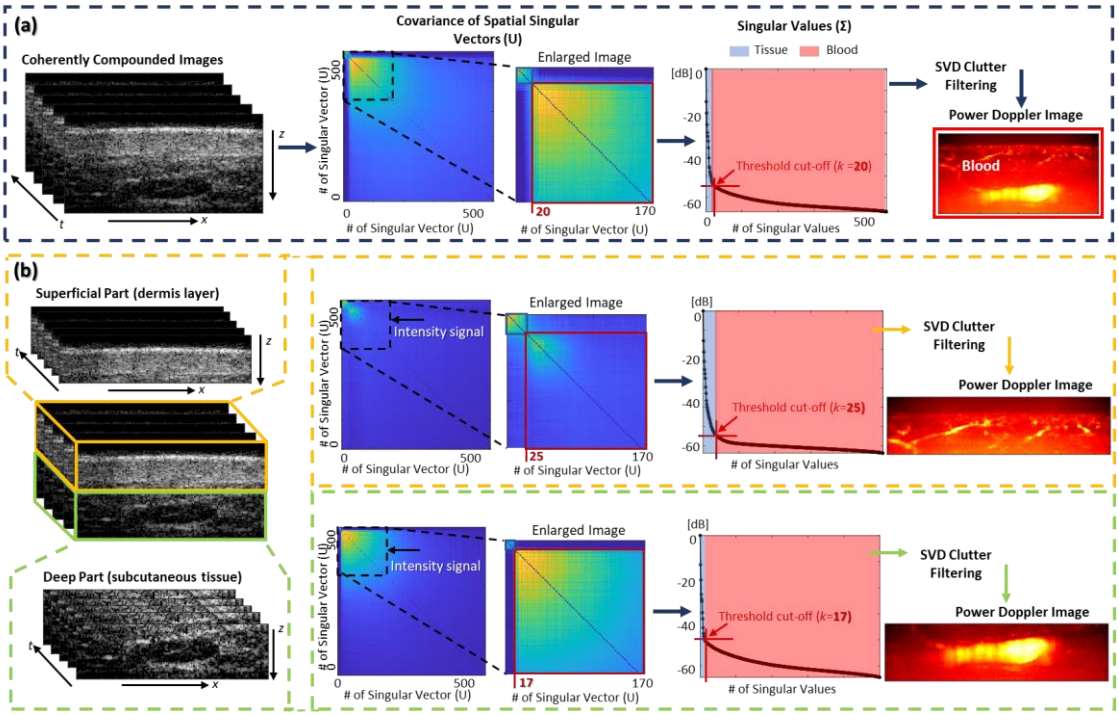

Fig. 5.4. Illustration of selecting optimal threshold value. (a) global SVD approach. (b). Proposed region-based SVD processing of ultrafast ultrasound of skin dataset. © *2022, Ultrasonics, Elsevier*

As a result, the acquired B-mode data was initially divided into two distinct horizontal rectangular regions: the dermis (upper region) and the sub-cutaneous (lower) regions. In this study, the horizontal boundary between these regions was manually set based on the B-mode intensity map, which provides a demarcation of the dermis-subcutaneous tissue boundary. Subsequently, we applied SVD clutter filtering independently to each of these regions. As reported in several studies/as mentioned earlier, SVD can decompose spatio-temporal signal $\boldsymbol{S}$ into three matrices $\boldsymbol{U}$, $\boldsymbol{V}$, and $\boldsymbol{\Sigma}$. This can be seen in Equation 3, where $\boldsymbol{U}$ and $\boldsymbol{V}$ are spatial and temporal singular vectors with dimensions ($n_x \,.\, n_z \,,\ n_x \,.\, n_z$) and ($n_t \,.\, n_t$) respectively, and $\boldsymbol{\Sigma}$ is a diagonal matrix with size ($n_x \,.\, n_z \,, n_t$) that involves singular values.

$$\boldsymbol{S} = \boldsymbol{U}\boldsymbol{\Sigma}\boldsymbol{V}^{*} \qquad (3)$$

Here, $\boldsymbol{S}$ is the 2D Casorati matrix form of $s(x, z, t)$ in one of the divided regions and * is the conjugate transpose operator. After determining the appropriate cut-off singular value k for suppressing the tissue clutter signal, the process of extracting the blood signal, accompanied by low-intensity background noise $\boldsymbol{S}_{\mathrm{bn}}$ proceeded as follow,

$$\boldsymbol{S}_{\mathrm{bn}} = \sum_{i=k}^{N} \sigma_i \, \boldsymbol{u}_i \boldsymbol{v}_i^{*} \qquad (4)$$

where N is the ensemble size and σ_i, $\boldsymbol{u}_i$, $\boldsymbol{v}_i$ are the i^{th} singular value, spatial and temporal singular vectors respectively. The boundary between two distinct subspace squares observed in the covariance of spatial singular vectors $\boldsymbol{U}$[47] was chosen in this work to determine the best cut-off singular value k from respective regions as shown in Fig.5.4. The blood signal from each regions was then captured by generating power Doppler image PW_{bn}, as follows,

$$PW_{\mathrm{bn}}(x, z) = \ 10 \log_{10} \int | \, s_{\mathrm{bn}}(x, z, t)|^2 \ dt \qquad (5)$$

where s_{bn} is a three-dimensional matrix converted from the 2D Casorati matrix $\boldsymbol{S}_{\mathrm{bn}}$. Finally, a single image was created by combining two power Doppler vessel images from respective regions. To merge the power Doppler images obtained from each respective

region, at first we determine the difference in between two pixels of the merged image at the boundary of the regions, later we measured the mean of the obtained difference value, and then add the mean difference value to the power Doppler image of the second region and obtained the merged power Doppler image as illustrated in Fig 5.5.

$$PW = \text{First Region} + \text{Second Region}$$

$$\text{Difference} = PW(181) - PW(182)$$

$$\text{mean (Difference)}$$

$$\text{Second Region\_2} = \text{mean (Difference)} + \text{Second Region}$$

$$PW = \text{First Region} + \text{Second Region\_2}$$

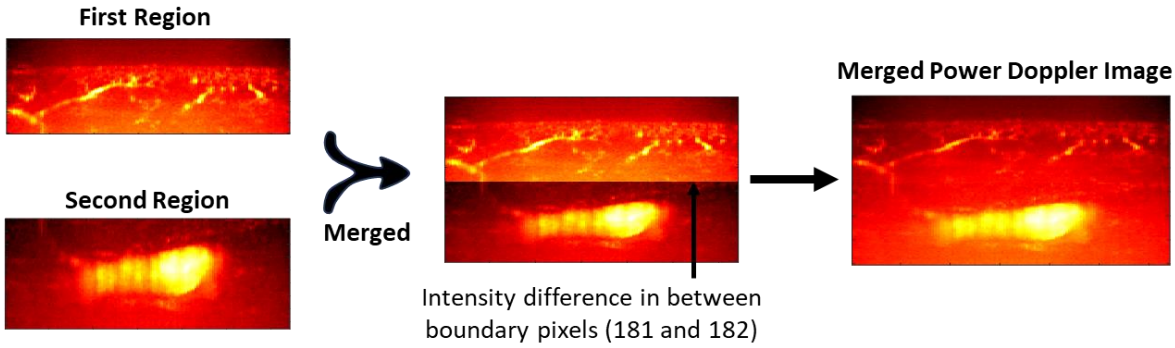

Fig. 5.5. The illustration of the mean difference value measurement and utilization of the determined value in merging two power Doppler images from two different regions into one merged power Doppler image.

5.2. Imaging Framework

A novel imaging framework shown in Fig. 5.6 was developed to visualize the intricate cutaneous vascular network. Initially, we acquired a set of five hundred B-mode image

frames of the skin up to depth of 4 mm, utilizing the coherently compounded ultrafast ultrasound imaging. The process of generating a single B-mode frame involved emitting plane-wave pulses (characterized by 3 cycles and a central frequency of 31.5 MHz) from ten distinct transmission angles (ranging from -5 to +5 degrees). These pulses were transmitted at a pulse repetition interval of 200 μs (resulting in pulse repetition frequency of 5 kHz). The channel-domain radiofrequency (RF) signals received from each transmission angle were then beamformed and spatially compounded to form one B-mode image. This process led to a post-compounding frame rate of 500 Hz. Given than we collected 500 frames for each experiment, the total acquisition time amounted to 1 second.

As a preliminary step, the B-mode images underwent horizontal division into two regions. Those regions were chosen based on the skin anatomical features from B-mode images. The upper region corresponded to the dermis layer, contained peripheral micro-vessels, while the lower regions represented the subcutaneous layer contained smaller vessels.

In the subsequent phase, SVD filtering was applied separately to each region, employing the fine hundred B-mode frames. This step aimed to extract to blood flow signals while considering the sensitivity of required for detecting micro-circulation within vessels (with flow speeds ranging from approximately 1 to 20 mm/s), while concurrently eliminating motion artifacts. The signals extracted from the respective regions were subsequently integrated into a single vascular image. Finally, to enhance the vessel visualization, we employed the top-hat transform morphological filter to suppress the remaining system generated background noise within the SVD processed power Doppler image. Further elaboration on each of these steps is provided in the subsequent sub-sections.

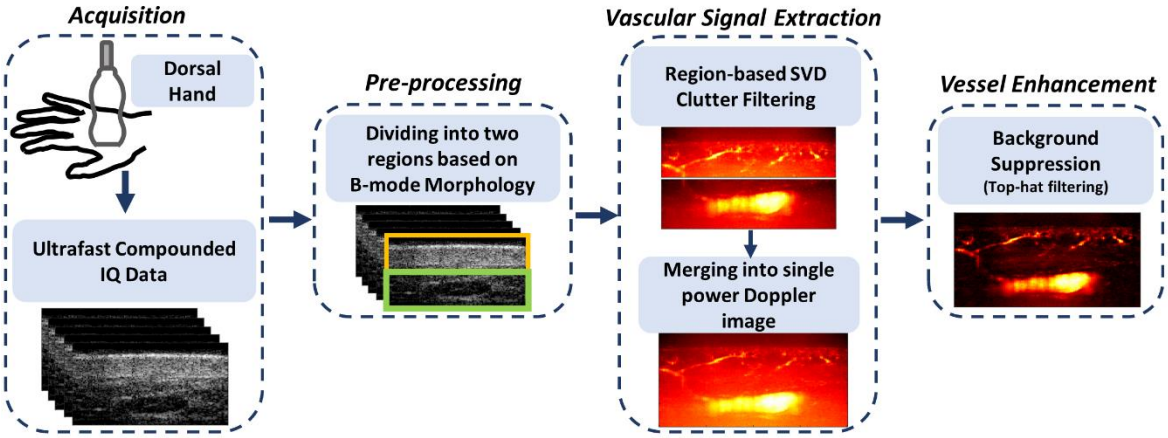

Fig. 5.6. Flow chart of imaging framework for visualization of complete cutaneous vascular network. © *2022, Ultrasonics, Elsevier*

5.3. Experimental Setup

The assess the effectiveness of proposed imaging framework, which comprises region-based SVD filtering followed by top-hat transform filtering. We conducted an imaging experiment to visualize the cutaneous vasculatures from three different position at the dorsum of the hand. As depicted in Fig. 5.7, the experimental setup consisted of an ultrasound system (Vantage 256 high-frequency configuration, Verasonics Inc., Kirkland, WA, USA) and a high-frequency CMUT (capacitive micromachined ultrasonic transducer) linear array transducer (L38-22v, KOLO Medical, San Jose, CA, USA) with center frequency of 31.25 MHz. The transducer was securely positioned using a holder and attached to the object under examination. To ensure the alignment between the imaging field and the probe's elevational focal depth (approximately 8 mm), a small hydrogel pad (6 mm thick, HydroAid, KIKGEL, Poland) was placed between the probe and the imaging object. The imaging sequence was programmed into the ultrasound system. For transmitting pulses at a center frequency of 31.25 MHz and receiving the echo signals, we utilized 128 transducer elements with an element pitch of 69 μm. It's worth noting that, to enable the 4-points/wavelength sampling method, the ultrasound system's maximum sampling rate (62.5 MHz) proved inadequate. Consequently, we

adopted a specialized sampling approach known as the bandwidth sampling method[44,52]. With this technique, echo data was sampled at a rate of 41.67 MHz, allowing acquisition of signals within a broader bandwidth (approximately 20 to 40 MHz) that exceeded the probe's native bandwidth. The acquired data was subsequently transferred to a personal computer equipped with MATLAB software (R2020b, MathWorks, Natick, MA, USA) for further signal and image processing. Data acquisition took place at the first dorsal interosseus muscle (located at the base of the thumb) to capture images of the radial artery and micro-vessels in the dorsal hand. We selected three imaging planes encompassing longitudinal sections (Trials 1 and 3) and a short-axis cross-section (Trial 2) of the radial artery to visualize the intricate cutaneous vascular network.

In addition to a qualitative evaluation of the proposed method by observing the subcutaneous vasculatures in generated images, as a quantitative index, the contrast-to-noise ratio (CNR) from all obtained images were calculated as shown in equation 6. This was to rectify the image quality and compare the performance with the conventional global SVD filtering approach.

$$CNR = \frac{\mu_{blood} - \mu_{background}}{\sigma_{noise}} \qquad (6)$$

where, μ_{blood} is the mean value (dB) of the blood vessel signal, $\mu_{background}$ is the mean value (dB) of the background clutter signal, and σ_{noise} is the standard deviation of the background noise signal.

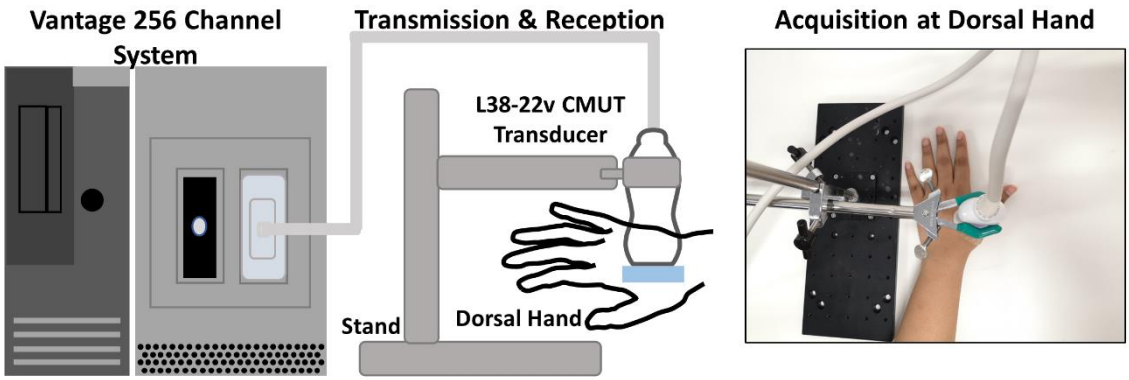

Fig. 5.7. Experimental Setup. © *2022, Ultrasonics, Elsevier*

5.4. Results

The region-based SVD clutter filtering of HFUS ultrafast data has demonstrated its effectiveness in extracting blood flow signals from micro and small vessels situated within the skin's dermis and subcutaneous layers, respectively. Fig. 5.8(a) illustrate the scanning position on the dorsal hand for HFUS ultrafast imaging and Fig. 5.8(b) provides an acquired B-mode images from the dorsum of the hand. Those images provides the skin's anatomical features, which serves as the basis for dividing the data into two distinct regions: the upper echogenic region includes the epidermis and dermis layers and the deeper hypoechoic region representing the subcutaneous tissue.

The B-mode frames of acquired HFUS ultrafast dataset were processed with the global approach of SVD and the proposed region-based approach of SVD. The obtained power Doppler images from respective SVD approaches were generated as shown in Fig. 5.8. It was observed that the proposed approach (Fig. 5.8(d)) of region-based processing eliminated the tissue clutter signals and visualized the microvasculature structures within the dermis layer efficiently as compared to the global SVD approach (Fig. 5.8(c)). In contrast, the appearance of small vessels within the subcutaneous layer remained consistent in the power Doppler images obtained with both SVD approaches. In addition, the visibility of the vasculatures was further enhanced with the application of top-hat transform filtering as shown in Fig. 5.8(e) and (f). Top-hat transform filter effectively suppressed the residual system generated background noise components that persisted in the power Doppler images after employing the global SVD approach as well as the proposed region-based SVD approach. In the case of the global SVD + top-hat filtering approach, it was observed that tissue clutter signal persisted in the epidermis and the dermis layers, obscuring the visibility of the dermal micro-vessels (indicated by arrows in Fig. 5.8(e)). Conversely, the region-based SVD + top-hat filtering approach has demonstrated that the proposed method successfully mitigated both tissue clutter signal and background noise, achieving robust and clear visualization of the comprehensive skin vascular networks.

Furthermore, Fig. 5.8(g) and (h) presents the intensity profiles derived from two distinct vertical lines drawn in Fig. 5.8(e) and 5.8(f), respectively. These intensity profiles

distinctly reveal three distinct signal peaks, symbolizing the superficial epidermal clutter signal, the dermal micro-vessel signal, and the subcutaneous small vessel signal. An important observation has been drawn from these profiles is the effective suppression of the epidermal tissue signal, as depicted by the pink line, when utilizing the proposed method of region-based SVD clutter filter in contrast to the global SVD approach, as also indicated by the pink arrows in Fig. 5.8(f). Additionally, the peak of the micro-vessel signal extracted through the region-based SVD method (pink lines) was observed to have a slightly elevated peak compared to the global SVD approach (blue line), while the peaks representing small vessels remained consistent between both SVD approaches.

Furthermore, the diameter of the visualized micro-vessels was quantified by measuring the Full Width at Half Maximum (FWHM) from the intensity profiles at -6 dB. These measurements revealed that the detected diameters of the two superficial micro-vessels were 76 and 128 μm, respectively. These observations were made during Trial 1 and were consistently confirmed in other trials presented in Fig. 5.9 and Fig. 5.10. In various positions on the dorsal hand, the micro-vessels within the dermis layer were better visualized when employing the proposed region-based SVD and top-hat filtering approach. It was evident from these trials that the proposed method outperformed in terms of micro-vessel visualization and clutter signal removal in cutaneous vasculature imaging. Collectively, these experimental trials underscore the resolvability and robustness of the region-based SVD technique in extracting the slow-flow signal of dermis layer micro-vessels while concurrently eliminating the epidermal clutter signal, leading to a substantial enhancement in imaging contrast.

In order to assess the image quality, Contrast-to-Noise Ratio (CNR) values were computed around a micro-vessels visible in each power Doppler image, as depicted in Fig. 5.11. Initially, a square region measuring 17 pixels in width and 40 pixels in height was selected. Within this region, the vascular area was manually delineated and designated as the signal region (illustrated as the blue dotted area in Fig. 5.11). The remaining pixels within the region were considered part of the background clutter region (depicted as the black solid box in Fig. 5.11). Subsequently, a noise (avascular) region of the same dimensions and at the same depth was selected (as shown in the green solid box in Fig. 5.11). In all three trials, CNR values were determined in a sequential order, starting

with Global-SVD filtering, followed by Region-based SVD filtering, then Global-SVD + top-hat filtering, and finally Region-based SVD + top-hat filtering. For example, in Trial 1, the image processed using the region-based SVD exhibited a contrast of 4.1 dB compared to the 3.4 dB achieved with global SVD processing. Additionally, the top-hat transform effectively suppressed background noise, leading to an improved overall image quality. Consequently, the image processed with region-based SVD + top-hat filtering achieved a contrast of 5.2 dB, surpassing the 4.0 dB contrast obtained with global SVD + top-hat filtering. In addition, image contrast was evaluated in other experimental trials, as presented in Fig. 5.11, to assess the performance and consistency of the proposed method. It was observed that, on average, the overall image contrast increased by 0.7 dB when employing the region-based SVD approach instead of global SVD filtering. Furthermore, the addition of top-hat filtering to the region-based SVD filtering further enhanced the contrast by 1.0 dB.

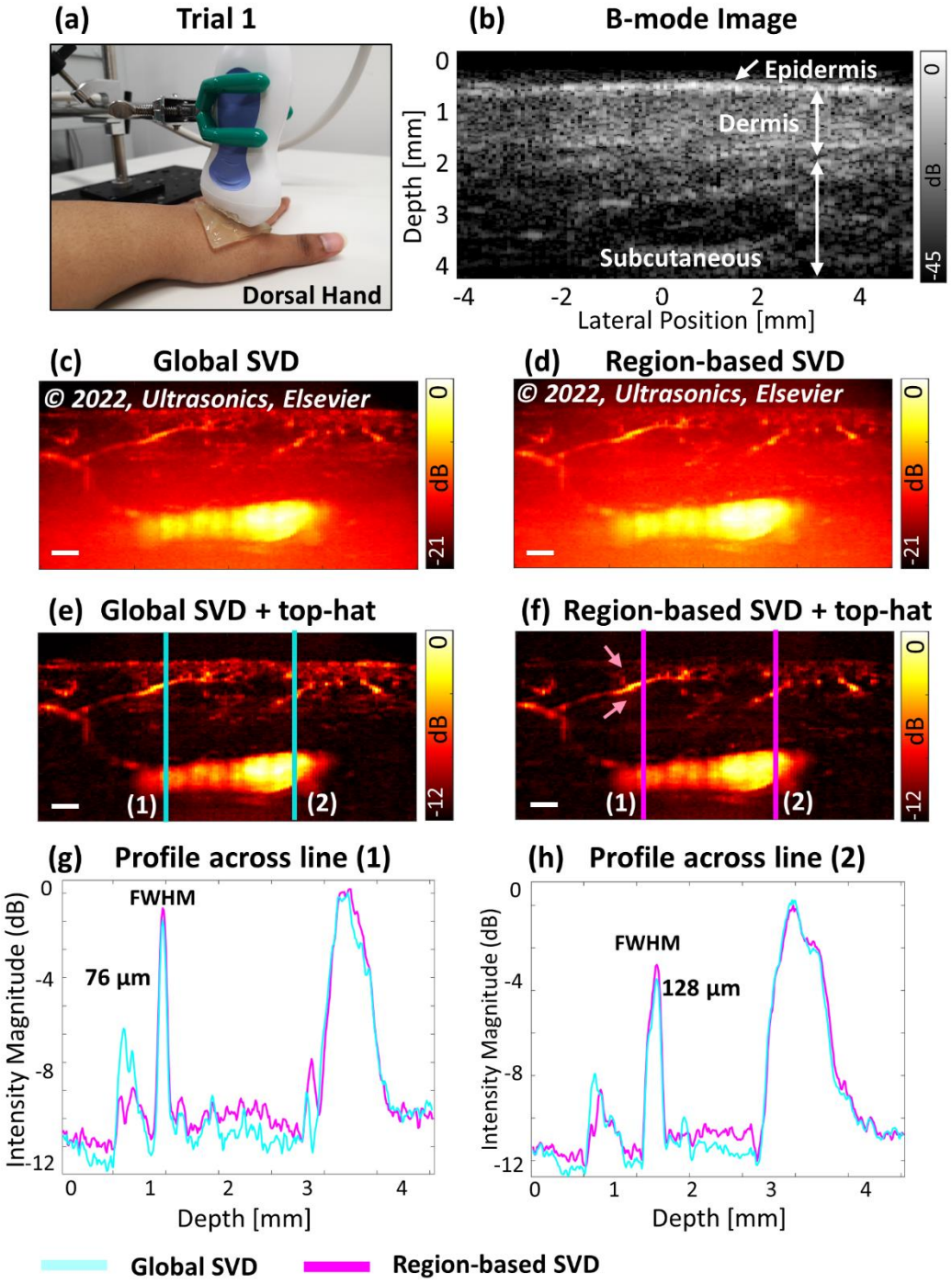

Fig. 5.8. Obtained images from the dorsum of the hand (Trial 1). (a). Illustration of imaging position. (b). Acquired B-mode image. (c-e). Power Doppler images processed with global SVD and top-hat filtering. (d-f) Processed power Doppler images with proposed region-based SVD and top-hat filtering. (g) and (h) intensity profiles from respective line 1 and 2. Scale bar represents 1 mm. *© 2022, Ultrasonics, Elsevier*

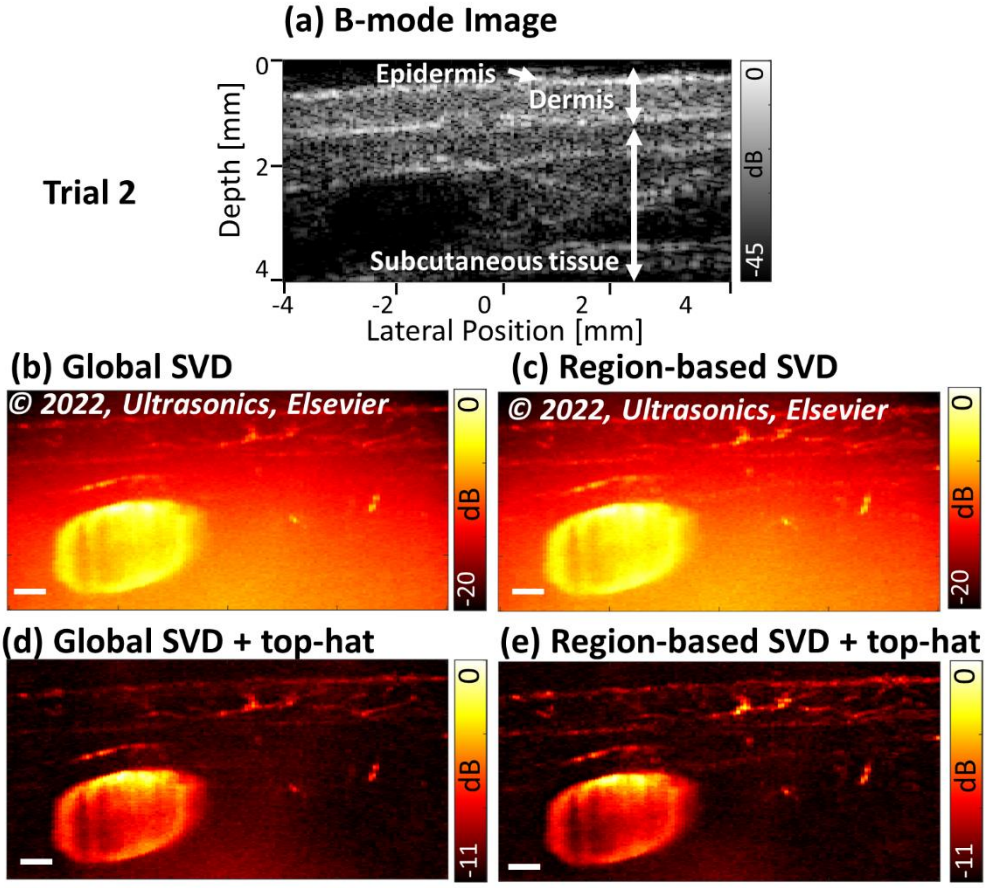

Fig. 5.9. Obtained images from the dorsum of the hand (Trial 2). (a). Illustration of imaging position. (b). Acquired B-mode image. (c-e). Power Doppler images processed with global SVD and top-hat filtering. (d-f) Processed power Doppler images with proposed region-based SVD and top-hat filtering. (g) and (h) intensity profiles from respective line 1 and 2. Scale bar represents 1 mm. © *2022, Ultrasonics, Elsevier*

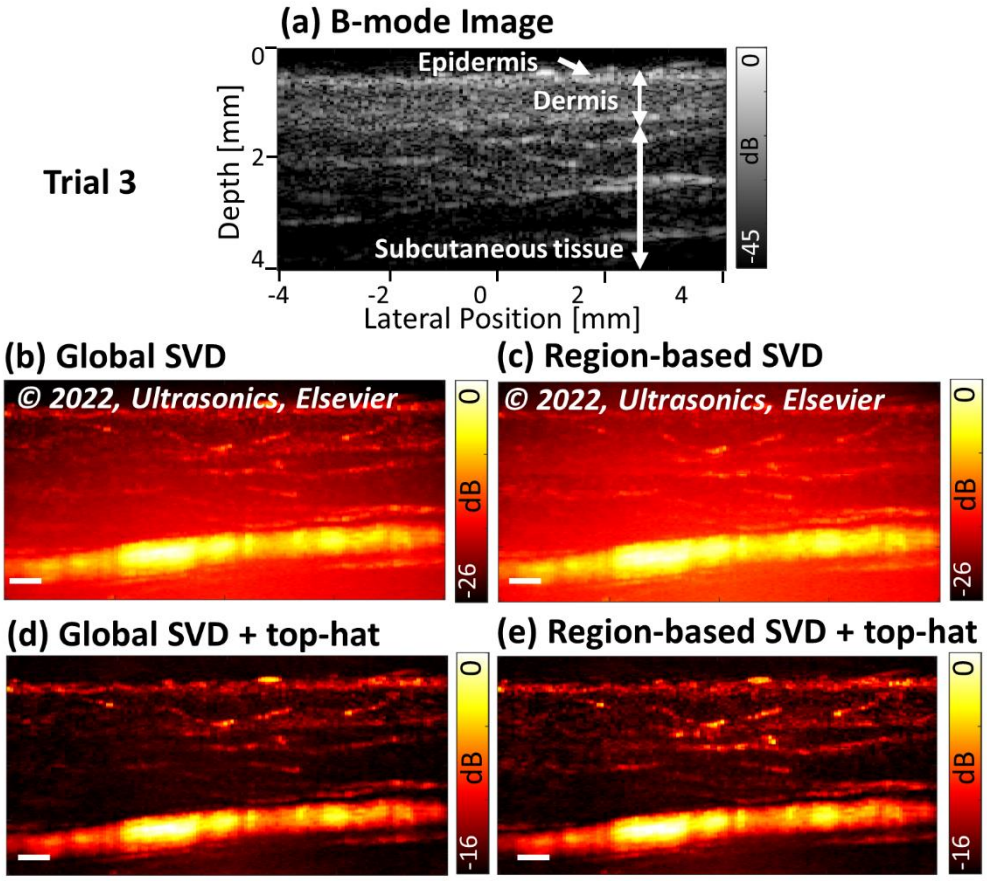

Fig. 5.10. Obtained images from the dorsum of the hand (Trial 3). (a). Illustration of imaging position. (b). Acquired B-mode image. (c-e). Power Doppler images processed with global SVD and top-hat filtering. (d-f) Processed power Doppler images with proposed region-based SVD and top-hat filtering. (g) and (h) intensity profiles from respective line 1 and 2. Scale bar represents 1 mm. © *2022, Ultrasonics, Elsevier*

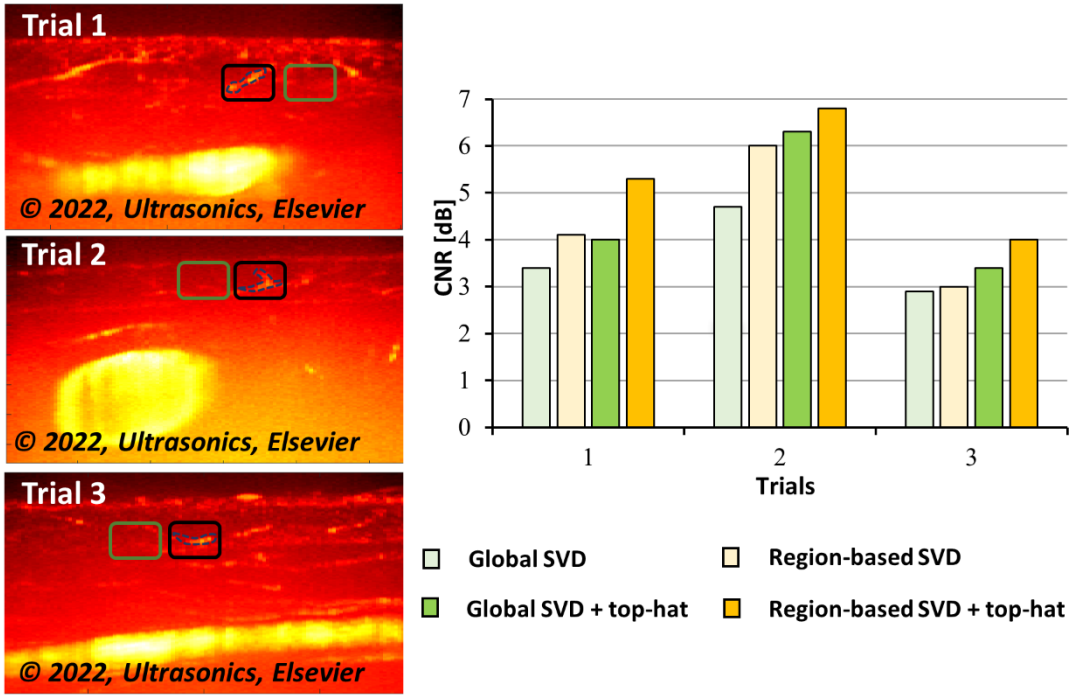

Fig. 5.11. Quantitative analysis on the metric of CNR among global SVD and region-based SVD approach. Black and green solid line boxes represent the ROI for background signal and noises respectively, while the blue dashed lines indicate the blood signal in micro-vessels in all respective images.

5.5. Discussion

In this study, we devised a novel region-based processing algorithm of SVD clutter filtering for visualizing cutaneous vascular networks using ultrafast HFUS imaging. The *in-vivo* skin experiments showed that, in comparison with the global SVD approach, the proposed approach successfully increased the contrast of the micro-vessels in the dermis layer. It effectively suppressed the tissue clutter in the dermis layer and enabled robust and clear visualization of the comprehensive skin vascular network from micro-vessels (dermis layer) to small vessels (subcutaneous tissue).

To extract such flow signals from vasculatures with different dimensions and flow rate and at different depth positions, this study utilized anatomical layer information of the

skin obtained in B-mode imaging and divided the imaging field for blood vessel visualization into two regions, based upon the biological knowledge such as the range of diameter and flow speed of the blood flow is different between the dermis layer and the subcutaneous tissue, and the epidermis layer does not contain any blood flow (avascular). Hence, ultrafast HFUS echo data from each region should have its own spatio-temporal characteristics and based on the respective data statistics, the region-wise SVD could estimate the optimal cut-off singular values to suppress the tissue clutter components for each region significantly. In contrast, the global SVD approach assumed the uniform spatio-temporal characteristics over the imaging field, and it was not a desirable assumption for the skin vascular imaging. The power Doppler images in Figs. 5.8 (c) and 5.9 (b) showed that the global SVD approach effectively eliminated the clutter signal in the subcutaneous tissue, but the clutter components remained at the epidermis and dermis layers hampered the visibility of the micro vessels. This might be because the small vessels in the subcutaneous tissue had much higher flow speed and larger diameter than the micro vessels in the dermis layer, and the slow-flow signals from the micro-vessels tended to reside at different spatio-temporal singular vectors which were overlapped by tissue clutter signals. To test the optimality of the cut-off singular value selected for proposed region-based SVD clutter filtering and explained in Section 5.1.3. The optimal cut-off singular value for the given dataset (regardless of the SVD approach either global SVD or the proposed region-based SVD) was chosen based on the boundary of the two subdivisions as illustrated in Fig. 5.12. We evaluated the performance of the global SVD with different cut-off singular values as shown in Fig. 5.12 and confirmed that the cut-off value of (k = 20) estimated by the covariance matrix of the spatial singular vectors outperformed the other singular values from an aspect of the imaging quality (CNR) as shown in Fig. 5.12.

The CNR of the global SVD filtering with the optimal cut-off value was found to be 3.4 dB, while it was still smaller than 4.1 dB obtained after the region-based SVD filtering. This might be because of the fact that, in global SVD, some features of the signal from micro-vessels were contained in the singular vectors corresponded to the tissue region due to the flow speed in the micro-vessels that is very slow compared to that in the smaller vessels in the deeper region. The proposed region-based SVD filtering aided to separate

those signals from micro-vessels and tissue clutter more robustly and precisely.

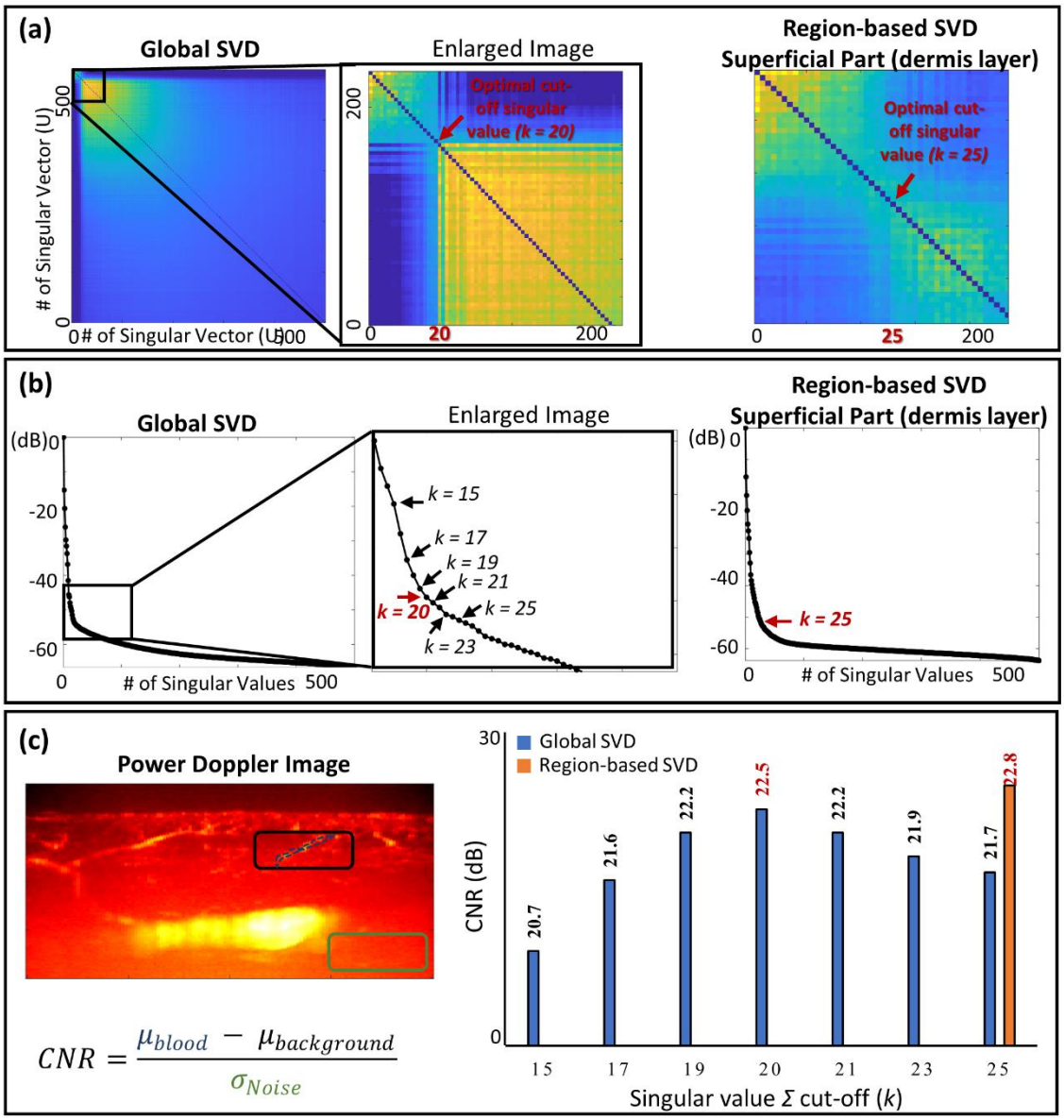

Fig. 5.12. The evaluation of image quality (CNR) at different singular value cut-off. (a). Covariance matrix obtained from spatial singular vectors (**U**). (b). Singular values (Σ) magnitude graph. (c). Obtained power Doppler image, and respective CNR measurements under different cut-off values in global SVD processing, and single optimal cut-off value measurement with proposed region based SVD processing.

From that validation, it was confirmed that the selected cut-off singular value ($k = 20$) was optimal to give the best CNR with the global SVD approach, while the region-based SVD filtering outperformed the global SVD filtering with any cut-off values since, in the region-based approach, the SVD filtering for the upper dermis region was not influenced by any tissue and flow characteristics in the lower subcutaneous region. After the SVD filtering, the system-generated background noise components remained in the image, impede the micro-vessel visibility as shown in Figs. 5.8(c, d) and 5.9b, c), because this study only selected a single cut-off singular value for SVD filtering that suppressed the tissue clutter components and preserved the flow and noise components. These background noises could be effectively eliminated using top-hat transform filtering, which was capable of selectively suppressing the background noises based on the morphological characteristics and further enhancing the visualization of the microvasculature as shown in Figs. 5.8 (e, f) and 5.9 (d, e). As a result of better suppression of the tissue clutter and the background noise components, our experiments found that the combination of region-based SVD and top-hat filtering was the desirable framework for visualizing the comprehensive cutaneous microvascular networks, and it was also observed in the quantitative evaluation using CNR metric (Fig. 5.11).

In comparison to other adaptive SVD filtering approaches, e.g., block-wise SVD filtering, we conducted a comparison analysis based on image quality and processing time as shown in Fig. 5.12. In block-wise SVD filtering, the imaging field was split into multiple blocks and the flow signals were extracted locally by performing SVD filtering for each block based on local data statistics. The block-wise SVD has shown merit in visualization of deep and dense vasculatures where performance of global SVD was compromised due to alteration in structural complexity and presence of the depth-dependent background noise, while in order to achieve desirable performance, implementation of block-wise SVD required optimizations of processing parameters such as the size and the overlap ratio of the blocks depending on the stochastic properties of the imaging area. The performance of the block-wise SVD filtering in the cutaneous micro-vessel's visualization has been shown in Fig. 5.12. Due to the sparsity in the dermis micro-vessels, most of the blocks remain signal less while processing with the block-wise

SVD clutter filtering. In terms of CNR measurement, the observations shown that the image quality of the power Doppler image processed with block-wise approach is slightly higher than the global SVD approach, while the processing time is also quite higher than the global SVD. On the other hand, the image contrast of the power Doppler image processed with proposed region-based SVD clutter filter has higher CNR value of 4.1 dB than that of 3.5 dB of block-wise approach and 3.5 dB of global SVD approach. Besides, the region-based SVD processing consume less time of 4.2 sec in comparison to 6.9 sec of block-wise SVD approach. In that comparison analysis we observed that the skin vascular networks are superficial and sparser, and the local data statistics much vary at every imaging location, which would make it difficult to optimize the necessary parameters for each image. On the other hand, the region-based SVD approach can readily select the regions as it relies on the anatomic information observed in B-mode images and would facilitate simple and robust micro-vascular imaging.

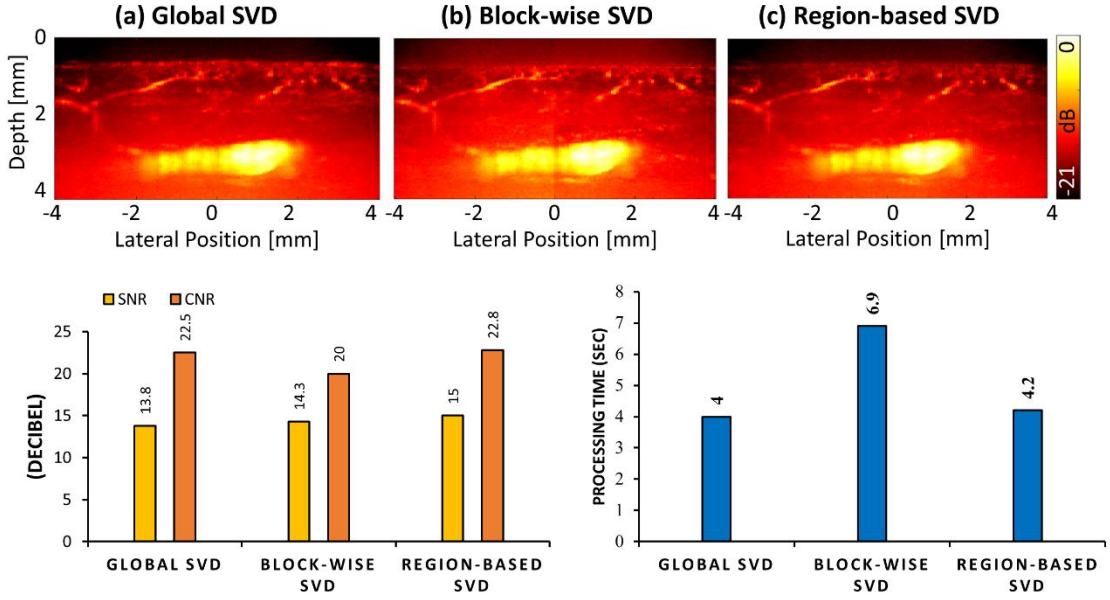

Fig 5.13. Power Doppler images of cutaneous vasculatures, processed with the global SVD, the block-wise SVD and the proposed region-based SVD. (a). Quantitative comparison in CNR measurements among different processing methods, (b). Processing time (computational cost) versus the different SVD processing methods.

As shown in Fig 5.8 (h), the detected diameter of the micro-vessels was approximately 76 μm that was in a range of the peripheral microvascular diameter reported literature, i.e., 10-200 μm[53,54]. In order to visualize further minute vessels, both hardware and software innovations such as ultra-high frequency ultrasound systems (> 40 MHz)[27] and super-resolution imaging techniques[55] may be used. In addition, the current workflow executed the processing manually for cut-off selection and the extraction of regions from the B-mode, which could be improved through automatic integration, for further enhancing the sensitivity and visualization of micro-vessels. Meanwhile, the present approach was limited to 2D visualization which will be expanded to 3D volumetric imaging to better observe the complex vascular networks of the skin which will be elaborated in the subsequent chapters. Also, the presented *in-vivo* results from a healthy human subject provided an insight for conducting clinical trials to further validate the proposed technique to visualize vasculatures in the progression of cutaneous disorders.

Chapter 6
Three-dimensional Volumetric Imaging of Superficial Micro-vessels

Advancements in ultrafast acquisition techniques in conjunction of spatio-temporal clutter filters based on singular value decomposition (SVD) has significantly enhanced the sensitivity of Doppler ultrasound in visualization of micro-vessels. This combined approach provides new diagnostic markers for numerous preclinical and clinical applications [20-30]. The advancements realized in two dimensional ultrasound imaging can also be extended to three dimensional volumetric ultrasound imaging, enabling a comprehensive evaluation of micro-vasculatures in disease diagnosis and its progression. Typically, power Doppler imaging of superficial (skin) vasculatures, makes use of a high frequency 1D-array transducer to image a specific cross-sectional 2D slice image of the skin. That 2D image of the skin or single slice image of skin is unable to provide the complete comprehensive visualization of blood vessels which resides outside the out-of-plane insonified region and is therefore insufficient when observing the complex vascular structures such as cutaneous vascular network (small vessels and micro-vessels).

Some studies [82,83] have been reported to use the 2D-matrix array transducer for 3D Doppler ultrasound imaging, which are able to generate a 3D volumetric image at single event of transmission. However, these systems experiences lower signal sensitivity, high computational complexity and high cost (both for transducer and the hardware required to use it) when compared to traditional 1D linear array transducers. Several other methods [73-77] have been reported for 3D visualization of vascular structures or anatomical morphological imaging using a 1D linear array transducer. In those reported approaches, mainly the motorized stages have been used to translate the transducer across the region of interest to perform 3D imaging. One of such method is iterative mechanical scanning in which the ultrasonics signal was acquired in sequential manner in multi-step acquisition process. Stationary acquisition is repeated for every location of the 3D imaging field resulting in a long acquisitions time and is mainly applicable to stationary

objects such as small animal imaging. The applicability of this iterative approach has been reported previously for small animal's brain functional ultrasound imaging[74]. Another method for 3D imaging utilizing the motorized linear stages is to translate the ultrasound transducer continuously at a constant speed over a region of interest to obtain a 3D volumetric ultrasound dataset. This continuous translation scanning with ultrafast ultrasound imaging has been reported[73] in 3D volumetric imaging of kidney vasculatures, and breast lesions by Chen et al[73]. This approach involves the continuous translation of a 1D linear array transducer at a constant speed to acquire a stack of B-mode images. Acquired images were processed with singular value decomposition based clutter filter to extract the flow signal from 3D volumetric data. However, the limitation confronted with continuous scanning approach is in terms of deteriorated image quality attributed to that interference noises which were caused by the translation of transducer at the constant speed, which ultimately affects the visibility of micro-vessels.

In this chapter, we presented the 3D volumetric imaging of superficial microstructures via step-by-step scanning and continuous scanning approaches to understand the phenomenon of 3D volumetric imaging with mechanical translation. Also, elaborated the feasibility of 3D volumetric imaging performed via continuous mechanical scanning approach in visualization of *in-vivo* superficial micro-vasculatures. Further, will elaborate about the proposed image processing workflow to overcome the limitation of translation motion (interference) noises that appeared in the acquired 3D volumetric dataset due to continuous translation of transducer. The proposed image processing algorithm encompass section-wise region-based SVD filtering which extracts the flow signal from different layers of the skin from each location of 3D volumetric area, a non-local means (NLM) filter[51] which effectively remove the noises and improves the sensitivity and visibility of *in-vivo* superficial micro-vessels in 3D volumetric visualization. A top-hat transform morphological filter, which suppress the remaining background noises and enhances the overall image contrast of the processed power Doppler images which ultimately enhances the visibility of micro-vessels.

6.1. Elevational Resolution (Slice thickness)

In the plane of two-dimensional imaging, an object or feature that is orthogonal to the imaging plane would appear as a straight line image or edge. On the other hand, in the plane of a three-dimensional imaging, an object or feature orthogonal to the imaging plane appear as a cross-sectional, and it would be visible as a slice within a full three dimensional view. In the context of medical imaging, orthogonal to the imaging plane referred to as a direction or orientation that is perpendicular or at the right angle to the imaging plane (axial and lateral) in which the image is taking place. The concept of being orthogonal is essential in imaging because it helps to define the spatial relationship and orientation of objects within the imaging field, allowing for accurate interpretation of the images in 3D. Spatial resolution of 3D volume comprised on axial resolution which is the ability of the ultrasound system to distinguish two points appeared in parallel to the beam, while the lateral resolution defines as the ability to distinguish two points appeared perpendicular to the ultrasound beam. On the other hand, elevational resolution defines as the ability of an ultrasound system to distinguish and resolve structures in the elevational or out-of-plane dimensions or orthogonal to the imaging plane. It defines as the system's ability to differentiate between structures located at different depths along the ultrasound beam's propagation in elevational direction. In other words, elevational resolution measures how ultrasound system can distinguish objects in the third dimension (elevational), which is perpendicular or orthogonal to the imaging plane (axial and lateral). It mainly depends on the ultrasound transducer's element height in much the same way that the lateral resolution is dependent on the ultrasound transducer's element width.

The ultrasound beam has a three-dimensional shape, and the out-of-plane shape of beam is wider than the in-planes (axial and lateral) axis. The shape or thickness of the ultrasound beam in an out-of-plane scan is determined by the combination of the element size (height of element) and the focus of the acoustic lens, and thus these both values are fixed in every commercially available transducer. The initial width of the beam near to the transducer is equal to the height of the transducer's element, as it moves away from the transducer the shape of beam become narrowed until it reaches the least point of elevational focus at the position of elevational focal depth. As it crosses the elevational

focus depth the beam diverges again as illustrated in Fig. 6.1 (b).

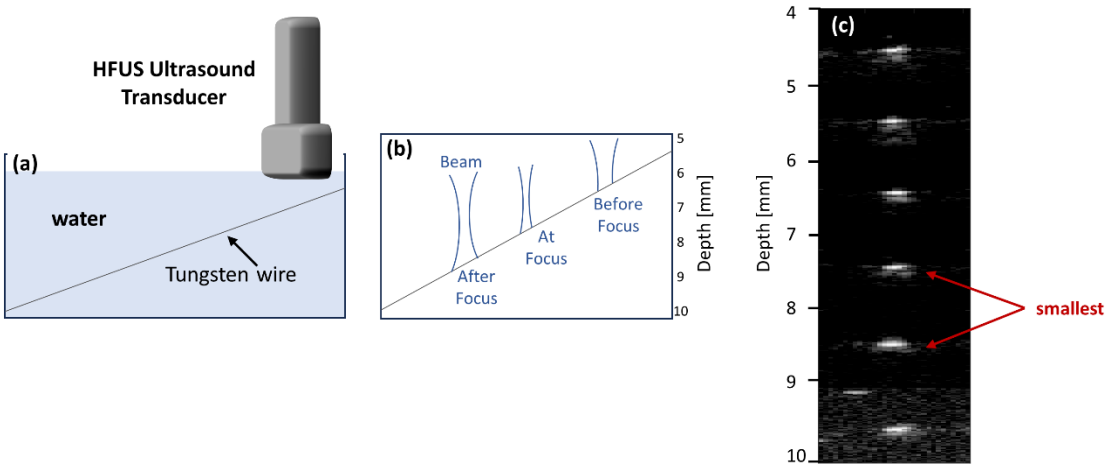

Fig. 6.1. Experimental setup to measure elevational resolution. (a) a wire phantom, (b). Illustration of beam profile in elevational direction. (c). Wire scatterers signal from different axial depth positions.

As mentioned above, the elevational resolution of a transducer is the ability to distinguish two points in the elevational direction of ultrasound beam. Hence it depends on the element height and the acoustic focal length. Theoretically it can measure as per following equation:

$$\textit{Elevational Resolution} = \textit{wavelength} \times (\textit{elevational focus} / \textit{height of element})$$

In order to observe the signal characteristics in terms of elevational resolution in 3D volumetric imaging, a theoretical value of the utilized L38-22v linear array high-frequency array transducer was measured as:

$$\textit{Elevational Resolution} = 0.0513 \times (8.0 / 1.8)$$

$$\textit{Elevational Resolution} = 0.0513 \times 4.44$$

$$\textit{Elevational Resolution} = 0.2280\ mm = \mathbf{228\ \mu m\ (Theoretical\ Value)}$$

Where, the elevational focus of transducer (L38-22v) is 8.0 mm, the elevational

aperture (height of element) is 1.8 mm and the wavelength of the beam at the center frequency of 30 MHz is 0.0513 mm.

6.1.1. Experimental Set-up

Theoretical resolution are often measured under ideal conditions, however in real-time conditions various factors such as signal characteristics, system parameters and environmental conditions affects the actual resolution. Measuring the experimental resolution is also considered as an important aspect in evaluation of system's performance and provides an insight into how the system performs in practical scenarios. Also, the experimentally measured values are meant to validate and verify the theoretically measured values.

An efficient experimental setup has been proposed to measure the elevational resolution of utilized HFUS probe L38-22v, as shown in Fig 6.1 (a). A wire phantom was designed to obtain the elevational beamwidth by placing the ultrasound transducer perpendicular to the direction of the suspended wire. The phantom was composed of 3D printed box with dimensions of 12, 32, 50 mm in depth, width and height respectively. The wire phantom was designed in order to acquire the ultrasonic signal from several depth positions from 0 mm to 10 mm. The box of the phantom was filled with water in which a tungsten wire of diameter 25 μm is placed in vertically tilted position as shown in Fig 6.1. (a). Due to the inclination of the wire in phantom box, the vertical height of the scattered point of wire displayed on the beamformed B-mode image corresponds to the beam width (w) in the elevational direction. Since w = h/tan 45[78], as also illustrated in Fig 6.1. (b).

Scanning from the right corner of the wire phantom or consider as the starting point of wire from the right side to the end of the phantom or up to the left side of the phantom enables to obtained the complete elevational beam profile at different axial depth positions. The high-frequency ultrasound transducer mounted with holder was used to acquire the ultrasonic signal from different depth positions. The height of the beam was then calculated to measure the elevational resolution at six different depth positions while moving the transducer along the wire perpendicularly. As the transducer move from right

to left side of the phantom. The beam of the ultrasonic beam was wider at the superficial depth and narrowed down around the transducer elevational focal depth of 8 mm and again it diverges while moving beyond the focal point as illustrated in Fig 6.1. (b). The intensity profiles from each depth position were acquired vertically from the point scatterer of inclined wire in obtained B-mode images and the full-width half maximum (FWHM) was measured respectively. As in this scenario, we measured the height of suspended wire via a scattered point intensity, hence the obtained intensity profile was observed non-linear. To create a linear intensity plot with a single peak, we applied a MATLAB built-in gaussian fit model and measured the FWHM from the maxima and minima of the intensity peak. The process was repeated at each depth positions and the complete elevational beam profile was obtained.

6.1.2. Results

The obtained intensity profiles from each depth position were analyzed and the FWHM values were determined as shown in Fig. 6.2. As the transducer move from right to left along the suspended vertically inclined wire, the elevational beamwidth varies from shallow to in depth axial positions. Hence the elevational resolution also changes from the shallow depth to deeper positions. As the beamwidth at the shallow region is similar to the height of the element, it than narrow down at the transducer elevational focus and then again diverges as illustrated in Fig. 6.1. (b). Table 6.1 shows the obtained elevational resolution values from different axial depth positions. It was observed that at the depth of range 7.5 – 8.5 mm, the minimum values of the elevational resolution were measured. This observation supports the idea that the utilized transducer (L38-22v) retains the precise elevational resolution at the focal depth of 8 mm. At this point of transducer elevational focus, the measured resolution values were observed in range of 225 – 307 µm as graphically represented in Fig. 6.3.

In comparison to the measured theoretical value of elevational resolution of 228 µm of utilized L38-22v ultrasound transducer at the focal depth of 8 mm, the experimentally measured values of elevational resolution was in the range of 225 µm – 307 µm from the depth positions of 7.5 mm and 8.5 mm respectively. From these results, it was observed

that the elevational resolution was varied at different depth positions. The minimum values was observed at the depth position of 7.5 mm and 8. 5 mm. The slice thickness or the width of the beam in elevational direction was observed to be in the range of 551 µm to 225 µm.

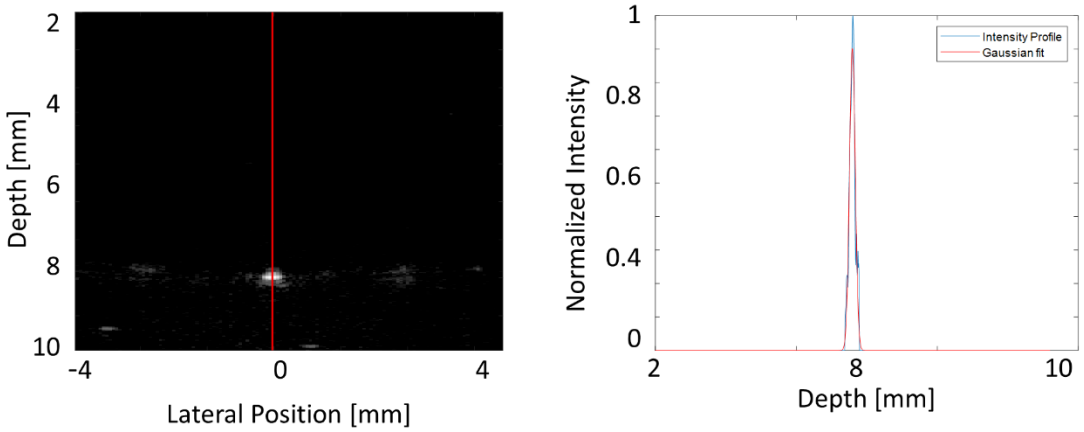

Fig. 6.2. Measurement of intensity profile to obtain FWHM to calculate the elevational resolution.

Table 6.1 Measured elevational resolution from different axial depth position

Depth	Elevational Resolution
4.5 mm	551 micron
5.5 mm	393 micron
6.5 mm	410 micron
7.5 mm	225 micron
8.5 mm	307 micron

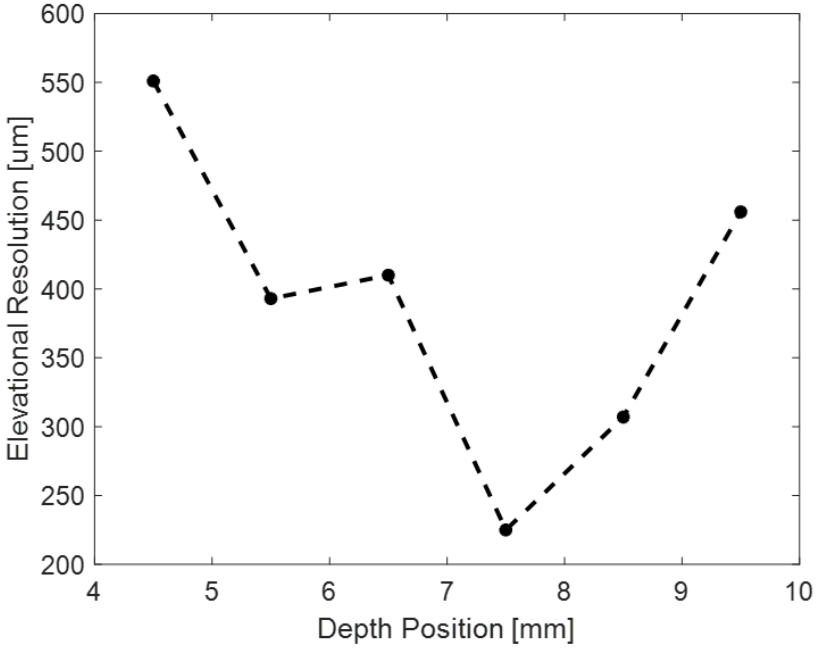

Fig. 6.3. Measured elevational resolution from different depth position

6.2. 3D volumetric Imaging

3D volumetric ultrasound imaging with 1D linear array transducer is mainly performed by mechanical scanning. It is performed by acquiring multiple slices of 2D ultrasound images from different scanning approaches [79, 80] and rendered to reconstruct the 3D volumetric image to visualize the morphology of internal structures in multi-dimensional view.

6.2.1. Step-by-Step mechanical scanning

Step-by-step is one of the mechanical scanning approach, in which the ultrasonic signal was acquired from different positions along the elevational direction in an iterative scanning manner. The ultrasound probe was placed perpendicular to the imaging object such as in the case of flow tract as shown in Fig. 6.4. The ultrasonic signal was acquired in steps via sequentially translating the probe over the object to completely scan the imaging area in iterative manner. Later the obtained ultrasonic signal from each respective step was processed to generate an image which represents a 2D slice of 3D volumetric data. Once all the sequentially acquired data from each step was processed, the obtained 2D slice images were merged to reconstruct a 3D volumetric data. The major limitation of step-by-step scanning approach is that the acquired ultrasonic signal in sequential steps from different imaging positions results in acquisition of signal asynchronously. Also, due to the acquisition of signal in multiples steps, the scanning time and the data acquisition time is more to observe the moving objects in real time scenarios. Therefore, this iterative translation approach has been used effectively for brain functional imaging or imaging of stationary objects such as small animals to detect the vascularity in tumor angiogenesis[74-77, 79,80].

6.2.2. Continuous mechanical scanning

In comparison to the iterative mechanical scanning, continuous mechanical scanning involves the translation of the transducer continuously at constant speed in one direction. As shown in Fig. 6.5, the ultrasound transducer was placed perpendicular to the imaging object and translated continuously in elevational direction. Consequently, the ultrasonic signal was acquired synchronously from the imaging area and the acquisition and scanning time is also very small because a single signal acquisition event was used to acquire the data, resultantly this approach is faster scanning approach. However, this approach faces certain challenges in visualization of structure. Due to continuous scanning of imaging area, the acquired ultrasonic signal appeared as distorted by certain interference noises. These noises were created due to the continuous motion of transducer which appeared in between the acquisition of different frames. These interference noises

appear as speckle in the obtained B-mode images and sharp signal leap in processing of micro-flow signal which affects the ultrasensitive Doppler filtering process.

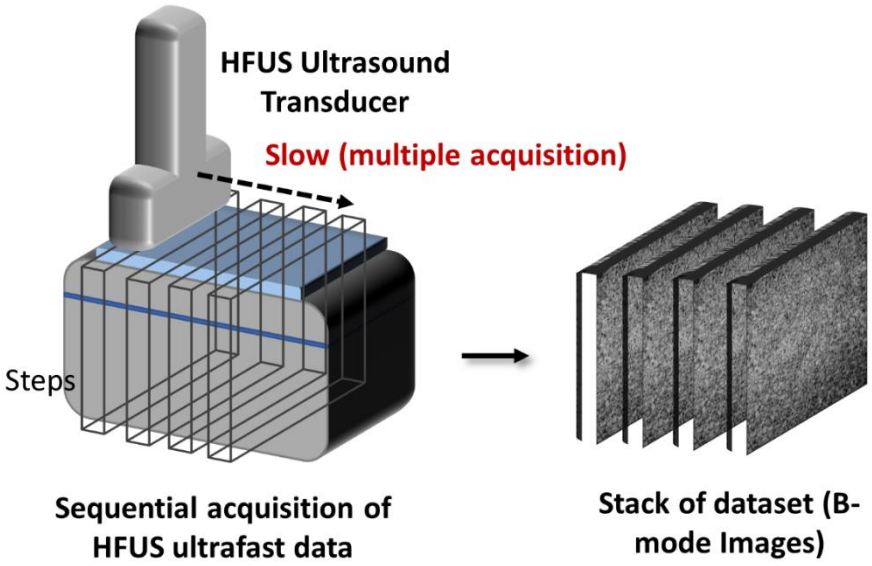

Fig. 6.4. Illustration of step-by-step (iterative) mechanical scanning approach.

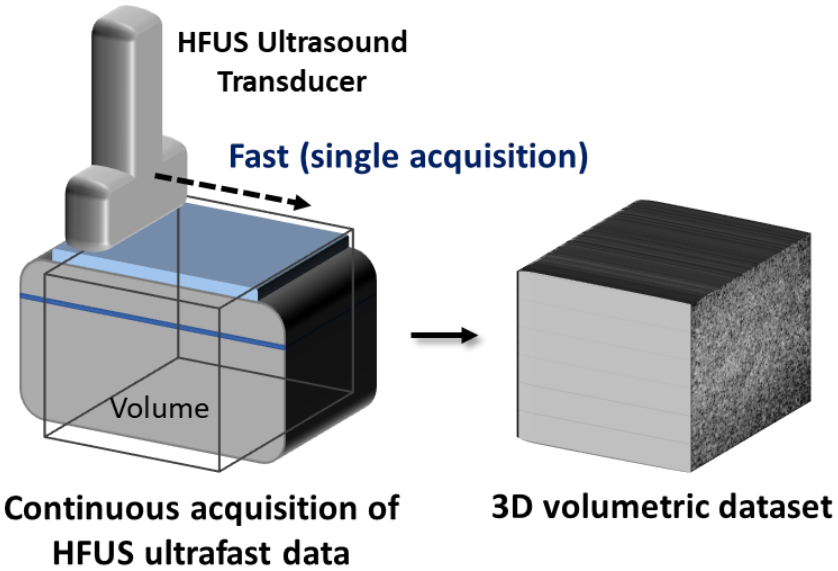

Fig. 6.5. Illustration of continuous (at constant speed) mechanical scanning approach.

6.3. 3D Volumetric Imaging Experimental Setup

To perform 3D volumetric imaging of superficial micro-vessels, an efficient experimental setup was proposed. Both the approaches of 3D volumetric mechanical scanning: the iterative scanning and continuous scanning was performed to observe and evaluate the signal characteristics. Devised experimental setup shown in Fig. 6.6 was comprised on Vantage Verasonics ultrasound (Verasonics Inc., Kirkland, WA, USA) research purpose system to transmit and acquire the ultrasonic signal, 2D stages connected with controller to translate the transducer in iterative manner as well as continuously at constant speed. A micro-flow phantom with flow channel of 200 µm at the superficial depth of 4 mm was utilized which mimics the superficial micro-vessels. A determined flow circuit assembly was implemented to infuse the blood mimicking fluid (BMF) in the micro-flow channel via a syringe pump at a specified flow velocity to observe the characteristics of flow signal under both of scanning approaches.

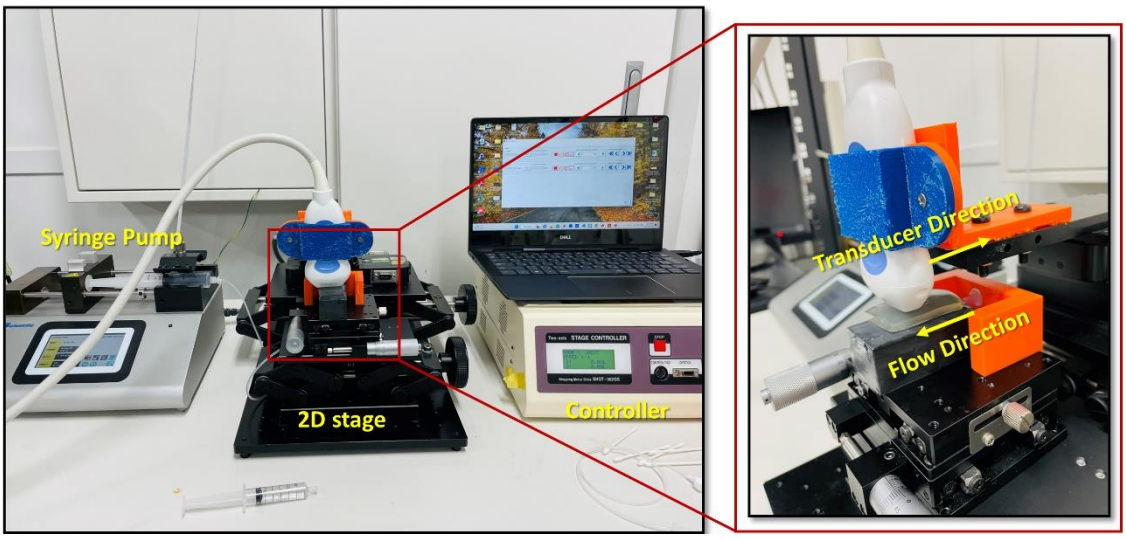

Fig. 6.6. Experimental setup for 3D volumetric imaging

6.3.1. Signal acquisition via Step-by-step mechanical scanning

To visualize the micro-phantom in short-axis position in step-by-step scanning approach. The ultrasound probe was mounted with transducer holder as shown in Fig. 6.6,

which was a 3D printed jig and was designed in order to connect the transducer (probe) with 2D mechanical stages (OSMS(CS)20-35, Sigmakoki Co., Ltd, Japan). The 2D stages were connected with two axis stage controller (SHOT-302GS, Sigmakoki Co., Ltd, Japan) to translate the stages in the elevational direction. The step-by-step data was acquired by translating the transducer in two different settings. At first to scan a 200 µm straight flow tract, the data was acquired in 10 steps with step size 1 mm as shown in Fig. 6.7 (a). Secondly to scan a bifurcated 300 µm flow tract, the data was acquired in 18 steps with step size of 0.5 mm as illustrated in Fig. 6.7 (b).

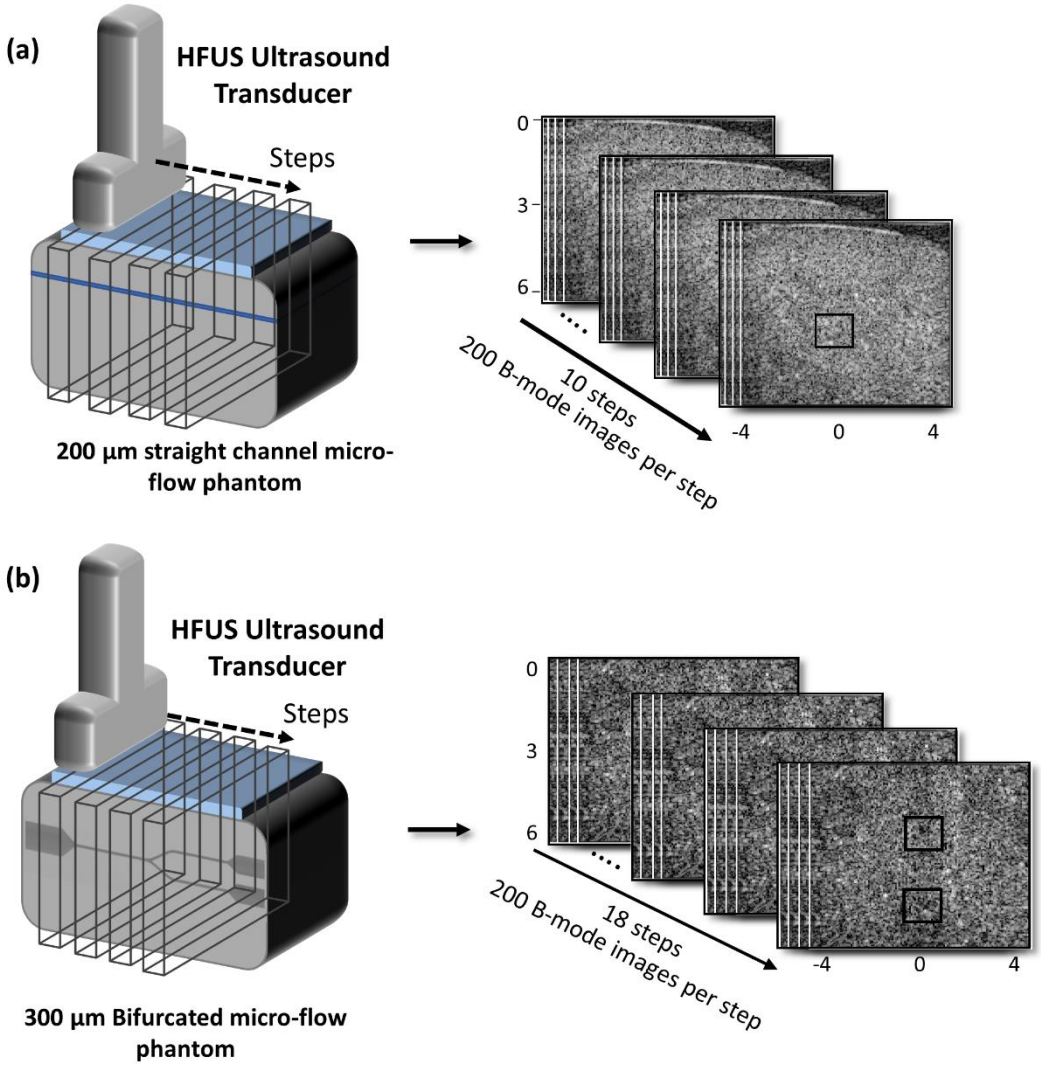

Fig. 6.7. Experimental setup for 3D volumetric data acquisition. (a). step-by-step mechanical scanning on straight micro-flow phantom (200 µm). (b). step-by-step mechanical scanning on bifurcated micro-flow phantom (300 µm).

Respective micro-flow phantoms were connected with a syringe pump to infuse the BMF at flow rate of (200 µm = 37µl/min and 300 µm = 84µl/min) at flow speed of 20 mm/s. A linear array high-frequency transducer connected with a vantage system was used to acquire the ultrasonic signal from micro-flow tracts at center frequency of 30 MHz. 128 elements of transducer were excited to transmit ten plane waves with compounding angles of -5 to + 5 degree at pulse repetition frequency of 5 kHz. During each step of scanning 200 B-mode compound frames were acquired. Later, the obtained dataset of ultrafast ultrasound from both micro-flow phantoms underwent further signal processing. Each acquired step was processed with singular value decomposition (SVD) based clutter filter to truncate the clutter signal and extract the desired flow signal as shown in Fig. 6.8. Subsequently, the processed 2D images were stacked in a concatenated matrix and were rendered using the MATLAB in-build volume viewer for 3D volumetric realization of micro-flow phantoms of two different dimensions and geometries the straight micro-channel and the bifurcated micro-channel.

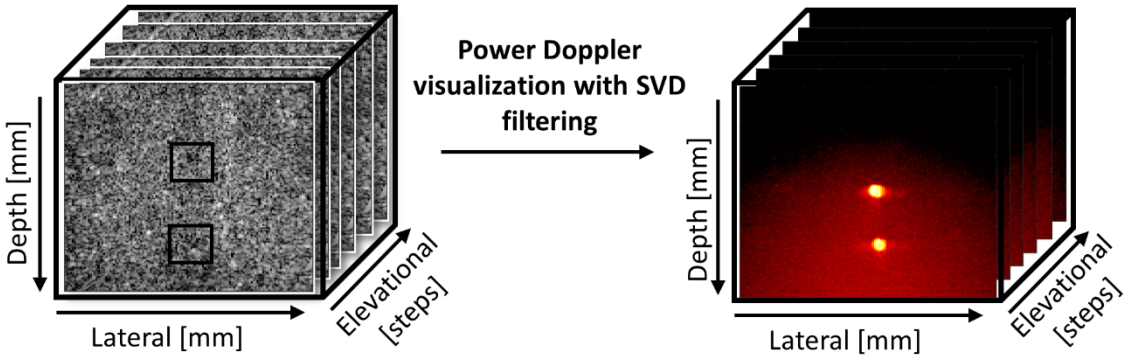

Fig. 6.8. Processing of obtained 3D volumetric data with SVD clutter filter

6.3.2. Signal Acquisition via continuous mechanical scanning

In this approach the transducer was translated continuously in elevational direction at a distance of (distance 5 mm and 10 mm) and the probe was mounted via 3D printed probe holder with 2D stage (OSMS(CS)20-35, Sigmakoki Co.), which were controlled by controller (SHOT-302GS, Sigmakoki Co.) to translate the transducer continuously with a constant speed of (1 mm/s and 2 mm/s) as shown in Fig. 6.9. A linear array transducer was used for transmission and reception of ultrasonic signal. 2500 compound frames were obtained at pulse repetition frequency of 5 kHz. Each frame was compounded by ten steered plane waves. The start of the acquisition was synchronized with the triggering of the vantage and motorized translation stage. A straight tube micro-phantom (200 µm) was connected with flow circuit assembly comprised on syringe pump and tubing and was connected with micro-phantom with the help of IV catheters. This assembly facilitated the infusion of BMF at a flow rate of 37µl/min.

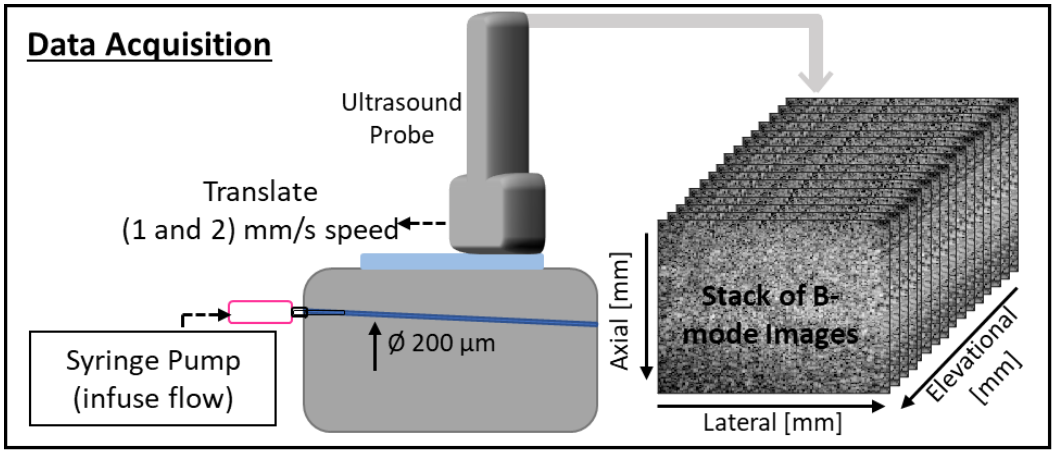

Fig. 6.9. Acquisition of ultrafast ultrasound data from 200 µm flow tract via continuous mechanical translation.

6.3.2.1. Stage Controller settings

To translate the transducer at constant speed of 1 mm/s and 2 mm/s. The transducer was mounted with 2D stages via probe holder. The transducer mounted stage was controllerd by a 2D-stage controller. In controller settings, the translation of stage was

programmed with continous movement at the constant speed of 1 mm/s and 2 mm/s.

To program the translation of these 2D stages, an eidtable program has been written in the controller memory switches. To do so, certain prior settings in the stage controller has been accomplished with the help of controller manual. Those settings include:

1. Memory Switch setting.
2. Calculate the constant speed values.
3. Edit a program.

1. **Memory Switch setting:** In memory switch setting, at first we need to press the "Ctrl" and "SET" buttons in MANUAL mode of the controller simultaneously via using a connected control pad of controller. The memory switch settings screen will be displayed on the controller screen. Later, press the "-2(4)" button on the cross-shaped button of the control pad to change the memory swtiches. Among those memory swtiches the translation speed was set by selecting the starting speed value and final speed value with zero accelration to maintain the constant speed. The translation speed setting of 1 mm/s was set under the memory switch of speed1 and 2 mm/s was set under the memory switch of speed2.
2. **Calculation:** The values of speed 1 mm/s and 2 mm/s of transducer translation was set based on number of pulses per second (PPS) values. In controller the pulses per second represents the rate at which pulses occur in one second. The reciprocal of PPS value converts this value it to the unit of seconds. The resolution of transducer motion was set under setting of memony swich DIVIDE, in these experiments we choose the default value of 1 μm of translating step. Resolution or travel per pulse/distance per pulse are consider to the same concept, which is the amount of linear distance the motorized stage moves per each pulse. Received by the motor controller. It is often expressed in units μm or mm per pulse. It tells how much the stage will move for each pulse of the motor. Therefore,

Resolution = Distance per pulse = 1 μm = 0.001 mm.

and i.e., 500 PPS = 1/500 = 0.002 s

Memory switch Speed1

Travel per pulses = 1000 PPS = 1/1000 = 0.001 s

Speed(V) = Distance per pulses (mm)/time per pulses (s)

Speed(V) = 0.001/0.001

Speed(V) = 1 mm/s

Memory switch Speed2

Travel per pulses = 2000 PPS = 1/2000 = 0.0005 s

Speed(V) = Distance per pulses (mm)/time per pulses (s)

Speed(V) = 0.001/0.0005

Speed(V) = 2 mm/s

Beside distance travelled in each settings was also adjusted to travel the desired distance at each chosen speed settings.

Distance travelled = Distance per pulse × Number of pulses

Where number of pulses defined as the the total distance travelled by stages in linear translation at allocated speed. Therefore, at speed of 1 mm/s for duration of 5 seconds, the distance travelled is 5 mm, while at speed of 3 mm/s for duration of 5 seconds (signal acquition time), the distance travelled is 10 mm/s according following equation.

Distance (S) = Speed (V) × Time (T)

Distance (S) = 1 (mm/s) × 5 (s)

Distance (S) = 5 mm.

Distance (S) = 2 mm/s × 5 (s)

Distance (S) = 10 mm

In this regard, the number of pulses required to cover the travel distance of 5 mm and 10

mm was obtained by follwing equation.

$$\text{Distance travelled} = \text{Distance per pulse} \times \text{Number of pulses}$$

$$\text{Distance travelled} = 0.001 \text{ mm} \times 5000 \text{ pulses}$$
$$\text{Distance travelled} = 5 \text{ mm}$$

$$\text{Distance travelled} = 0.001 \text{ mm} \times 10000 \text{ pulses}$$
$$\text{Distance travelled} = 10 \text{ mm}$$

3. Edit a program:

To edit a translatio program in controller, at first press the (MODE) button of control pad of controller, until it reachs the edit mode on controler screen. In the edit mode on the screem press the (SET) button to initiate the program editing (writing). After pressing the (SET) button, the program number selection screen will appear on the controller screen. Selecte the program by pressing the top and bottom button of cross-shaped button of control pad. Once the program was chosen, press the (SET) button again, the screen will change in to the edit mode of the program. Data entry points in the program edit mode was separated by commas. Move the cursor using the left and right buttons of cross-shapped button of control pad. There are mainly three aspects of program which are needeed to be set for each allocated speed condition. Fig 6.10. illustrate all the aspect of the program and Table 6.2 presents the translating program. Each aspect of program are defined below:

1. Operating pattern: In both programs of translating speed of 1 mm/s and 2 mm/s, the operating pattern of 0 and 99 was set in the program to start and stop the translation. 0 is a normal operation mode which moves the stage at specified co-ordinates and stop and 99 represents the the end of the program, which means to terminate the translation.
2. Movement distance: In the present experimental setup, the 2^{nd} axis (2^{nd} stage) was utilized to translate the transducer. In this regard, the input pulses relative

to the distacne travelled in each setting. Here the values of 1000 and 2000 for 5 mm and 10 mm respectively.

3. Speed: As per the settings of memory switches, the speed of 1 and 2 were edited with respective to each program settings.

Fig. 6.10. Front panel of two-axis stage controller illustrates the editable program.

Table 6.2. An editable program of two-axis stage controller

Line Number	Operating Pattern	1st axis coordinate	2nd axis coordinate	Output instruction	Speed setting	Wait time
1	0	0	1000/2000	0	1/2	0
2	99	0	0	0	0	0

6.3.2.2. Synchronization of stage controller and vantage Verasonics system

In order to acquire the 3D volumetric signal via continusly translating the transducer, the stage controller (translate the 2D stages) and vantage verasonics system (acquire the ultrasonic signal) to start the imaging sequence and translation synchronously. To do, an arduino borad was used to provide a trigger signal and Input signal to vantage system and

controller respectively to initiate the acquisition and translation process. Schematic diagaram in Fig. 11. has shown the respective connections between the vanatge system, arduino and the controller.

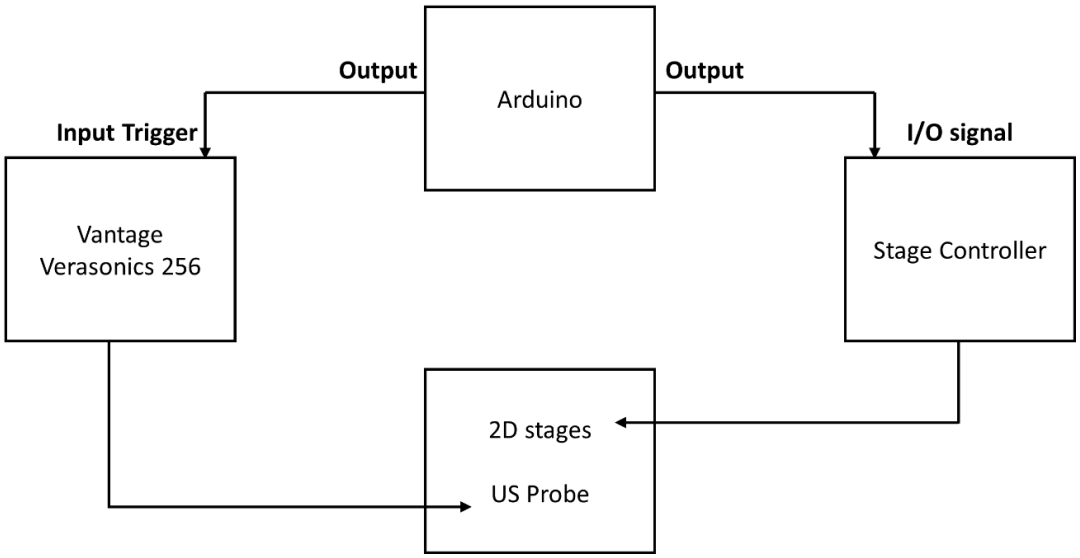

Fig. 6.11. Illustration of connection between Vantage system, two-axis stage controller and the Arduino to make signal acquisition and translation synchronous.

1. **Vantage Verasonics System**: The vantage verasonics system can receive both trigger in and trigger output signal via a dedicated BNC connectors located on the (input/output) panel on the rear side. In this study to synchronize the vantage system, we utilized the input trigger BNC connector from the rear panel. To do so, at first the trigger command was mentioned in the imaging sequence in SeqControl event as “Trigger_2_Falling”. The command specified the receiveing of trigger signal at specified event in imaging sequence. Trigger_2_Falling command presents activation of signal at the falling edge of received trigger input signal at the BNC conector. Later, the trigger input signal was applied to the BNC connector from an external source to initiate the triggering process. The main condition for tirgger input signal to vantage system was that the input pulse to the

connector should be a signal level of 3.3 volts LVTTL. The voltage level must not exceed 5.5 volts.

2. **2D stage controller**: To translate the 2D stages in specified direction at specified speed. The translation program was written in the controller as explained above. To initite the program, we utilized the I/O signal of the controller to translate the stages as per eidted program. In the controller, when the opertion is programmed from an external device, motorized operations follow the instructions in the program by turning START input in I/O signals in the rear panel of the controller. To do so, we used the controller rear 10250-52A2Jl SCSI Connector (3M connector) to connect the I/O pins of connector on Pin # 18 (START High) and Pin # 43 (START Low). The active high signal of voltage (3.5 V – 5 V) on these pins the programmed motorized operation will be initaite by the controller as per per chosen program of translation. On the defined start pins of SCSI connetor, we soldered the wires on high (Pin 18) and low (Pin 43) pins, later connected the 3M connector with socket at the rear I/O pannel of controller. The main conditions to input signal was that of active high signal which refers that the input voltgae lies in the range of 3.5 V to 5 V.
3. **Arduino Micro-controller (Mega 2560):** To provide the input signal and trigger signal to 2D stage controller and vantage verasonics system simultaneously to create the synchronization, we utilized the arduino borad. Vantage BNC connector was connected with input pin 9 and 3M connector start pin was connected with input pin 10 of arduino. The negative terminals of the both connectors was grounded with the ground pin of arduino. The input voltage of 5V was provided to arduino via USB connection with computer. To initiate the translation and acqusition, a program from arduino software was uploaded on the arduino borad using serial interfacing between the arduino borad and computer. Fig. 6.12 shows the program for the generation of pulses at digital input pins of arduino.

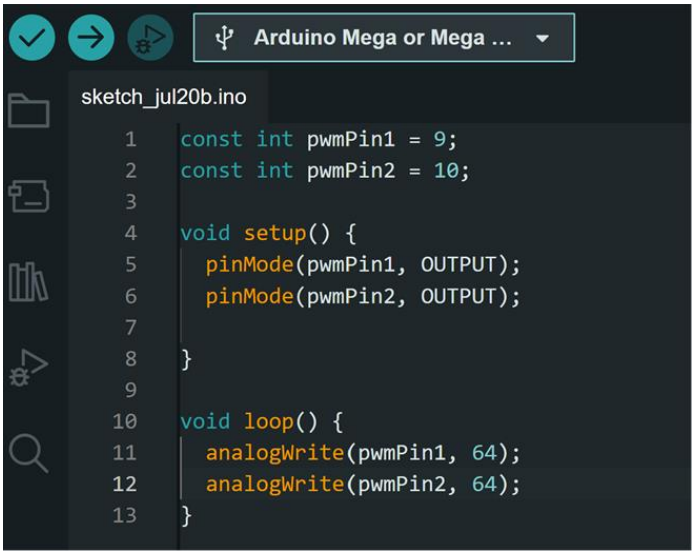

Fig. 6.12. A window of Arduino software presenting a program to send the signal to vantage and controller to initiate the respective process.

6.4. 3D Volumetric Image Processing

In iterative mechanical scanning approach, a number of beamformed B-mode images acquired from each acquisition step were stacked into a space and time matrix with dimensions of (nz × nx × ne), where nz and nx are the spatial samples along the depth (z) and lateral (x) dimensions, while ne is the number of B-mode images referred to as the Doppler ensembles or frames. This matrix is then filtered by performing a SVD to truncate a number of singular components corresponding to stationary and slow moving clutter signal, filtering the remaining signal comprised on the flow signal and the noise. The resulting filtered matrix is averaged over the ensemble length to compute the power Doppler image.

On the other hand, in continuous mechanical scanning, unlike the step-by-step acquisition, each frame is not acquired from the known imaging area and therefore averaging over an ensemble's length will impact the image resolution. When this matrix is filtered in the same way as the traditional SVD, where ny (elevational direction) is taken to be the number of ensembles or frame size ne, we are left with a SVD processed

power Doppler image in which the continuous spatial signal acquired from the elevational direction was fused results in the overlayed of signals which hinders the extraction of desired vascular flow signal. In this manner, via continuous mechanical scanning, we are unable to average over ny, as it contains the spatial components of the signal as well in elevational direction from over the whole translation of imaging area.

Fig. 6.13 Illustrates the implementation of global SVD on the acquired ultrasonic data with continuous mechanical scanning. The application of SVD processing on a lengthy sequence of ultrasonic signal introduces more mixtures between blood and tissues components. If the singular components extracted between at an arbitrary threshold, the quality of the resultant Doppler image may compromise due to the mixture of signal component. As illustrated in the spatial vector analysis in Fig. 6.13 that due to the motion of the transducer translation, a distorted signal is created which appeared as interference noises in the singular values decay graph as well as can be observed in the spatial covariance matrix. The distorted signal overlayed between two distinct subspace regions of flow signal and tissue signal. Due to these interference noises, it was quite cumbersome to choose the cut-off threshold value to filter out the desired flow signal. Also, it was observed that these interferences noises increases by increasing the transducer translation speed. The faster the translation speed the more the interference noises. As shown in Fig. 6.13 the distorted noises with transducer speed of 1 mm/s was lower which gradually increases with the translation speed, and observed higher under speed of 3 mm/s.

Furthermore, to understand the characteristics and origin of these noises generated from the translation of transducer. At first we measured the thickness of each 2D slice image acquired from imaging area via continuous mechanical translation. Suppose that the translation speed of the transducer scanning is 1 mm/s, the signal acquisition time is 2 sec which shows that at PRF of 5 kHz and ten compounding angles, 1000 compounded B-mode frames can be acquired. Relied on those settings, the distance covered by transducer is 2 mm. Based on above values the slice thickness was measured by the following equation:

$$\textit{Slice thickness} = \textit{Distance covered by transducer} / \textit{Total acquired frames}$$

$$\textit{Slice thickness} = 2\ \textit{mm} / 1000$$

Slice thickness = 0.002 mm / frames

Slice thickness = 2 µm.

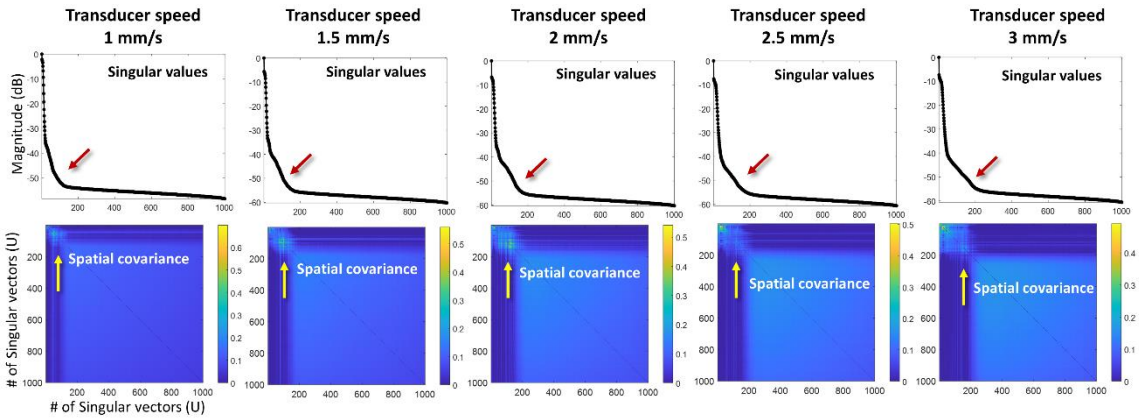

Fig. 6.13. Spatial singular value analysis to observe the effect of interference noises in determination of singular value cut-off threshold in SVD processing of ultrasound data acquired via continuous mechanical translation with different translation speed.

If with the transducer speed of 1 mm/s and 2500 compounded B-mode frames were acquired at the signal acquisition time of 5 sec. Then the distance covered by the transducer is 5 mm and the value of slice thickness is 2 µm. From these calculations, it was observed that each frame occupied a distance of 2 µm at the translation speed of 1 mm/s. As we increase the translation speed, the slice thickness also increases which causes the creation of distorted signal in between the slices.

As the data was acquired continuously via translating the transducer at a constant speed, we observed the effect of transducer translation motion on signal characteristics. In this approach each image was acquired from a unique position of imaging area. Acquisition of frames shown in Fig. 6.14 illustrate the acquisition time and the distance covered by each frame. It is shown that in the compounded frame, each frame at a different steering angle in the pre-compounding state was also acquired at a different imaging position. To observe the noises of motion in pre-compounded frames, we measured the thickness, or the distance covered by each pre-compounded frame as well:

1 frame = 10 compounded frames

Slice thickness of 1 frame = 2 µm

Slice thinness of each pre-compounded frame = 2 µm / 10 = 0.2 µm

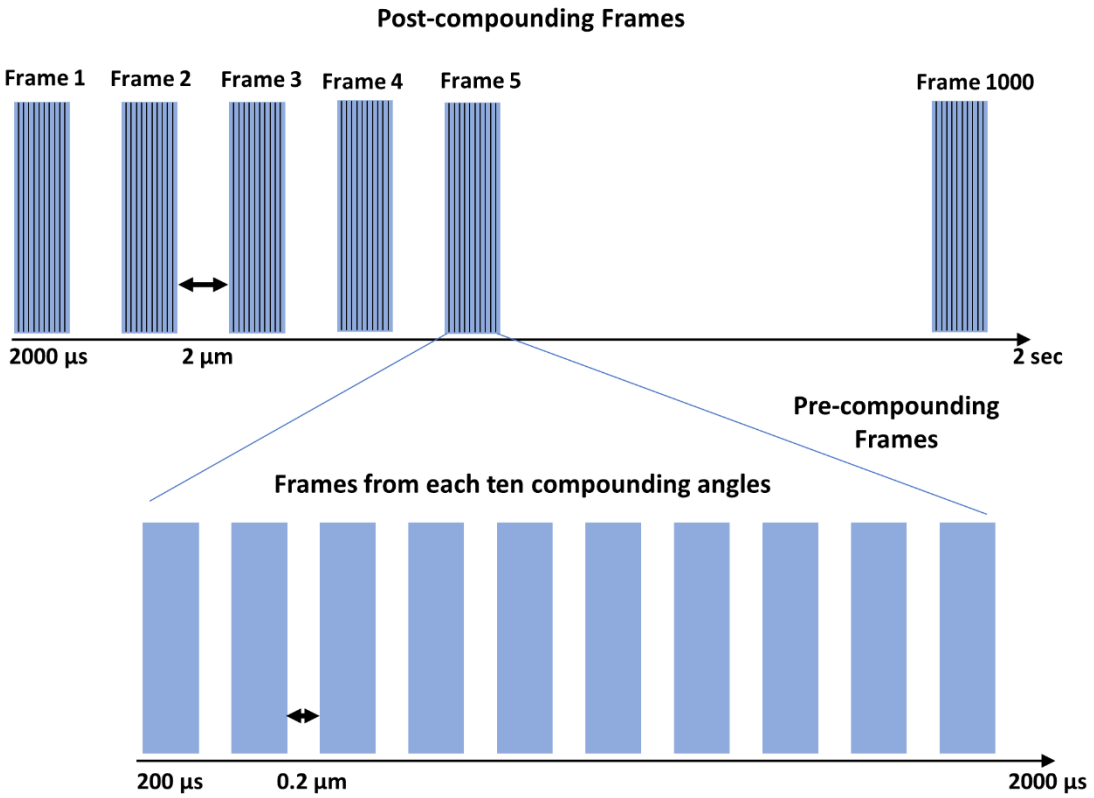

Fig. 6.14. Illustration of signal acquisition of pre-compounding frames and post-compounding frames.

Table 6.3. Distance covered by each frame or elevational thickness of each frame in pre-compounding and post-compounding state

Transducer speed	Acquired Frames	Acquisition Time	Compounding Frames	Distance Covered by each frame	Distance Covered by each Pre-compounded frame
1 mm/s	1000 frames	2 sec	10	2 µm	0.2 µm
1.5 mm/s	1000 frames	2 sec	10	3 µm	0.3 µm
2 mm/s	1000 frames	2 sec	10	4 µm	0.4 µm
2.5 mm/s	1000 frames	2 sec	10	5 µm	0.5 µm
3 mm/s	1000 frames	2 sec	10	6 µm	0.6 µm

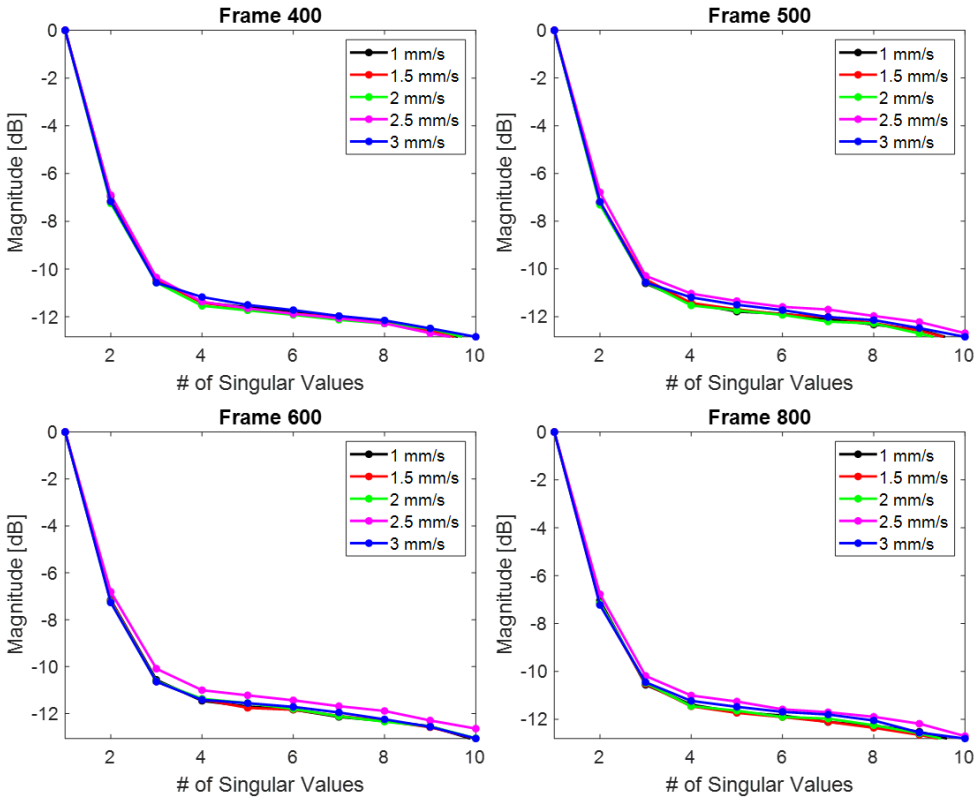

Fig. 6.15. Implementation of SVD on pre-compounding frames acquired under different translation speed of transducer.

From the above calculations, it was observed that each compounded frame has a slice thickness of 2 µm, and each pre-compounded frame has thickness of 0.2 µm at transducer speed of 1 mm/s. The obtained values shown in Table 6.3 demonstrates that the distance covered by each compounded frame and each pre-compounded frame at different speed of transducer translation. As noticed that the thickness of pre-compounded frames fall in the range of 0.2 µm – 0.6 µm under different transducer translation speed. In correspondence to utilized stage motor controller whose step resolution was set on 2 µm as a default value. Therefore, each pre-compounded frame covered the distance within the range of default values of stage controller step resolution. Also, it was observed in the Fig. 6.15 which represents the singular values decay graph of each pre-compounded frames, in which the interference noises was not observed even under higher translation speed of 3 mm/s.

6.4.1. Section-wise SVD Processing

Even though the acquired beamformed images are not sampled at the same location, a number of subsequent frames shares the similar signal statistics due to the beam-profile of 1D linear array transducer. The 1D array transducer samples a 2D images of (nz, nx), the backscattered energy from a single stationary 2D slice is also influenced by the out-of-plane environment in ny (elevational direction). The amount of energy in ny is also depth dependent and is mainly effective at the elevational focal point, also when compared to the in-plane (axial and lateral) resolution of the transducer. The out-of-plane (elevational) beam profile is wider which is relied on depth positions and beamwidth. In this perspective, the overlapping of acoustic energy in the obtained B-mode frames from the allocated space in the elevational direction due to the wider elevational beam profile. By taking advantage of this feature of beam-profile, instead of filtering a whole 3D volume acquired via continuous mechanical translation, the acquired 3D dataset was divided into a number of repeated ensembles which we called the sections of dimensions (nz × nx × ne × nrep) which gives us the situation similar to that of the traditional 2D SVD processing. Each section must have enough number of B-mode images or Doppler ensembles to map the flow signal efficiently. Also, the section thickness must rely within the range of the transducer elevational resolution explained in section 6.1 and in Fig. 6.3 to maintain the quality of image in elevational direction.

After averaging over ne, it would leave us with a number of power Doppler images spanning across the skin, in a similar way to the step-by-step 3D volumetric imaging. Choosing ensemble number has a lot of consequences when compared to stationary recordings, as you need a number of frames high enough for good delineation of tissue and blood motion without losing the spatial coherence of the frames within an ensemble.

6.4.2. Imaging Framework

The acquired ultrafast dataset with continuous mechanical scanning was then pre-processed by dividing the data into subsequent sections as shown in Fig. 6.16 (a) to perform the SVD clutter filtering efficiently via singular value thresholding to extract the

desired flow signal. Twelve sections were created by dividing the dataset comprised on (2500 frames = 5 s) as shown in Fig. 6.16 (a). Each frames comprised on (250 frames = 0.5 s) with an overlap of (50 frames = 0.05 s). The slice thickness of each B-mode image of 2500 B-mode dataset is 2 µm, with this the section thickness 2 × 250 frames is around 500 µm. Each section was then processed with SVD as shown in Fig.6.16 (b). Later, an established NLM filter[51] was implemented on each section's SVD filtered power Dopler image to mitigate the interference noises caused by the translation motion of transducer. Once all the sections were processed with combined algorithm of SVD and NLM, a 3D matrix was created to visualize the obtained flow structures in MATLAB built-in application of volume viewer as shown in Fig. 6.16 (c).

6.4.3. Non-local Means (NLM) Filtering

After performing SVD clutter filtering on each section of acquired ultrafast HFUS dataset, filtered matrix encompasses the blood flow signal and a form of additive noise caused by ultrasound system, in particular to the time gain compensation (TGC) circuit which retained in the designated singular subspace. Besides that, TGC based additive noise, another field of noises also appear in each section of 3D volumetric dataset which is caused by the motion of translation of transducer in 3D volumetric continuous scanning approach. The motion noises appeared as speckles in the images caused by the interferences in the acquisition of the signal which results in intensity fluctuation in the SVD processed power Doppler image. The TGC amplified additive background noises and the motion noises greatly changes the intensity values and deteriorates the vessels visibility, particularly in the super superficial region of the imaging area. In previous chapter, we elaborated that the combined approach of novel region-based SVD processing and top-hat morphological filtering truncates the clutter signal and suppressed the background noises respectively and enhanced the image contrast with significant improvement in superficial micro-vessels visibility. However, an additional level of denoising is also needed to mitigate the vast intensity fluctuations from the acquired 3D volumetric data via high-frame rate plane wave imaging.

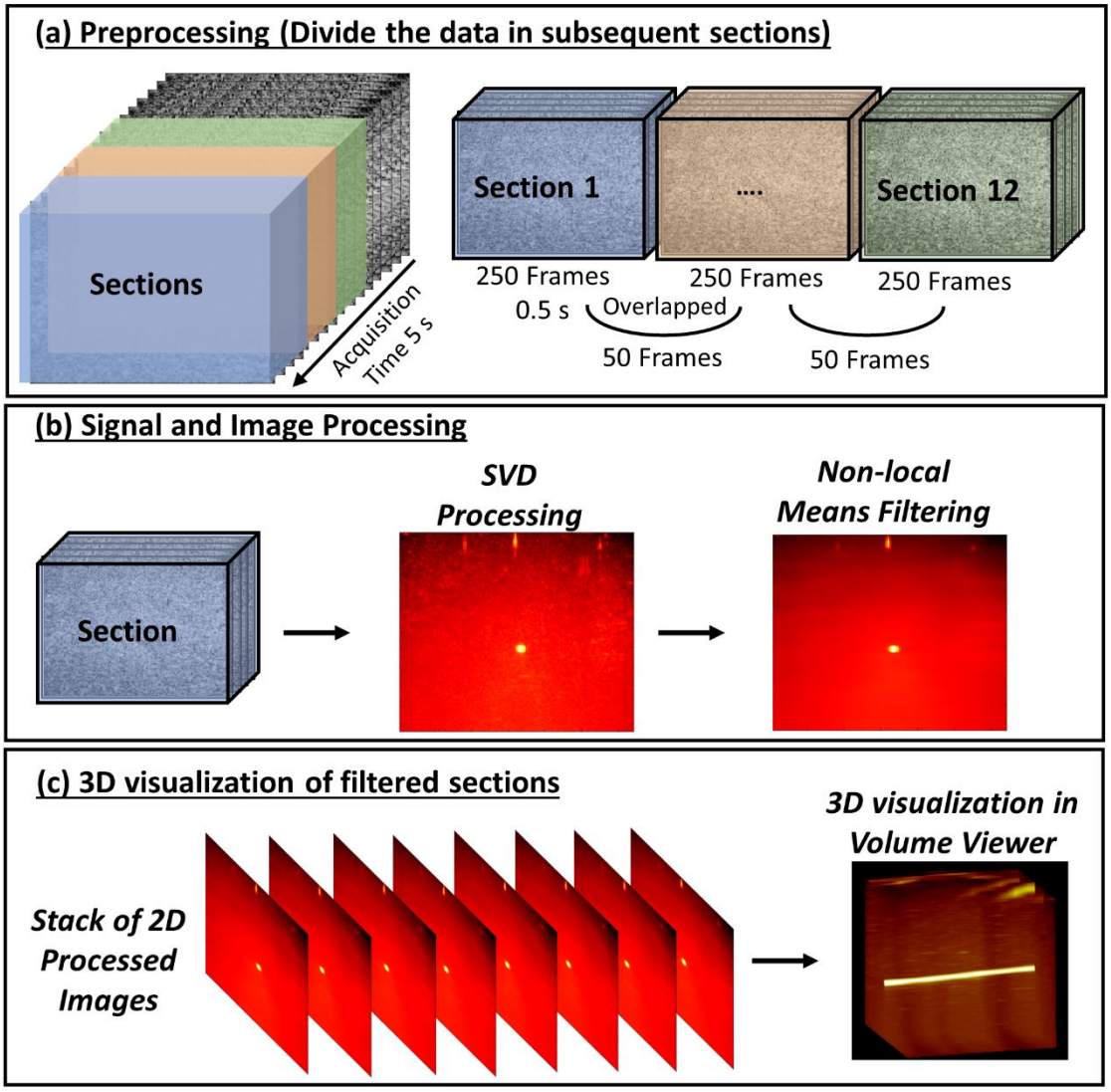

Fig. 6.16. Section-wise SVD Processing of acquired ultrafast ultrasound data 200 µm flow tract acquired via continuous mechanical translation.

Usually, the image denoising methods recover the images from the noisy measurement. There are several denoising methods [84-89] that have been proposed to eliminate the noises and restore the image quality. While these methods may employ diverse tools and approaches it must be emphasized that a wide class of image denoising methods share the same basic remark: they rely on the fundamental concept of noise reduction through averaging. In traditional local filters such as mean and median filters [96,] the denoising operation is performed by averaging only the nearby pixels within the local neighborhood.

In contrast, the non-local means filter (NLM) [90-91] does not rely solely on the pixel values in a local neighborhood around the target pixel in the imaging field, but this approach consider the similarity throughout the entire image instead of restricting to a fixed local neighborhood. The NLM filter searched for similar patches or regions throughout the entire image to compare the similarity between the targeted pixel and the neighboring pixels in different parts of the image. By doing so, it can effectively remove the noises while preserving the fine details and structures of objects in the image.

Non-local means filter is an advanced and effective denoising method for both natural and medical images. It is operated based on the principle that noisy pixels in an image can be denoised by comparing them to similar patches in other regions of the image. In the field of medical imaging, it has been used in the denoising of ultrasound imaging [91], magnetic resonance imaging (MRI) [92] and low-dose X-ray computed tomography imaging [93], positron emission tomography (PET) imaging [94] and optical coherence tomography (OCT) imaging [95]. In the perspective of ultrasound B-mode imaging [91], this filter has been implemented to reduce the speckle noises to preserve the details of anatomical structures for better diagnosis of diseases [91,97]. In the field of high-frame rate power Doppler imaging, Adabi et al [98-99] proposed the implementation of the combined approach of NLM filter and top-hat morphological filter to remove the background noises and enhance the visibility of vasculatures in power Doppler imaging. Also, in the field of ultrasound localization microscopy (ULM) song et al [100] implemented NLM filter on the clutter filtered micro-bubble signals to reduce the false localizations of noises for better ULM imaging. Inspired by the applicability of NLM in removal of speckle noises in B-mode imaging [91], and false micro-bubbles signals in ULM imaging[100], and in ultrasensitive Doppler imaging [98,99, 101] we implemented it in 3D volumetric imaging, to remove the motion noises caused by the translation of transducer in continuous scanning and preserve the blood signal and vascular structures.

Key features and advantages of NLM filter is to consider the similarity between a given pixel pair is robustly derived from intensity differences between the patches of neighboring pixels surrounding them making it effective in preserving fine details and textures in the image. Also, due to non-local averaging it retains the ability to denoise both Gaussian and non-Gaussian noises. It adapts to the local characteristics of the image,

and effectively preserve the edges and structures in the image. Following is the detailed description of implementation of NLM:

1. First an image to denoise refer as two-dimensional or three-dimensional grid of pixels values representing as the input to the NLM denoising algorithm.
2. The search window was chosen as a larger region with in the image that the NLM filter uses to search for similar patches. This window scans the entire image, and for each pixel, it identifies as set of candidate patches within the search window.
3. The reference window was then chosen as a small square area centered around the pixel in the search window. This window represents the local region that you are trying to denoise. The central pixel within the reference window is the pixel you are trying to denoise.
4. The similarity window is of the same size as of the reference window, but it's located around other pixel in the search window. The NLM filter calculates the similarity between the reference window and these similarity windows to find the similar patches.

For each pixel in the image, the algorithm selects a reference window centered at that targeted pixel as shown in Fig. 6.17. It then compares the reference window to all the other similarity windows within the search window, one by one. The comparison typically involves measuring the similarity between the pixel values in these patches, such as by computing the Euclidean distance. Later, the NLM algorithm assigns weights to the similarity windows based on the similarity between the reference window and each similarity window. The windows which are more similar receives higher weights, while less similar windows get lower weights. The denoised value of the targeted pixel in the reference window is computed as the weighted average of the pixel's values within the similarity windows, where weights are based on the similarity scores. This process is repeated for all the pixels in the image, resulting in a denoised version of the image.

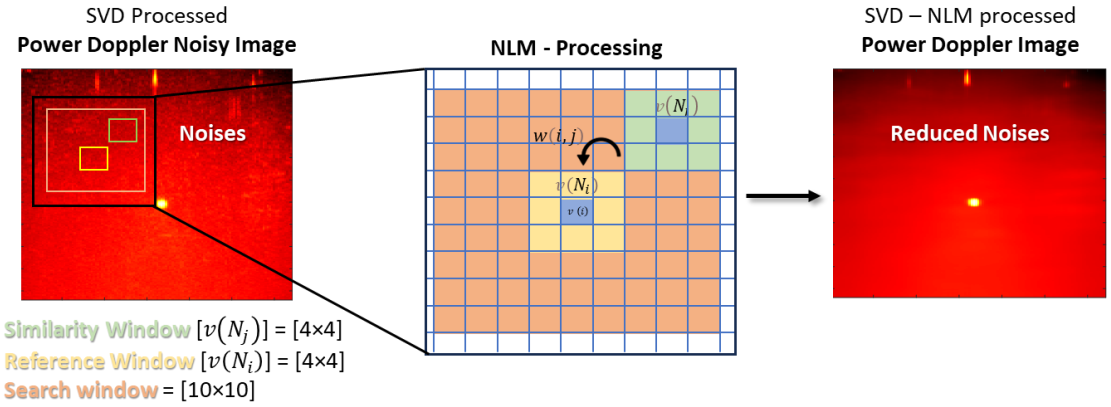

Fig. 6.17. Representation of non-local means filter processing.

Such as in a noisy image $x = \{x^i | \ i \in I\}$, the estimated value $NL[x](i)$, for a pixel *i*, is computed as a weighted average of all the pixels in the images.

$$NL\ [x](i) = \sum_{j \in I} \left(w(i,j)\ x(j)\right)$$

Where the family of weights $\{w(i,j)\}_j$ depends on the similarity between the pixels *i* and *j* and satisfy the usual conditions $0 \leq w(i,j) \leq 1$ and $\sum_j w(i,j) = 1$.

The similarity between two pixels *i* and *j* depends on the similarity of the intensity level vectors $x(N_i)$ and $x(N_j)$, where N_k denotes a square neighborhood of fixed size and centered at a pixel *k*. This similarity is measured as a decreasing function of the weighted Euclidean distance, $\|x(N_i) - x(N_j)\|_{2,a}^2$, where $a > 0$ is the standard deviation of the gaussian kernel. The application of Euclidean distance to the noisy neighborhood raises the following equality.

$$\|x(N_i) - x(N_j)\|_{2,a}^2 = \|y(N_i) - y(N_j)\|_{2,a}^2 + 2\sigma^2$$

This equality shows the robustness of the algorithm since in expectation the Euclidean

distance conserves the order of the similarity between the pixels. Pixels with a similar intensity level neighborhood to $x(N_i)$ have higher weights in the average. These weights are defined as,

$$w(i,j) = \frac{1}{Z(i)} e^{-\frac{\|x(N_i) - x(N_j)\|_{2,a}^2}{h^2}}$$

Where $Z(i)$ is the normalizing constant that ensures $\sum_j w(i,j) = 1$.

$$Z(i) = \sum_j e^{-\frac{\|x(N_i) - x(N_j)\|_{2,a}^2}{h^2}}$$

And h acts as a degree of filtering. It controls the decay of the exponential function and therefore the decay of weights as a function of the Euclidean distances. The NL-means not only compares the intensity level in a single point but the geometrical configuration in a whole neighborhood. This fact allows a more robust comparison than other neighborhood filters.

6.5. *In-vivo* superficial micro-vessels imaging

In order to visualize the superficial micro-vessels in three-dimensional view at the dorsum of the hand *in-vivo* experiments were performed utilizing the proposed imaging framework. The HFUS ultrafast data was acquired via a continuous mechanical scanning at the constant speed of 1 mm/s. The acquired dataset was processed with a proposed approach of section-wise SVD clutter filter and NLM filter to remove the clutter signal and noises respectively. As described in chapter 5, to visualize the cutaneous vascular network, the HFUS ultrafast data was processed with the novel approach of region-based SVD clutter filter instead of global SVD filter. Therefore, in 3D volumetric image processing algorithm, we implemented the section-wise region-based SVD filter to remove the clutter signal and extracts the blood flow signal from different layers of the

skin efficiently, NLM filter to remove the motion noises, and top-hat filter to remove the system generated background noises. The complete signal and image processing algorithm is illustrated in Fig. 6.18 and Fig. 6.19.

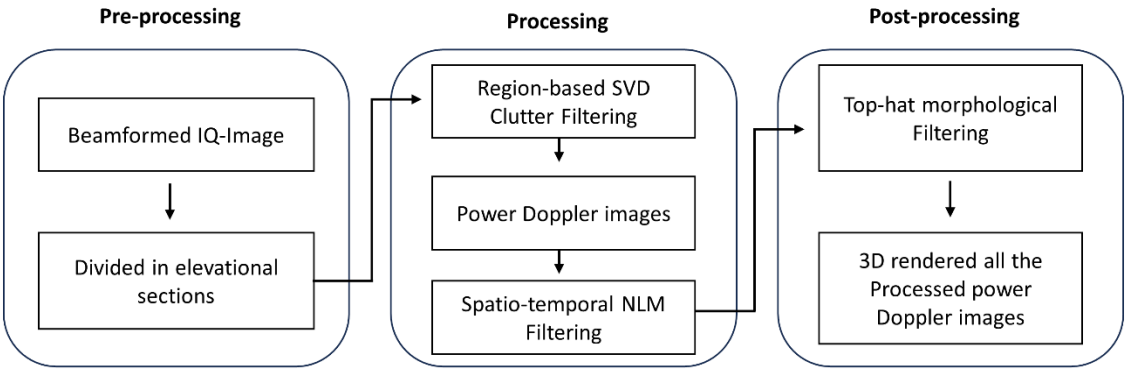

Fig. 6.18. 3D volumetric signal and image processing workflow.

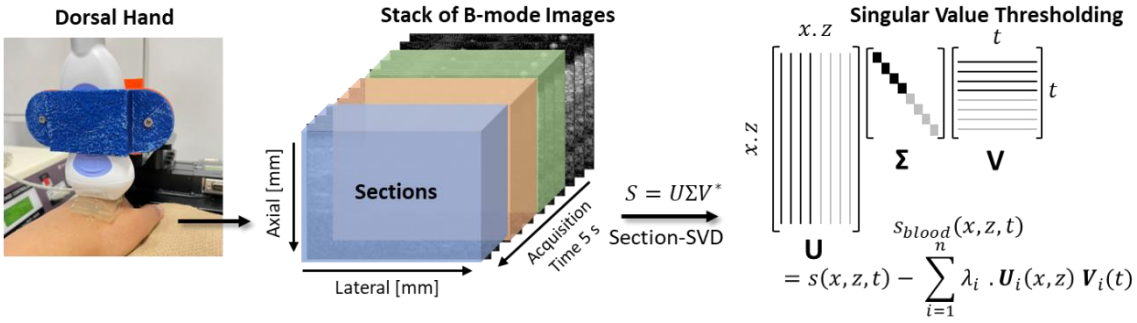

Fig. 6.19. 3D volumetric signal acquisition and processing (*in-vivo*)

6.6. Result

6.6.1. *In-vitro* micro-flow phantom imaging

The cross-sectional (axial – elevational) view of straight micro-flow channel shown in Fig. 6.20 (a) and bifurcated micro-flow channel Fig. 6.21 (a) presents the short-axis view

of each power Doppler image acquired via step-by-step mechanical translation. This cross-sectional view demonstrated the continuity in the flow tract and in detail visualization of micro-structures. The concatenated dataset of all the processed 2D power Doppler images of each step was rendered in MATLAB in-built volume viewer application for 3D realization as shown in Fig. 6.20 (b-c) of straight channel 200 µm flow tract and Fig. 6.21 (b-c) of bifurcated channel 300 µm flow tract.

In addition, to the 3D volumetric imaging performed via step-by step mechanical scanning, a continuous mechanical scanning approach was also implemented to acquire the 3D HFUS ultrafast dataset. Processed power Doppler images revealed that by increasing the transducer translation speed results in increment to interference noises. The section-wise SVD processing of 3D dataset results in the formation of a stack of 2D power Doppler image of each section which highlights the presence of flow signal at explicit location of imaging area. Later each section was processed with NLM filter to remove the translation motion noises as presented in Fig. 6.22 (b)**,** which indicates that the application of the NLM filter effectively mitigates the interference noises resulting from the probe translation. Notably, these noises exhibit a dependency on the transducer speed, as evidenced by the volumetric images shown in Fig. 6.22. Volumetric data acquired at a transducer speed of 1 mm/s Fig. 6.22 (a-b) exhibit fewer noises compared to that obtained at 2 mm/s Fig. 6.22 (c-d). In both instances, the NLM filter effectively eliminates the interference noises leading to a twofold enhancement in image contrast compared to the images without NLM processing as shown in Fig. 6.23

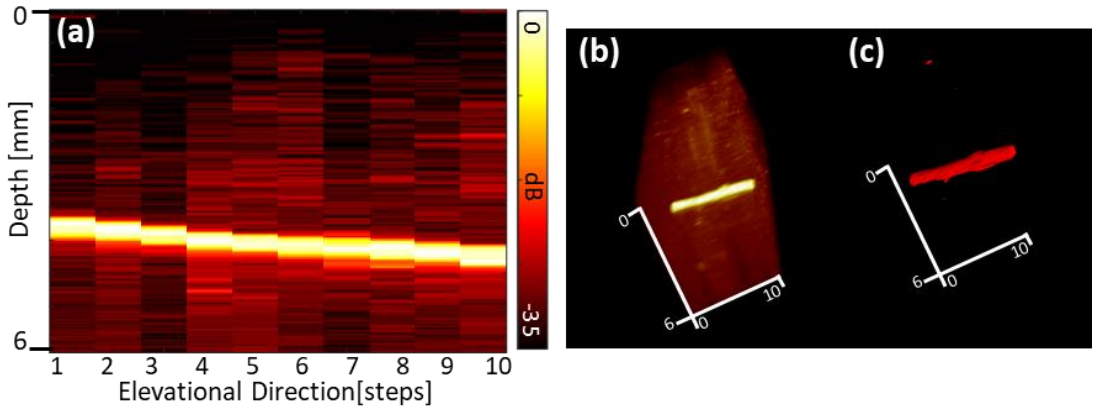

Fig. 6.20. 3D rendered volumetric imaging of 200 µm straight channel micro-flow phantom obtained via step-by-step mechanical translation. (a). Cross-sectional (axial-elevation) view of stacked 2D power Doppler images. (b). Maximum intensity projection of 3D rendered volumetric image. (c). Iso-surface representation of 3D rendered volumetric image.

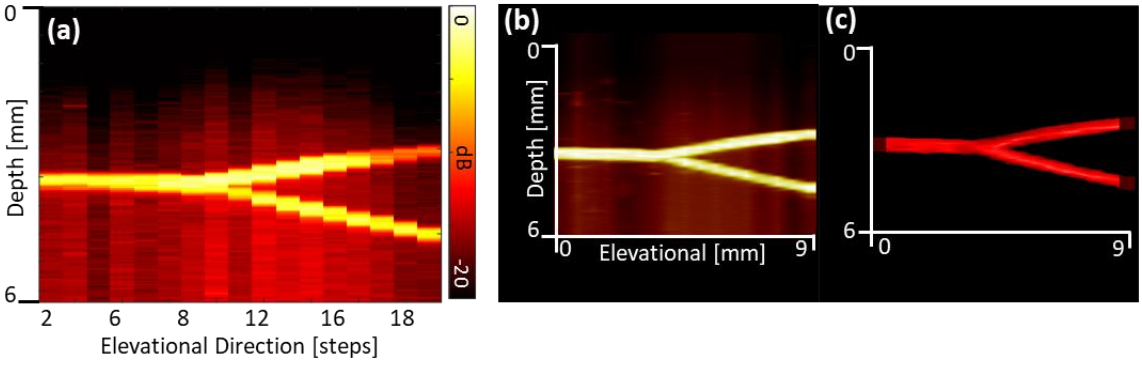

Fig. 6.21. 3D rendered volumetric imaging of 300 µm bifurcated channel micro-flow phantom obtained via step-by-step mechanical translation. (a). Cross-sectional (axial-elevation) view of stacked 2D power Doppler images. (b). Maximum intensity projection of 3D rendered volumetric image. (c). Iso-surface representation of 3D rendered volumetric image.

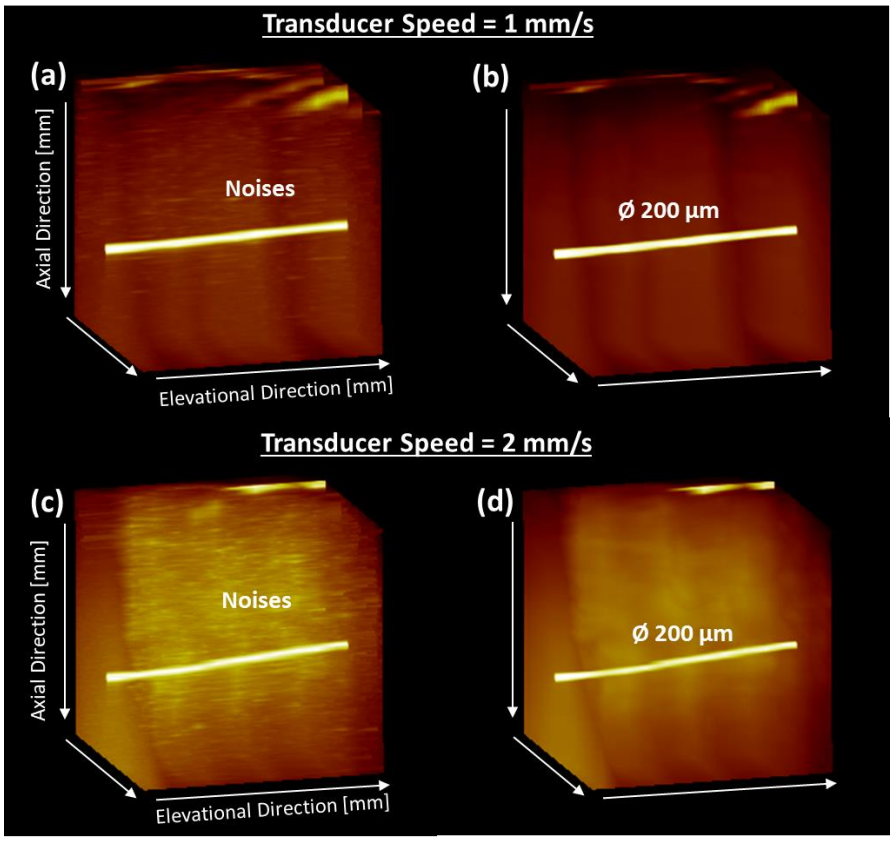

Fig. 6.22. 3D rendered volumetric images of 200 µm flow tract obtained via continuous mechanical translation. (a – b) 3D images obtained with transducer speed of 1 mm/s, (c-d) 3D images obtained with transducer speed of 2 mm/s.

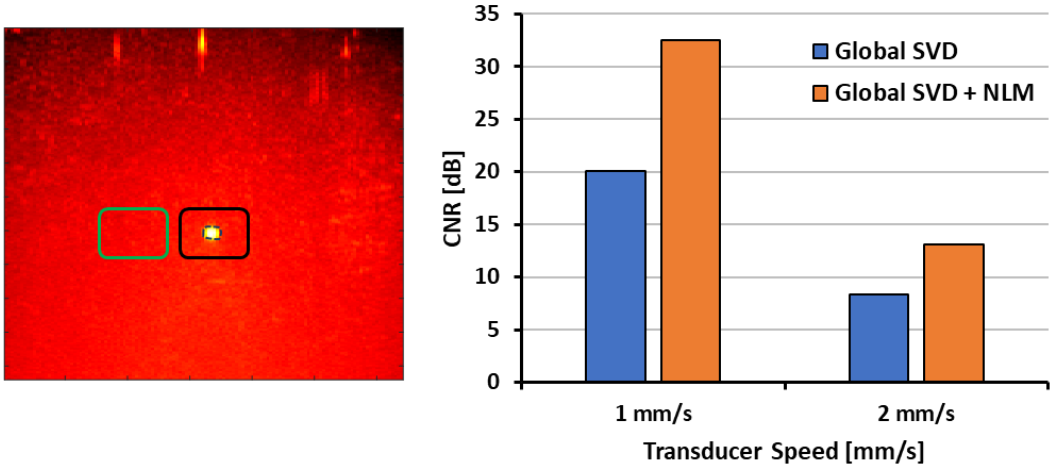

Fig. 6.23. Quantitative comparison of contrast-to-noise ratio among SVD and SVD + NLM under two conditions of transducer speed (1 mm/s and 2 mm/s). Green box indicates noise field, black box is background signal and dashed blue indicates the signal..

Besides, the assessment of 3D volumetric imaging performed via step-by-step and continuous mechanical scanning in qualitative metric. The quantitative measurements was also performed to measure the diameter of the visualized flow tracts. The 3D volumetric image shown in Fig. 6.21 was processed quantitatively to measure the diameter of the bifurcated micro-flow channel visualized in each step-by-step processing. Intensity profiles were obtained from the center position of the flow tract in the short-axis image of each acquired step and the FWHM was measured from each respective power Doppler image. As shown in Fig. 6.24 it was observed that the averaged diameter of the parent branch was measured 278 ± 13.2 µm while the daughter branches 1 and 2 was observed 225 ± 18.6 µm and 247 ± 26.8 µm respectively

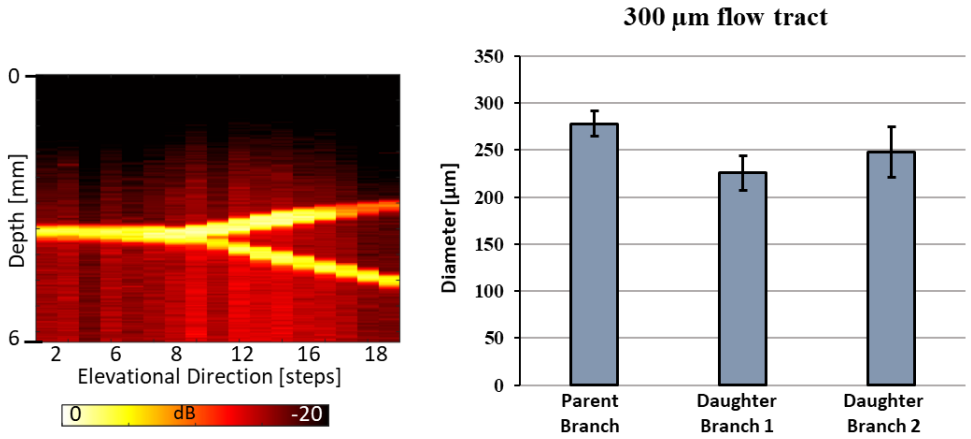

Fig. 6.24. Quantitative measurement of detected diameter of micro-flow tract (300 µm) visualized in 3D volumetric imaging performed via step-by-step mechanical scanning approach

Later, 3D volumetric imaging of straight micro-flow channel performed via continuous mechanical scanning was also quantitatively analyzed. As shown in Fig. 6.25 the diameter of visualized flow tract in each section of the 3D volumetric data was processed. Intensity profiles from each power Doppler images was obtained from the center position of flow tract in the short-axis image and the FWHM was measured. From that analysis it was observed that averaged detected diameter of 193.0 µm with transducer translation speed of 1 mm/s, and 188.75 µm with transducer translation speed of 2 mm/s. These measured values of the micro-flow tract was observed under the flow speed of 20 mm/s in the micro-flow tract of 200 µm in diameter.

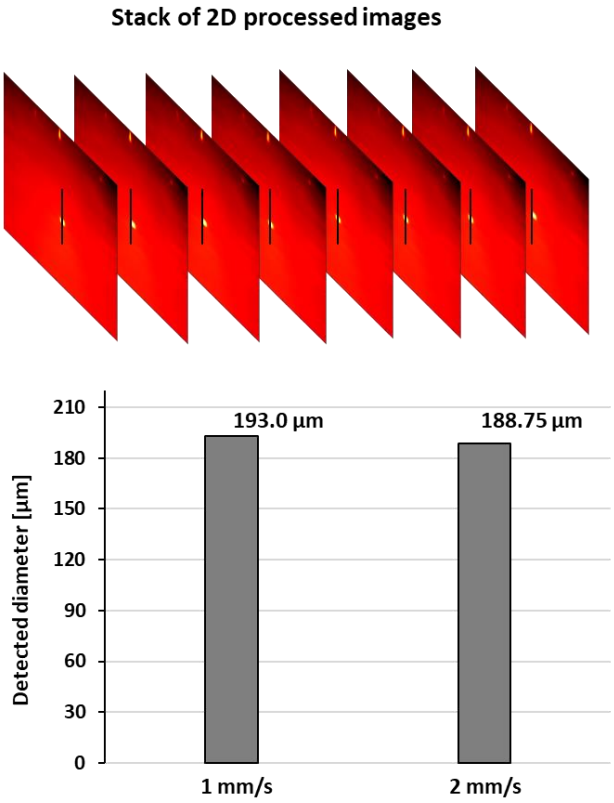

Fig. 6.25. Quantitative measurement of detected diameter of micro-flow tract (200 µm) visualized in 3D volumetric imaging performed via continuous mechanical scanning approach

6.6.2. *In-vivo* superficial micro-vessels imaging

In *in-vivo* superficial micro-vessels imaging, the acquired data from the dorsum of the hand was processed with proposed combined approach of section-wise region-based SVD filter, NLM filter and top-hat transform morphological filter. To visualize the micro-vessels from the acquired *in-vivo* data, it was first divided into the respective sections. Each section was then processed with proposed 3D volumetric image processing workflow shown in Fig. 6.18. From the obtained SVD filtered signal, the power Doppler images were generated from each respective section. Resultantly the vasculatures were clearly visualized in the subcutaneous layer of the skin in the obtained power Doppler images. However, the strong noises appeared as speckles remain persistant in the SVD

processed power Doppler images. These noises were caused by the motion of the transducer translation in continous mechanical scanning which results in acquition of distorted signal in between the acquisition frames. That distorted signal emerge as speckle noise with different pixel intensity values in the SVD processed power Doppler images. To prevail over such noises, non-local means (NLM) filter was implemented to smoothed the fluctuated intensity values in the image by computing the denoised values based on the pixel's similarity comparison. As a result, the fluctuated intensities of pixels becomes denoised and uniform across the image, causing the reduction in the speckle noises. In the final step of processing, the background system generated noises were suppressed by the implementation of the top-hat transform morphological filter as elaborated in Chapter 4. Quantitatively, in section-wise SVD procressing, the image contrast and the visibility of superficial micro-vessels in the dermis layer of the skin was improved with region-based SVD filtering in comprison to the global approach. It happened due to the fact, that flow siganl of smaller vessels in the deeper layer of skin overlayed the slowest flow signal of superficial micro-vessels in the dermis layer of the skin during singilar value thresholding in global approch of SVD. Region-based filtering extracts the flow signal from respective layers of the skin at different cut-off values based on local signal statistics in respective layers of the skin enhances the visibility of micro-vessels and the image contrast. Application of NLM filter reduces the speckle noises and normalize the image intensity while preserving the vascular signal. The remianing background noises were suppressed with the application of top-hat filter which retains the ability to suppress the background noises, and highlights the vasculatures visibility as shown in Fig 6.26.

Once each section is processed with the 3D image processing workflow presented in Fig.6.18, stack of 2D processed power Doppler images were concatenated into a single 3D volume and rendered in MATLAB in-built 3D volume viewer. The representation of volume was observed in slice-view and volume-view of the 3D viewer as presented in Fig 6.27 and Fig. 6.28 respectively. Vasculature's signal was observed in respective slices (axial, lateral and elevational) of 3D volume to locate the presence of micro-vessels and smaller vesselss in the depth depenedent layers of the skin. Furthermore, in maximum intensity projection (MIP) representation of 3D volume, the vasulatures were clearly observed in superficial dermis layer and deep layer as indicated by green circles in Fig.

6.28. It was also observed that due to poor elevational resolution, the visibility of micro-vessels in the elevational direction was forfeited, while the deeper smaller vessels were visualized clearly in Fig. 6.28.

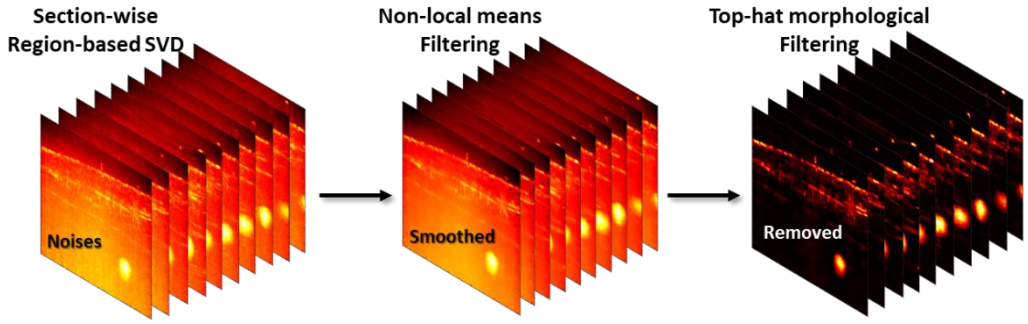

Fig. 6.26. Stack of 2D power Doppler images processed with section-wise SVD, NLM and top-hat morphological filter.

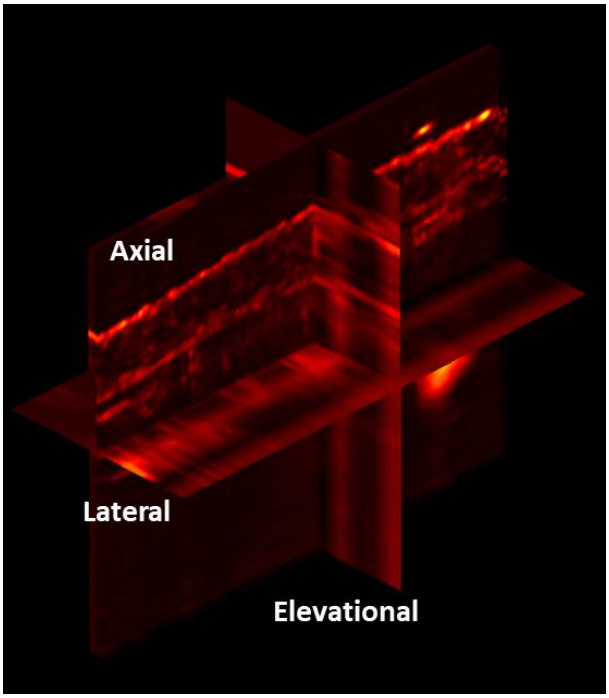

Fig. 6.27. Slice view of 3D volume in MATLAB in-built volume viewer.

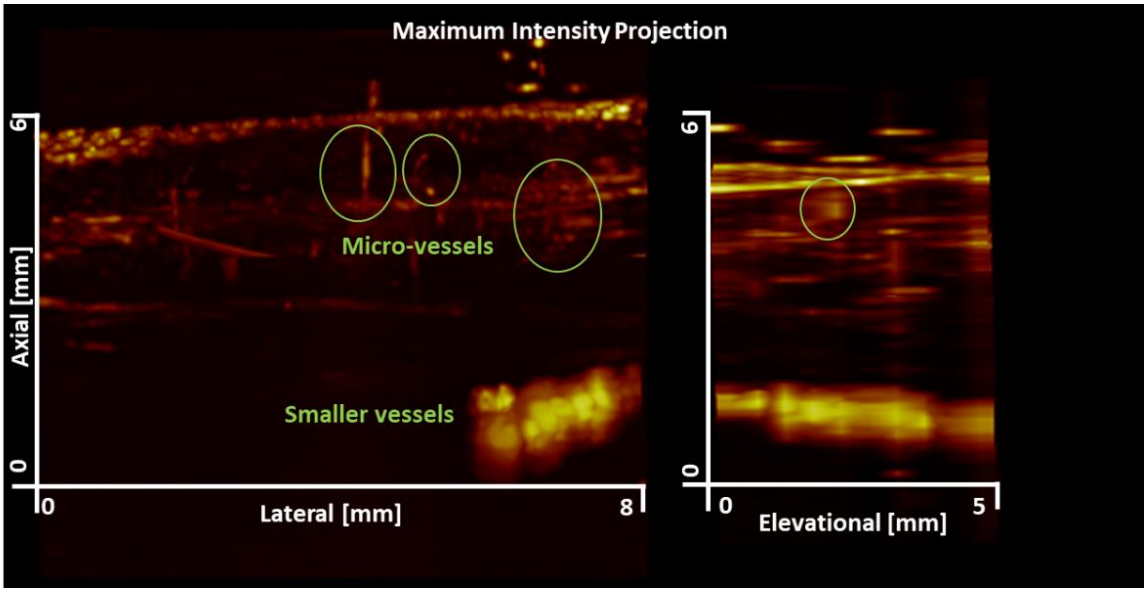

Fig. 6.28. Volumetric view of 3D volume (Maximum intensity Projection) in MATLAB in-built volume viewer.

Further trial experiments were also performed to observe the reproducibility and resolvability of the proposed 3D volumetric image processing apporaoch. The data was obtained from different locations on the dorsum of the hand using HFUS 3D volumetric imaging with continuous scanning approach. The acquired datasets were then processed with the proposed 3D volumetric image processing workflow illustrated in Fig. 6.18. Each processed data was then represented in MATLAB in-built volume viewer revealing the visualization of superficial vasculatures in three-duimensional view. As shown in Fig. 6.29 (Trial 2) and 6.30 (Trial 3), the superficial micro-vessels and deeper smaller vessels were visualized at different depth position. The visibility of micro-vessles were clearly obserevd in the dermis layer of skin at the dept h of 2-3 mm while the smaller vessels were observed in the deeper layer of subcutaneous tissue at the depth of 3-4 mm. Additionally, it was observed in Fig. 6.30 that the superficial epidermal tissue signal was very strong in the processed power Doppler images.

To understand the characteristics of observed epidermal noisy tissue signal in SVD decomposed matrices, the singular value thresolding was performed at different cut-off values as shown in Fig. 6.31. The purpose of this analysis was to observe the intensity and the effect of epidermal tissue on flow signal of vasculatures in singular values. As presented in the singular value decay graph shown in Fig. 6.31, the possibility of the presence of the tissue signal and the flow signal lies in the higher and middle singular

values respectively ranging from 1 – 90 singular values. The filtering was performed at different cut-off values (10, 40, 60, and 80) of singular values as shown in Fig. 6.31. From this analysis it was observed that the intentisy of superficial epidermal tissue signal was quite high and remain persisitant in all the higher and middle singualr values.

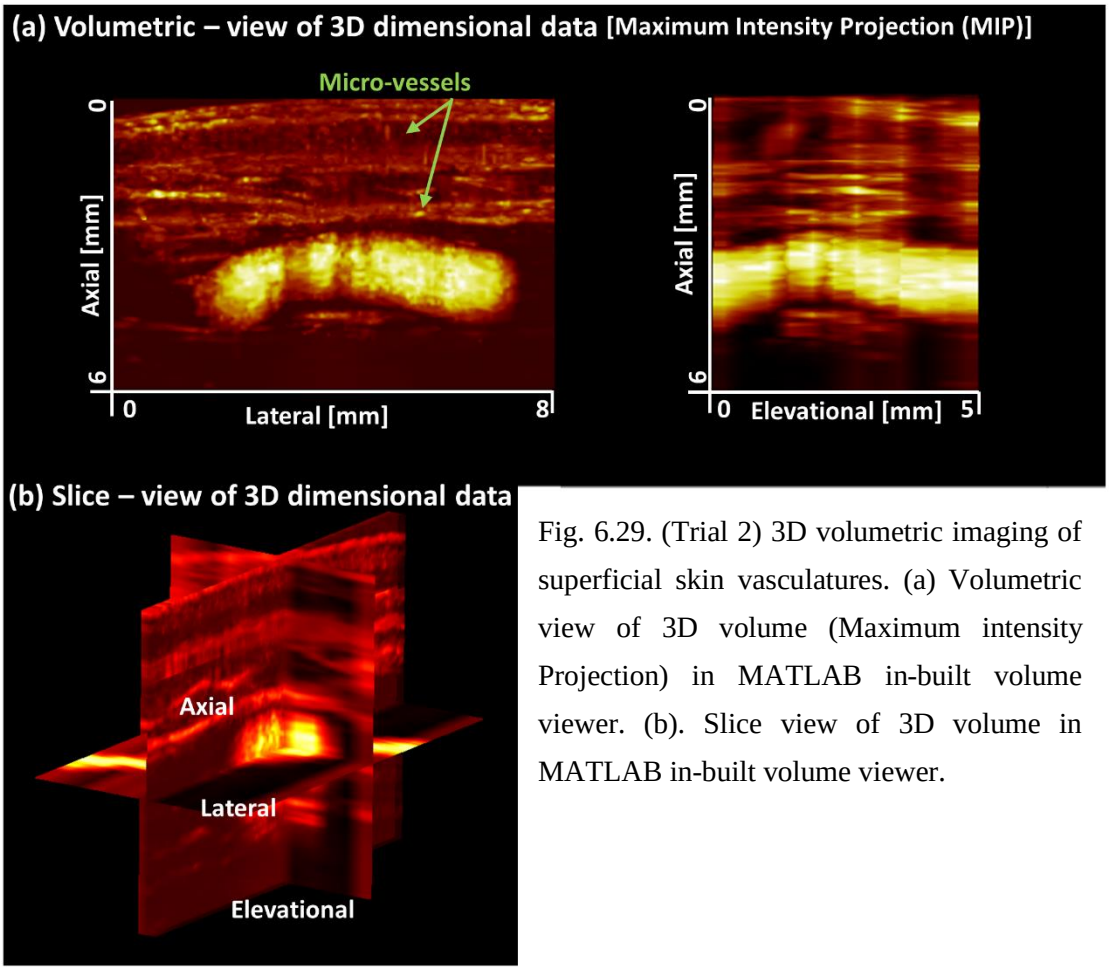

Fig. 6.29. (Trial 2) 3D volumetric imaging of superficial skin vasculatures. (a) Volumetric view of 3D volume (Maximum intensity Projection) in MATLAB in-built volume viewer. (b). Slice view of 3D volume in MATLAB in-built volume viewer.

To tackle the challenges posed by epidermal tissue signals that affects the visbitly of vasculatures, an epidermal removal approcah was implemented by turncating the HFUS beamformed data retaining the erpidermal layer from B-mode images of 3D volumetric dataset. Later it was processed with the proposed 3D volumetric image processsing workflow (Fig. 6.18). After truncating the superficial epidermal tissue layer, it was obsereved that the strong high intensity layer was removed from the processed power Doppler images as depicted in Fig. 6.32, resultantly enhances the visibility of the superficial micro-vessels and as well as the deeper vasculatures.

Quantitatively, the diameter of the visualized superficial micro-vessels was also measured by calculating the full-width half maximum from the obtained intensity profiles shown in Fig. 6.33. A single slice from the stack of 2D porcessed power Doppler images was chosen, and three different micro-vessels was taken to obtain the intensity profiles as indicated by respective colors in the single sliced power Doppler image. The detected diameter of the visualized superficial micro-vessels was observed in the range of 141 – 153 μm in diameter in correspondance to the diameter of dermal vasculatures (100 – 200 μm).

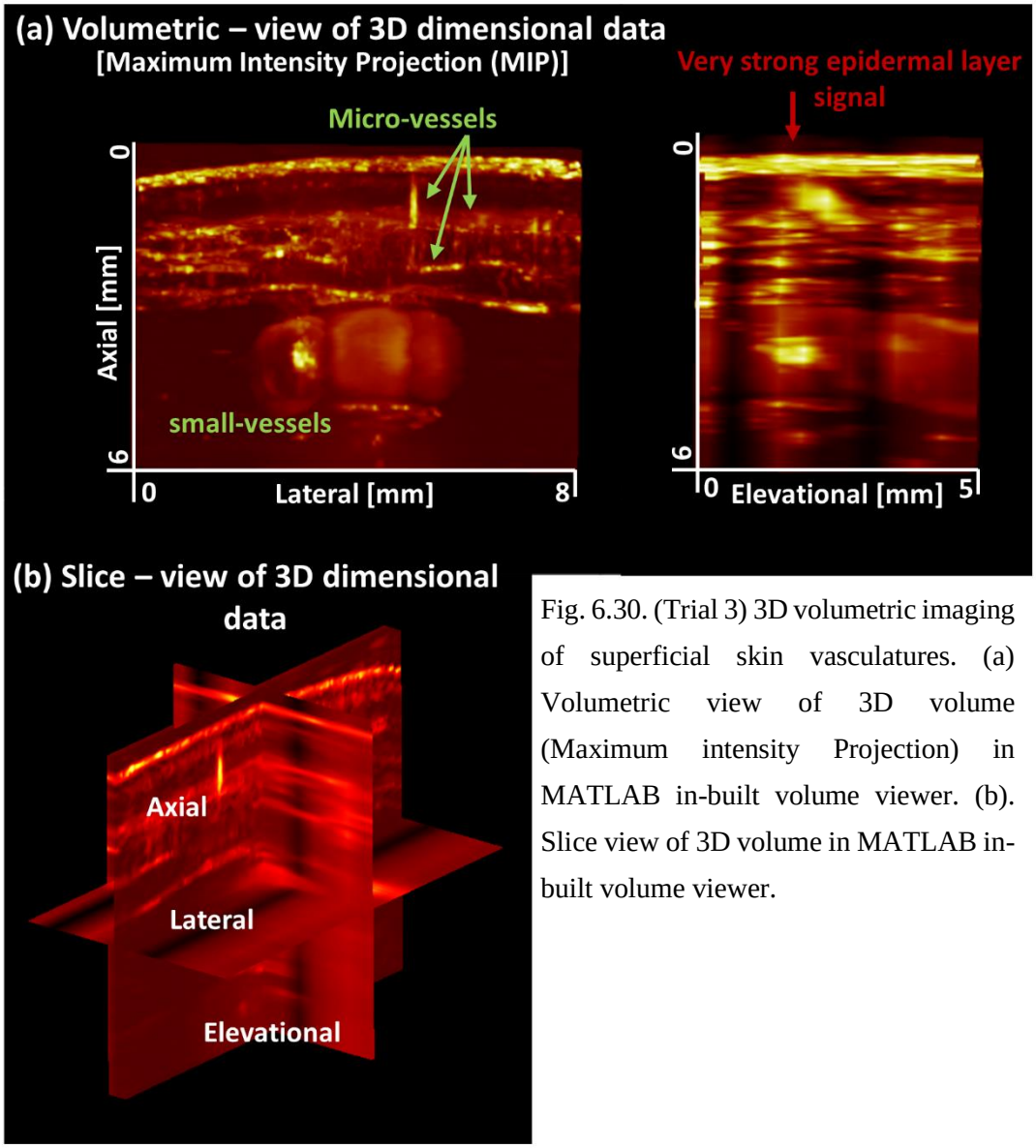

Fig. 6.30. (Trial 3) 3D volumetric imaging of superficial skin vasculatures. (a) Volumetric view of 3D volume (Maximum intensity Projection) in MATLAB in-built volume viewer. (b). Slice view of 3D volume in MATLAB in-built volume viewer.

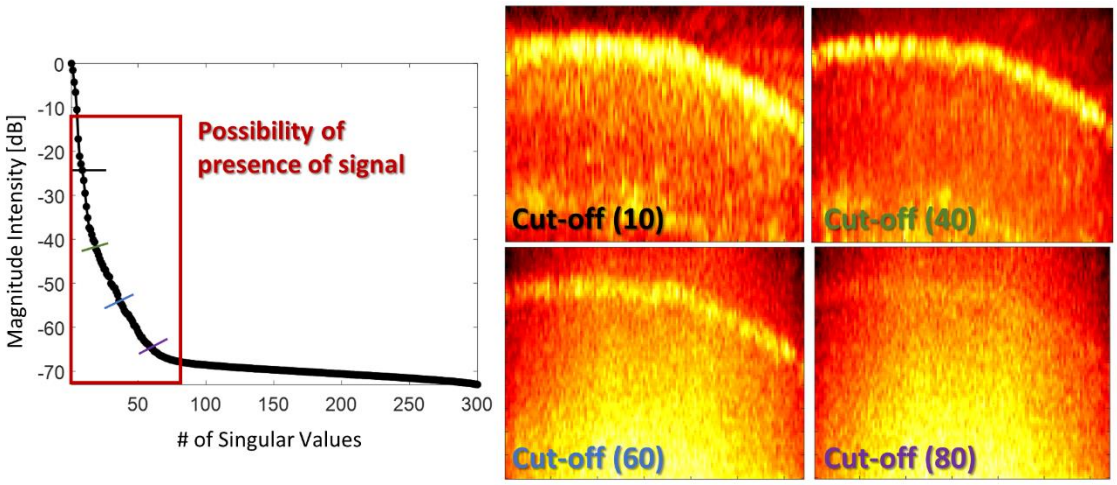

Fig. 6.31. Singular value thresholding at different cut-off values to observe the intensity of superficial epidermal tissue.

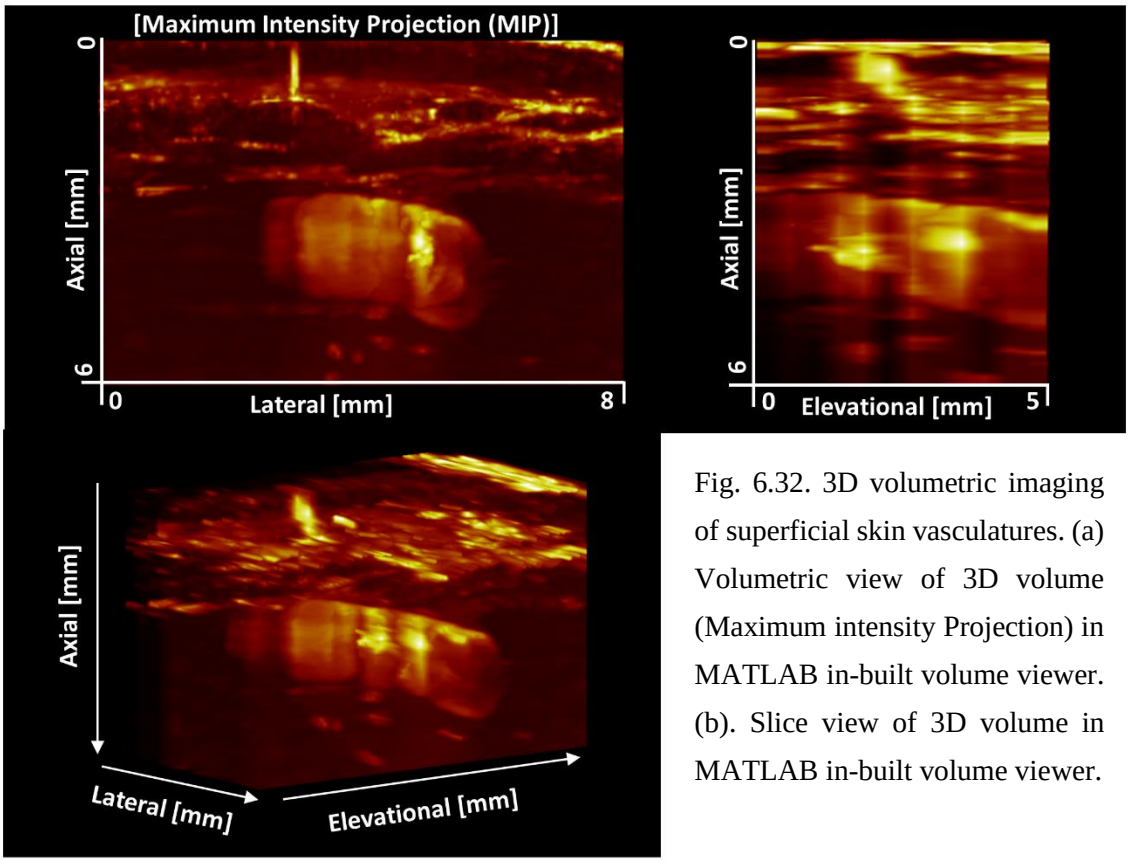

Fig. 6.32. 3D volumetric imaging of superficial skin vasculatures. (a) Volumetric view of 3D volume (Maximum intensity Projection) in MATLAB in-built volume viewer. (b). Slice view of 3D volume in MATLAB in-built volume viewer.

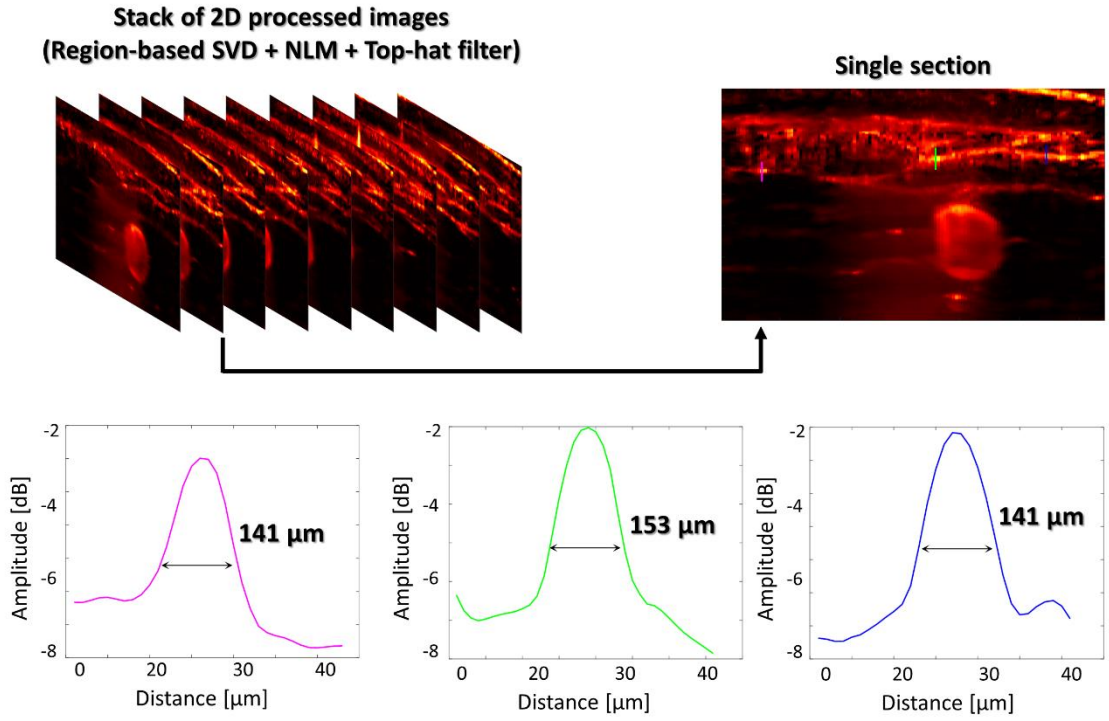

Fig. 6.33. Quantitative measurements of detected diameter of micro-vessels in the dermis layer of skin

Furthermore, the image contrast was also evaluated among the region-based SVD clutter filtering and global SVD clutter filtering in the 3D volumetric processing workflow. Quantitative metric of contrast to noise ratio (CNR) was calculated from respective power Doppler images processed with each filter of the proposed algorithm. From that analysis it was observed that the image quality in terms of CNR was increased from SVD to NLM to top-hat filtering. However, in comparison to the implementation of global SVD, image contrast was slightly improved with the processing of data with section-wise region-based SVD, NLM and top hat morphological filter as illustrated in Fig. 6.34.

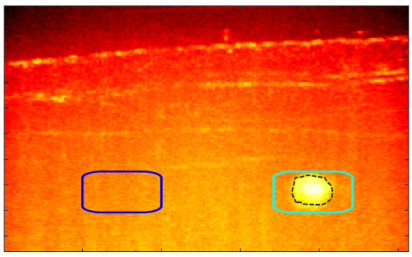

$$CNR = \frac{\mu_{blood} - \mu_{background}}{\sigma_{noise}}$$

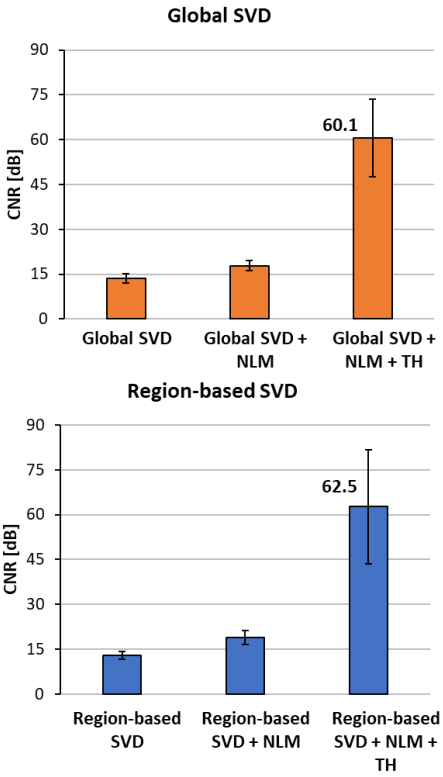

Fig. 6.34. Quantitative analysis on the metric of CNR among section-wise global SVD, NLM and top-hat filter and section-wise region-based SVD, NLM and top-hat filter approach. Blue and sky blue solid line boxes represent the ROI for background signal and noises respectively, while the blue dashed lines indicate the blood signal in micro-vessels in all respective images.

6.7. Discussion

In this chapter, we presented a 3D volumetric imaging of superficial vasculatures incorporating the high-frequency ultrafast ultrasound, continous mechanical translation, SVD based spatio-temporal cluter filtering and implementation of denoising filters such as top-hat transform and non-local means fitlering. The performance of the proposed framework was evaluated in 3D *in-vitro* micro-phantom experiments and *in-vivo* 3D volumetric imaging of superficial vasculatures of skin.

In the phantom experiments, both approaches of 3D mechanical (step-by-step and continuous) scanning has been performed to observe the phenomenon of 3D volumetric imaging in visualization of superficial vasculatures. In step-by-step mechanical scanning

approach, the image quality is higher at the trade-off of acquisition time and asynchronous data acquisition. On the other hand, with the approach of continuous mechanical scanning approach, the acquisition time is significantly decreased due to utilization of single transmission event in the acquisition of 3D data with benefit of synchronous acquisition of signal. In comparison to the step-by-step mechanical scanning approach, the continuous mechanical scanning approach is faster. However, the later approach faces the challenges to maintain the image quality. The power Doppler imaging utilizing HFUS ultrafast ultrasound and SVD clutter filtering using step-by-step mechanical scanning approach has higher image quality, which was significantly degraded via the continuous mechanical scanning approach, because the later approach faces the challenge of transducer translation motion which causes an additional interference noises between the tissue signal and the blood flow signal. Fig. 6.13 suggests that setting a lower translation speed supports the better separation between smaller shifted Doppler signal of tissue clutter aroused from the transducer translation and the Doppler signal of the flow signal. To overcome with such translation noises, we implemented an advanced and efficient 3D volumetric image processing algorithm which comprised on section-wise SVD clutter filtering which extracts the signal from each location efficiently and NLM filter which reduces the translation noises and enhances the image contrast.

Apart from the transducer translating speed, other important parameter which impacts the imaging quality in 3D imaging is the imaging depth and elevational resolution. The signals originated from the elevational focal depth, which is around 8 mm of L38-22v linear array transducer where the elevational slice thickness was observed the smallest. This slice thickness is larger when imaging at the deeper or the more superficial depth. The elevational profile not only determines the image resolution in the elevational dimension but also affects the overall Doppler image quality for the presented approach of section-wise SVD processing of 3D volumetric data. As the section's thickness and the number of frames in each section was chosen based on the maximum and minimum values of measured elevational resolution which was observed from different depth positions as shown in Fig 6.3. Further to observe the characteristics and affect of elevational resolution on image quality, we performed the experiment by changing the position of micro-phantom from straight to tilt position as shown in Fig. 6.35. When the continuous mechanical scanning was performed by placing the micro-channel phantom in perpendicular to the transducer beam, the flow channel and the ultrasonic beam position was also perpendicular, resulting the affect of elevational resolution on the micro-structure was minimum. On the other hand, when the micro-phantom was in tilted

positioned, the direction of ultrasonic beam and micro-structures was not perpendicular. The 3D volumetric scanning in straight direction, the straight micro-structure was affected with the elevational profile of the beam due to the tilting position of the phantom. From this experiment, it was observed qualitatively (Fig. 6.36) and quantitatively (Fig. 6.37) that imaging the straight superficial micro-channels from other dimensions, the elevational resolution affects the image quality. As shown in Fig. 6.36, the diameter of the visualized micro-structure in 3D rendered volumetric image obtained under tilted position was observed thicker with detected diameter of 277 μm (Fig. 6.37) in comparison to the one with observed diameter of 193 μm imaged without tilting conditions.

The most prominent advantage of the proposed approach compared to the existing 3D volumetric imaging approaches, is that it enables the power Doppler imaging of a large imaging volume in a shorter acquisition time with less computational costs with a trade-off of lower image quality. Implementation of the proposed 3D volumetric image processing algorithm comprised on section-wise region-based SVD clutter filtering and post-processing filters such as non-local means and top hat transforms truncates the clutter signal, interference noises and background noises respectively and enhanced the image quality and visibility of micro-vessels. It was observed that these translation noises become more prominent as the translation speed becomes faster. It can be explained by the dominating interference brought by speckle and tissue motion from the surrounding tissues. But the proposed approach significantly reduces the noises and enhances the image quality and visibility of micro-structures in 3D volumetric realization.

Impact of translation noises was also investigated in the pre-compounded frames of HFUS ultrafast data acquired via continuous mechanical scanning approach under different transducer translation speed as shown in Fig 6.15. From that analysis it was found that each individual pre-compounded frame covered a minimum distance of 0.2 μm which was considered negligible to causes an interference noises.

In the proposed approach of 3D image processing algorithm, the parameters such as section thickness and degree of NLM filtering was chosen to maintain the Doppler sensitivity and the quality of image respectively. The combined processing of section-wise region-based SVD processing, non-local means and top-hat filtering has shown its performance in *in-vitro* phantom experiments and *in-vivo* superficial skin vascular visualization. The realization of superficial micro-vessels in the dermis layer and smaller vessels in the deeper layers of the skin in 3D volumetric images in Fig. 6.28 highlights the potential of the proposed 3D volumetric imaging framework. We anticipate that the proposed approach of 3D volumetric imaging of superficial vasculatures has bring new

insights in the visualization of skin vascular networks and assist in the diagnosis and prognosis of various cutaneous disorders.

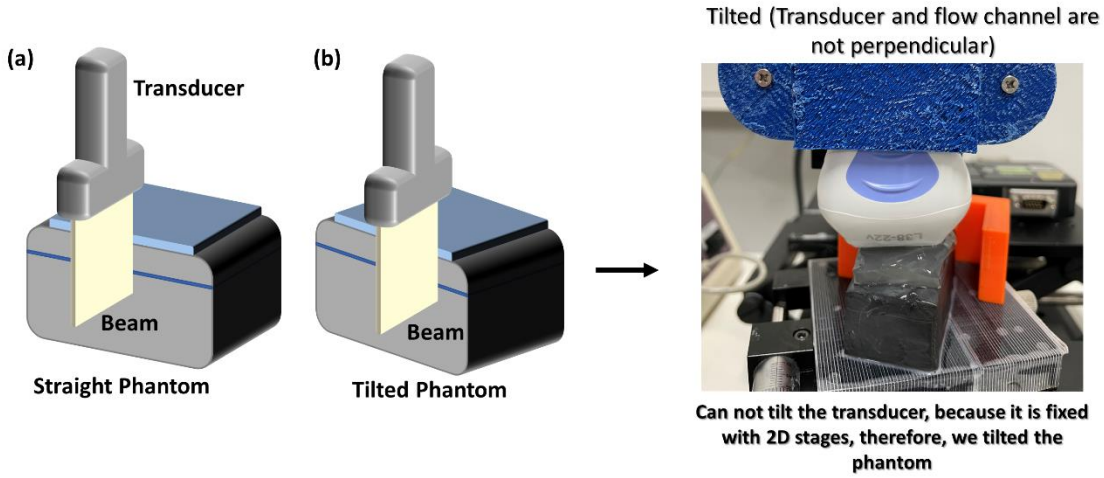

Fig. 6.35. Experimental setup to perform 3D volumetric imaging on (a) micro-phantom positioned in straight direction, (b) micro-phantom positioned in tilted direction.

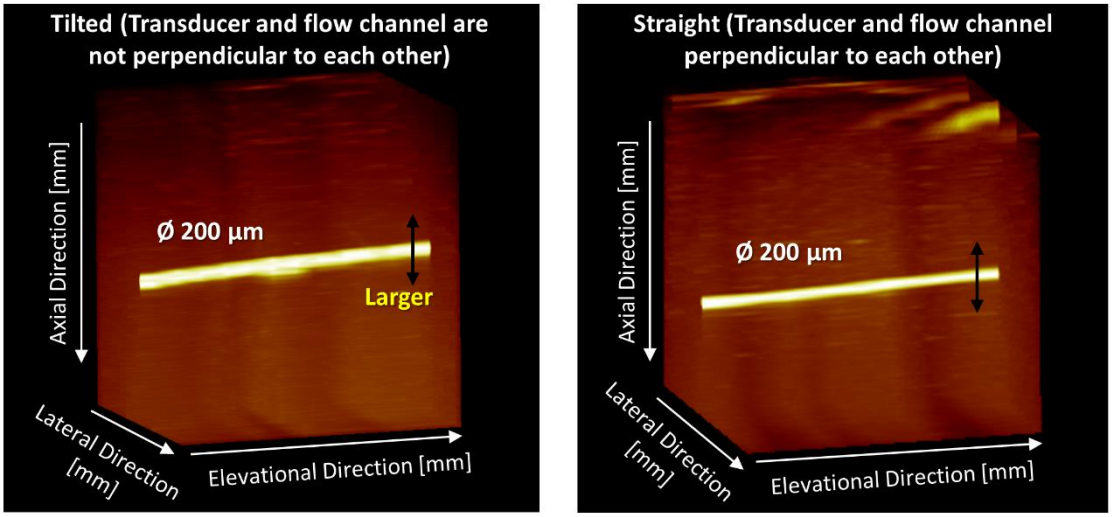

Fig. 6.36. Quantitative observation of micro-flow phantom in 3D volumetric imaging under experimental conditions of straight positioned micro-phantom and tilted positioned micro-phantom.

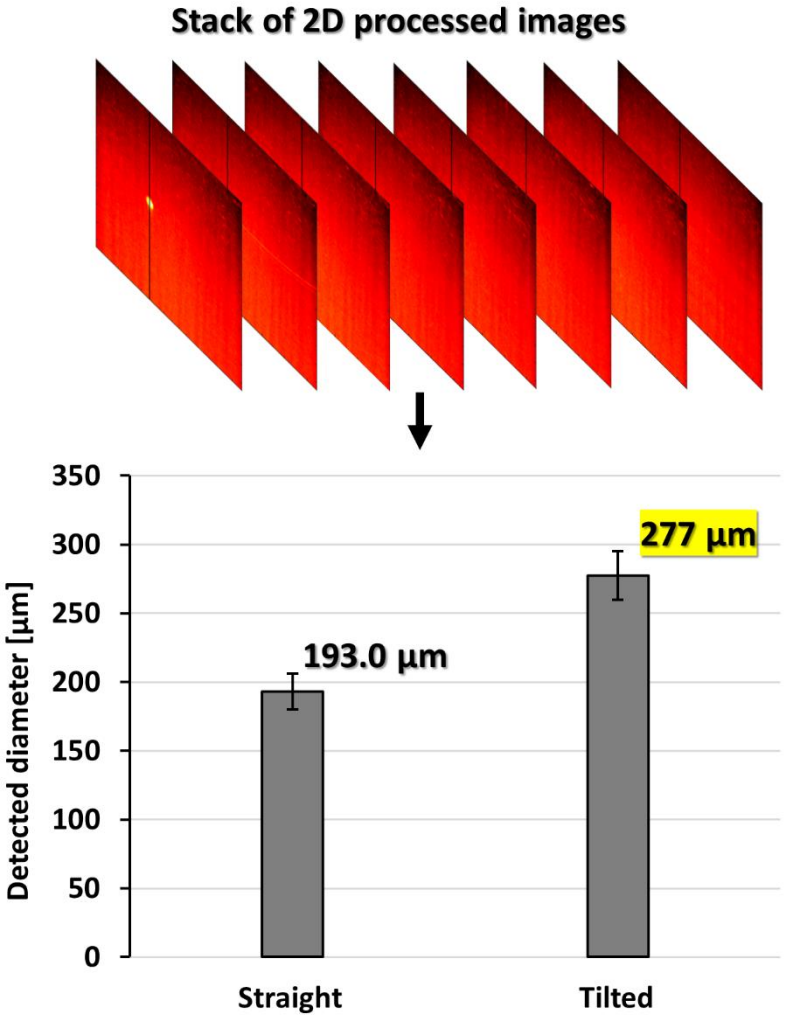

Fig. 6.37. Quantitative comparison in detected diameter of micro-flow phantom under experimental conditions of straight positioned micro-phantom and tilted positioned micro-phantom.

Chapter 7
Conclusion and Future perspectives

7.1. Conclusion

Considering skin as the superficial and the largest organ of human body, it is subjected to various diseases and abnormalities. Dysfunctionality in vasculatures of skin in response to any disease or pathology strongly affects the patients' health and daily life activities. Such as in cases of "Raynaud's phenomenon", "vasculitis" and "melanoma" these diseases are caused by the narrowing of vasculatures, remodeling of vasculatures and the formation of new vasculatures respectively. The earlier the diagnosis, the better the patient can be treated, and the fewer the consequences will be. Doppler techniques of ultrasound is one of the most utilized approaches in observation of the blood flow dynamics in vasculatures. In context of skin imaging, structures of skin layers and morphology has been examined with high-frequency (HFUS) ultrasound due to its good resolution and in-depth penetration. However, the conventional techniques of HFUS lacks the Doppler sensitivity to locate the blood flow signal of cutaneous superficial vasculatures in skin Doppler imaging. Also, the cutaneous vascular network comprised on very superficial micro-vessels and superficial smaller vessels. Mapping of very slow flow signal with conventional Doppler ultrasound approaches is cumbersome due to its limited Doppler sensitivity. To locate the flow signal of a very superficial micro-vessels, highly sensitive Doppler techniques need to be implemented such as ultrafast Doppler imaging. This techniques retains the ability to locate the blood flow signal under wide range of flow velocities due to its higher temporal resolution. Besides, the cutaneous vasculatures are characterized by complex tortuous and branched structures appears in surrounding of diseased tissue. Imaging of these complex vascular structures in two-dimensional imaging is difficult due to their anastomose structures in single imaging plane. Therefore, in this dissertation, I have decided to devised an imaging framework which is capable enough to visualize the cutaneous super superficial vasculatures (micro-vessels at depth of less than 5 mm) and subcutaneous vasculatures (small vessels at depth of 5 mm) in two-dimensional and three-dimensional imaging planes efficiently.

The perspective of this dissertation is to devise an image and signal processing algorithms to locate the micro-flow signal of superficial skin micro-vessels using high-

frequency ultrafast ultrasound imaging. This dissertation is comprised on seven chapters. First, the background and significance of the study has been described, later an overview of the devised HFUS imaging framework including the designing and fabrication of novel micro-flow phantoms have been proposed and validated. Then, a novel clutter filter has been proposed and evaluated in extraction of the blood flow signal from a very superficial (micro-vessels) and superficial (small vessels) vasculatures of skin in two-dimensional imaging of cutaneous vasculatures. Later, that 2D imaging approach has been extended to three-dimensional and proposed an efficient 3D volumetric data acquisition and processing workflow to visualize the superficial vasculatures in multi-dimensional view.

To achieve the goal of the thesis, the devised HFUS imaging framework was validated in *in-vitro* micro-phantom experiments at center frequency of 30 MHz instead of ultra-higher frequency of 40 MHz. Two wall-less superficial micro-flow phantoms of different dimensions and geometries have been proposed with novel designing and fabrication protocols to validate and optimize the imaging sequences. Even in the literature, no such method for fabrication of superficial micro-flow phantom was reported earlier. HFUS ultrafast Doppler imaging experiments were conducted utilizing the developed phantoms to evaluate the performance of the proposed image and signal processing framework in mapping of micro-flow signal under different experimental conditions of flow velocity. After validating the performance of framework in *in-vitro* phantom experiments, an advanced and novel region-based SVD clutter filter was proposed and evaluated in *in-vivo* superficial cutaneous vasculature imaging. Moreover, the two-dimensional imaging framework extended to three-dimensional, and the comprehensive visualization of cutaneous vasculature has proven the merit of the proposed algorithm. Implementation of section-wise region-based SVD clutter filter and post-processing non-local means and top-hat transform filters greatly removes the clutter signal, motion noises, background noises and enhances the image quality and visibility of micro-vessels.

The overarching aim of this research study is to provide the solution or an imaging framework capable enough to visualize the cutaneous vasculature in two-dimensional and three-dimensional imaging. This research work presents the step-by-step manifestation of imaging framework comprising on optimization of imaging sequences, designing and fabrication of micro-flow phantoms, novel SVD based clutter filters, and an efficient 3D volumetric imaging framework. Encouraging results from two-dimensional and three-dimensional *in-vivo* cutaneous vasculatures visualization has shown the credibility and efficacy of the filtering algorithms. Also, in comparison to the conventional SVD clutter filtering approach such as global SVD, the proposed approaches efficiently removes the

clutter and significantly enhances the image contrast.

The proposed imaging framework has shown its potential in visualization of complete cutaneous vascular network (micro-vessels and smaller vessels) in two-dimensional and three-dimensional imaging efficiently. Based on these promising results, the proposed 2D and 3D HFUS imaging protocols could find huge applications in the imaging of cutaneous vasculatures. Also, due to its feature of comprehensive visualization of vascular network it could facilitate in diagnosis and prognosis of various skin disorders including the Raynaud's phenomenon and skin melanoma.

7.2. Future Perspectives

We successfully developed the 2D and 3D HFUS imaging framework and evaluated its performance in *in-vitro* and *in-vivo* experiments. This time the study is mainly focused on the development of image and signal processing algorithms and its evaluation in *in-vitro* experiments and single subject *in-vivo* trial experiments but in future the proposed approaches could be implemented in clinical trial studies with specified objectives and outcomes. There are certain shortcomings, where the proposed approaches needs to be modified for better signal extraction, denoising and visualization of micro-vasculatures.

1. Two dimensional imaging with the proposed approach of HFUS ultrafast Doppler and region-based SVD clutter would be performed on different subjects to evaluate the resolvability of the proposed framework in visualization of cutaneous vascular networks.
2. In three dimensional volumetric imaging, instead of acquisition of 2500 frames at PRF of 5 kHz, more frames would be acquired at higher PRF which might increase the performance. Also, the post-processing NLM filter has been implemented on spatial data only, could be implemented on spatio-temporal data which might increase the denoising factor and enhances the image contrast and visibility of micro-vessels.

References

1. Deegan, Anthony J., and Ruikang K. Wang. "Microvascular imaging of the skin." Physics in Medicine & Biology 64.7 (2019): 07TR01.

2. Carmeliet, Peter, and Rakesh K. Jain. "Molecular mechanisms and clinical applications of angiogenesis." Nature 473.7347 (2011): 298-307.

3. J.C. Jennette, R.J. Falk, Small-vessel vasculitis, N. Engl. J. Med. 337 (21) (1997) 1512–1523.

4. Schmidt, Wolfgang A., et al. "Color Doppler ultrasonography of hand and finger arteries to differentiate primary from secondary forms of Raynaud's phenomenon." The Journal of rheumatology 35.8 (2008): 1591-1598.

5. Li, Yanyun, et al. "Dual mode reflectance and fluorescence confocal laser scanning microscopy for in vivo imaging melanoma progression in murine skin." Journal of investigative dermatology 125.4 (2005): 798-804.

6. Seth, Divya, et al. "Global burden of skin disease: inequities and innovations." Current dermatology reports 6 (2017): 204-210.

7. Giesey, Rachel Lynn, et al. "The global burden of skin and subcutaneous disease: a longitudinal analysis from the Global Burden of Disease Study from 1990-2017." SKIN The Journal of Cutaneous Medicine 5.2 (2021): 125-136.

8. Karimkhani, Chante, et al. "Global skin disease morbidity and mortality: an update from the global burden of disease study 2013." JAMA dermatology 153.5 (2017): 406-412.

9. Ogata, Dai, et al. "Epidemiology of skin cancer based on Japan's National Cancer Registry 2016–2017." Cancer Science (2023).

10. Hashemi, Ghazaleh, et al. "Melanoma tumour vascularization and tissue-resident endothelial progenitor cells." Cancers 14.17 (2022): 4216.

11. Olsen, Jonas, Jon Holmes, and Gregor BE Jemec. "Advances in optical coherence tomography in dermatology—a review." Journal of biomedical optics 23.4 (2018): 040901-040901.

12. Shahriari, Neda, et al. "In vivo reflectance confocal microscopy image interpretation for the dermatopathologist." Journal of Cutaneous Pathology 45.3 (2018): 187-197.

13. Mäkelä, P. J., et al. "Pretreatment sonographic evaluation of inguinal lymph nodes in patients with vulvar malignancy." Journal of ultrasound in medicine 12.5 (1993): 255-258.

14. Schmid-Wendtner, Monika-Hildegard, and Walter Burgdorf. "Ultrasound scanning in dermatology." Archives of dermatology 141.2 (2005): 217-224.

15. Alexander, Harold, and DL Miller. "Determining skin thickness with pulsed ultrasound." Journal of Investigative Dermatology 72.1 (1979): 17-19.

16. Kumagai, Kazutoshi, et al. "High-resolution ultrasound imaging of human skin in vivo by using three-dimensional ultrasound microscopy." Ultrasound in medicine & biology 38.10 (2012): 1833-1838.

17. Wortsman, Ximena. "Common applications of dermatologic sonography." Journal of Ultrasound in Medicine 31.1 (2012): 97-111.

18. Barcaui, Elisa de Oliveira, et al. "High frequency ultrasound with color Doppler in dermatology." Anais brasileiros de dermatologia 91 (2016): 262-273.

19. Szabo, Thomas L. Diagnostic ultrasound imaging: inside out. Academic press, 2004.

20. Bercoff, Jeremy, et al. "Ultrafast compound Doppler imaging: Providing full blood flow characterization." IEEE transactions on ultrasonics, ferroelectrics, and frequency control 58.1 (2011): 134-147.

21. Tanter, Mickael, and Mathias Fink. "Ultrafast imaging in biomedical ultrasound." IEEE transactions on ultrasonics, ferroelectrics, and frequency control 61.1 (2014): 102-119.

22. Montaldo, Gabriel, et al. "Coherent plane-wave compounding for very high frame rate ultrasonography and transient elastography." IEEE transactions on ultrasonics, ferroelectrics, and frequency control 56.3 (2009): 489-506.

23. Denarie, Bastien, et al. "Coherent plane wave compounding for very high frame rate ultrasonography of rapidly moving targets." IEEE transactions on medical imaging 32.7 (2013): 1265-1276.

24. Demené, Charlie, et al. "Spatiotemporal clutter filtering of ultrafast ultrasound data highly increases Doppler and fUltrasound sensitivity." IEEE transactions on medical imaging 34.11 (2015): 2271-2285.

25. Macé E, Montaldo G, Cohen I, Baulac M, Fink M, Tanter M. Functional ultrasound imaging of the brain. Nature methods. 2011 Aug;8(8):662-4.

26. Song, Pengfei, et al. "Noise equalization for ultrafast plane wave microvessel imaging." IEEE transactions on ultrasonics, ferroelectrics, and frequency control 64.11 (2017): 1776-1781.

27. Chen, Pei-Yu, Yuan-Yu Hsueh, and Chih-Chung Huang. "In vivo microcirculation mapping of human skin keloid by 40-MHz ultrafast ultrasound imaging." 2017 IEEE International Ultrasonics Symposium (IUS). IEEE, 2017.

28. Chang, Chao-Chuan, et al. "In vivo visualization of vasculature in adult zebrafish by using high-frequency ultrafast ultrasound imaging." IEEE Transactions on Biomedical Engineering 66.6 (2018): 1742-1751.

29. Li, Hsin-Che, et al. "In vivo visualization of brain vasculature in Alzheimer's disease mice by high-frequency micro-doppler imaging." IEEE Transactions on Biomedical Engineering 66.12 (2019): 3393-3401.

30. Song, Pengfei, et al. "Ultrasound small vessel imaging with block-wise adaptive local clutter filtering." IEEE transactions on medical imaging 36.1 (2016): 251-262.

31. Ternifi, Redouane, et al. "Ultrasound high-definition microvasculature imaging with novel quantitative biomarkers improves breast cancer detection accuracy." European radiology 32.11 (2022): 7448-7462.

32. Kurti, Melisa, et al. "Quantitative biomarkers derived from a novel contrast-free ultrasound high-definition microvessel imaging for distinguishing thyroid nodules." Cancers 15.6 (2023): 1888.

33. Bhatta, Anil Kumar, Uma Keyal, and Yeqiang Liu. "Application of high frequency ultrasound in dermatology." Discovery medicine 26.145 (2018): 237-242.

34. Ng, Alexander, and Justiaan Swanevelder. "Resolution in ultrasound imaging." Continuing Education in Anaesthesia, Critical Care & Pain 11.5 (2011): 186-192.

35. Bjærum, Steinar, Hans Torp, and Kjell Kristoffersen. "Clutter filter design for ultrasound color flow imaging." IEEE transactions on ultrasonics, ferroelectrics, and frequency control 49.2 (2002): 204-216.

36. Heimdal, Andreas, and Hans Torp. "Ultrasound Doppler measurements of low velocity blood flow: Limitations due to clutter signals from vibrating muscles." IEEE transactions on ultrasonics, ferroelectrics, and frequency control 44.4 (1997): 873-881.

37. Jin, Zhan-Qiang, et al. "Color Doppler ultrasound in diagnosis and assessment of carotid body tumors: Comparison with computed tomography angiography." Ultrasound in Medicine & Biology 42.9 (2016): 2106-2113.

38. Jensen, Jørgen Arendt. "Stationary echo canceling in velocity estimation by time-domain cross-correlation." IEEE transactions on medical imaging 12.3 (1993): 471-477.

39. Hoeks, A. P. G., et al. "An efficient algorithm to remove low frequency Doppler signals in digital Doppler systems." Ultrasonic imaging 13.2 (1991): 135-144.

40. Kadi, Anthony P., and Thanasis Loupas. "On the performance of regression and step-initialized IIR clutter filters for color Doppler systems in diagnostic medical ultrasound." IEEE transactions on ultrasonics, ferroelectrics, and frequency control 42.5 (1995): 927-937.

41. Alfred, C. H., and Lasse Lovstakken. "Eigen-based clutter filter design for ultrasound color flow imaging: A review." IEEE transactions on ultrasonics, ferroelectrics, and frequency control 57.5 (2010): 1096-1111.

42. You, Wei, and Yuanyuan Wang. "Adaptive clutter rejection for ultrasound color flow imaging based on recursive eigendecomposition." IEEE transactions on ultrasonics, ferroelectrics, and frequency control 56.10 (2009): 2217-2231.

43. Song, Fuxian, Dong Zhang, and Xiufen Gong. "Performance evaluation of eigendecomposition-based adaptive clutter filter for color flow imaging." Ultrasonics 44 (2006): e67-e71.

44. Kaczkowski, Peter. "Bandwidth sampling data acquisition with the Vantage system for high frequency transducers." Verasonics White Pap (2016): 1-5.

45. Bhatti, A., T. Ishii, and Y. Saijo. "A Micro-flow Phantom for Superficial Micro-vasculature Imaging." Journal of Physics: Conference Series. Vol. 2071. No. 1. IOP Publishing, 2021.

46. Ledoux, Léon AF, Peter J. Brands, and Arnold PG Hoeks. "Reduction of the clutter component in Doppler ultrasound signals based on singular value decomposition: A simulation study." Ultrasonic imaging 19.1 (1997): 1-18.

47. Baranger, Jérôme, et al. "Adaptive spatiotemporal SVD clutter filtering for ultrafast Doppler imaging using similarity of spatial singular vectors." IEEE transactions on medical imaging 37.7 (2018): 1574-1586.

48. Bayat, Mahdi, Mostafa Fatemi, and Azra Alizad. "Background removal and vessel filtering of noncontrast ultrasound images of microvasculature." IEEE Transactions on Biomedical Engineering 66.3 (2018): 831-842.

49. Alberti, Giovanni S., et al. "Mathematical analysis of ultrafast ultrasound imaging." SIAM Journal on Applied Mathematics 77.1 (2017): 1-25.

50. Ghavami, Siavash, et al. "Quantification of morphological features in non-contrast-enhanced ultrasound microvasculature imaging." IEEE Access 8 (2020): 18925-18937.

51. Huang, Lijie, et al. "Improved ultrafast power Doppler imaging by using spatiotemporal non-local means filtering." IEEE Transactions on Ultrasonics, Ferroelectrics, and Frequency Control 69.5 (2022): 1610-1624.

52. Kang, Jinbum, et al. "High-Frequency Ultrasound Imaging With Sub-Nyquist Sampling." IEEE transactions on ultrasonics, ferroelectrics, and frequency control 69.6 (2022): 2001-2009.

53. Guyton, Arthur CMD. Text book of medical physiology. China, 2006.

54. Bentov, Itay, and May J. Reed. "The effect of aging on the cutaneous microvasculature." Microvascular research 100 (2015): 25-31.

55. Christensen-Jeffries, Kirsten, et al. "Super-resolution ultrasound imaging." Ultrasound in medicine & biology 46.4 (2020): 865-891.

56. Gessner RC, Kothadia R, Feingold S, Dayton PA. 3-D Microvessel-mimicking ultrasound phantoms produced with a scanning motion system. Ultrasound Med Biol. 2011 May 1;37(5):827-33.

57. Laughlin ME, Stephens SE, Hestekin JA, Jensen MO. Development of custom wall-less cardiovascular flow phantoms with tissue-mimicking gel. Cardiovasc. Eng. Technol. 2022 Feb;13(1):1-3.

58. Ishii T, Ho CK, Nahas H, Yiu BY, Chee AJ, Yu AC. Deformable phantoms of the prostatic urinary tract for urodynamic investigations. Med Phys. 2019 Jul;46(7):3034-43.

59. Ho CK, Chee AJ, Yiu BY, Tsang AC, Chow KW, Alfred CH. Wall-less flow phantoms with tortuous vascular geometries: Design principles and a patient-specific model fabrication example. IEEE Trans Ultrason Ferroelectr Freq Control. 2016 Dec 6;64(1):25-38.

60. Chee AJ, Ishii T, Yiu BY, Alfred CH. Helical toroid phantom for 3D flow imaging investigations. Phys. Med. Biol. 2021 Feb 11;66(4):045029.

61. Harput S, Christensen-Jeffries K, Ramalli A, Brown J, Zhu J, Zhang G, Leow CH, Toulemonde M, Boni E, Tortoli P, Eckersley RJ. 3-D super-resolution ultrasound imaging with a 2-D sparse array. IEEE transactions on ultrasonics, ferroelectrics, and frequency control. 2019 Sep 25;67(2):269-77.

62. Grand-Perret V, Jacquet JR, Leguerney I, Benatsou B, Grégoire JM, Willoquet G, Bouakaz A, Lassau N, Pitre-Champagnat S. A novel microflow phantom dedicated to ultrasound microvascular measurements. Ultrason Imaging. 2018 Sep;40(5):325-38.

63. Bhatti A, Ishii T, Saijo Y. A Micro-flow Phantom for Superficial Micro-vasculature Imaging. J Phys Conf Ser. 2021 Oct 1 (Vol. 2071, No. 1, p. 012054). IOP Publishing.

64. Meirza B, Hasegawa H, Evertsson M, Sjöstrand S, Cinthio M. Construction of an ultrasound phantom with micrometer-sized wall-less vessels. In 2019 IEEE International Ultrasonics Symposium (IUS) 2019 Oct 6 (pp. 1209-1211). IEEE.

65. Kenwright DA, Laverick N, Anderson T, Moran CM, Hoskins PR. Wall-less flow phantom for high-frequency ultrasound applications. Ultrasound Med Biol. 2015 Mar 1;41(3):890-7.

66. Hindle AJ, Perkins AC. A perfusion phantom for the evaluation of ultrasound contrast agents. Ultrasound in medicine & biology. 1994 Jan 1;20(3):309-14.

67. Pinter SZ, Lacefield JC. Detectability of small blood vessels with high-frequency power Doppler and selection of wall filter cut-off velocity for microvascular imaging. Ultrasound in medicine & biology. 2009 Jul 1;35(7):1217-28.

68. Desailly Y, Pierre J, Couture O, Tanter M. Resolution limits of ultrafast ultrasound localization microscopy. Phys. Med. Biol. 2015 Oct 28;60(22):8723.

69. Kim D, Park SH. A microfluidics-based pulpal arteriole blood flow phantom for validation of doppler ultrasound devices in pulpal blood flow velocity measurement. J Endodo. 2016 Nov 1;42(11):1660-6.

70. Adusei S, Ternifi R, Fatemi M, Alizad A. Custom-made Flow Phantoms for Quantitative Ultrasound Microvessel Imaging. Ultrasonics. 2023 Jun 22:107092.

71. Samavat H, Evans JA. An ideal blood mimicking fluid for doppler ultrasound phantoms. J Med Phys. 2006 Oct;31(4):275.

72. Oglat AA. A review of blood-mimicking fluid properties using doppler ultrasound applications. J Med Ultrasound. 2022 Oct;30(4):251.

73. Chen, Chuan, et al. "In vivo 3D power Doppler imaging using continuous translation and ultrafast ultrasound." *IEEE Transactions on Biomedical Engineering* 69.3 (2021): 1042-1051.

74. Demené, Charlie, et al. "4D microvascular imaging based on ultrafast Doppler tomography." *Neuroimage* 127 (2016): 472-483.

75. Gesnik, Marc, et al. "3D functional ultrasound imaging of the cerebral visual system in rodents." *Neuroimage* 149 (2017): 267-274.

76. Rau, Richard, et al. "3D functional ultrasound imaging of the visual system in the pigeon brain." *2017 IEEE International Ultrasonics Symposium*. IEEE, 2017.

77. Demené, Charlie, et al. "3-D longitudinal imaging of tumor angiogenesis in mice in vivo using ultrafast Doppler tomography." *Ultrasound in Medicine & Biology* 45.5

(2019): 1284-1296.

78. Scholten HJ, Weijers G, de Wild M, Korsten HH, de Korte CL, Bouwman RA. Differences in ultrasound elevational beam width (slice thickness) between popular handheld devices. WFUMB Ultrasound Open. 2023 Dec 1;1(2):100009.

79. Gesnik M, Blaize K, Deffieux T, Gennisson JL, Sahel JA, Fink M, Picaud S, Tanter M. 3D functional ultrasound imaging of the cerebral visual system in rodents. Neuroimage. 2017 Apr 1;149:267-74.

80. Rau R, Kruizinga P, Mastik F, Belau M, de Jong N, Bosch JG, Scheffer W, Maret G. 3D functional ultrasound imaging of pigeons. Neuroimage. 2018 Dec 1;183:469-77.

81. Bhatti, A., Ishii, T., & Saijo, Y. (2020, November). 2Pb5-8 Preliminary Study of Skin Microvasculature Visualization by High Frequency Ultrasound Plane Wave Imaging. In *Proceedings of Symposium on Ultrasonic Electronics* (Vol. 41, pp. 2Pb5-8). Institute for Ultrasonic Elecronics.

82. Provost, J., Papadacci, C., Demene, C., Gennisson, J. L., Tanter, M., & Pernot, M. (2015). 3-D ultrafast Doppler imaging applied to the noninvasive mapping of blood vessels in vivo. *IEEE transactions on ultrasonics, ferroelectrics, and frequency control*, *62*(8), 1467-1472.

83. Correia, M., Provost, J., Tanter, M., & Pernot, M. (2016). 4D ultrafast ultrasound flow imaging: in vivo quantification of arterial volumetric flow rate in a single heartbeat. *Physics in Medicine & Biology*, *61*(23), L48.

84. Alvarez, L., Lions, P. L., & Morel, J. M. (1992). Image selective smoothing and edge detection by nonlinear diffusion. II. *SIAM Journal on numerical analysis*, *29*(3), 845-866.

85. R. Coifman and D. Donoho. Wavelets and Statistics, chapter Translation-invariant de-noising, pages 125-150. Springer Verlag, 1995

86. D. Donoho. De-noising by soft-thresholding. IEEE Transactions on Information

Theory. 41:613-627, 1995.

87. Lindenbaum, M., Fischer, M., & Bruckstein, A. (1994). On Gabor's contribution to image enhancement. *Pattern recognition*, *27*(1), 1-8.

88. C. Tomasi and R. Manduchi. Bilateral filtering for gray and color images. In Proceedings of the Sixth Internatmal Conference on Computer Vision, pages 839-846, 1998.

89. Yaroslavsky, L. P. (2012). *Digital picture processing: an introduction* (Vol. 9). Springer Science & Business Media.

90. Buades, A., Coll, B., & Morel, J. M. (2005, June). A non-local algorithm for image denoising. In *2005 IEEE computer society conference on computer vision and pattern recognition (CVPR'05)* (Vol. 2, pp. 60-65). Ieee.

91. Coupé, P., Hellier, P., Kervrann, C., & Barillot, C. (2009). Nonlocal means-based speckle filtering for ultrasound images. *IEEE transactions on image processing*, *18*(10), 2221-2229.

92. Coupé, P., Yger, P., Prima, S., Hellier, P., Kervrann, C., & Barillot, C. (2008). An optimized blockwise nonlocal means denoising filter for 3-D magnetic resonance images. *IEEE transactions on medical imaging*, *27*(4), 425-441.

93. Zhang, H., Zeng, D., Zhang, H., Wang, J., Liang, Z., & Ma, J. (2017). Applications of nonlocal means algorithm in low-dose X-ray CT image processing and reconstruction: a review. *Medical physics*, *44*(3), 1168-1185.

94. Chan, C., Fulton, R., Barnett, R., Feng, D. D., & Meikle, S. (2013). Postreconstruction nonlocal means filtering of whole-body PET with an anatomical prior. *IEEE Transactions on medical imaging*, *33*(3), 636-650.

95. Yu, H., Gao, J., & Li, A. (2016). Probability-based non-local means filter for speckle noise suppression in optical coherence tomography images. *Optics letters*, *41*(5), 994-997.

96. Buades, A., Coll, B., & Morel, J. M. (2005). A review of image denoising algorithms, with a new one. *Multiscale modeling & simulation*, *4*(2), 490-530.

97. Bao, B. Q., Van Luyen, T., Duong, N. H., & Hieu, T. C. (2019). A novel despeckling approach for ultrasound images using adaptive OBNLM filter. In *Advances in Engineering Research and Application: Proceedings of the International Conference, ICERA 2018* (pp. 77-83). Springer International Publishing.

98. Adabi, S., Ghavami, S., Fatemi, M., & Alizad, A. (2019). Non-local based denoising framework for in vivo contrast-free ultrasound microvessel imaging. *Sensors*, *19*(2), 245.

99. Ghavami, S., Bayat, M., Fatemi, M., & Alizad, A. (2020). Quantification of morphological features in non-contrast-enhanced ultrasound microvasculature imaging. *IEEE Access*, *8*, 18925-18937.

100. Song, P., Trzasko, J. D., Manduca, A., Huang, R., Kadirvel, R., Kallmes, D. F., & Chen, S. (2017). Improved super-resolution ultrasound microvessel imaging with spatiotemporal nonlocal means filtering and bipartite graph-based microbubble tracking. *IEEE transactions on ultrasonics, ferroelectrics, and frequency control*, *65*(2), 149-167.

101. Huang, L., Zhang, J., Wei, X., Jing, L., He, Q., Xie, X., ... & Luo, J. (2022). Improved ultrafast power Doppler imaging by using spatiotemporal non-local means filtering. *IEEE Transactions on Ultrasonics, Ferroelectrics, and Frequency Control*, *69*(5), 1610-1624.

Acknowledgements

First and the foremost, I am thankful to Almighty Allah for giving me courage and strength to complete this important endeavor of my life.

Throughout this thesis dissertation I have received a great deal of support and guidance. I would like to extend my sincere gratitude to my supervisor Professor Yoshifumi Saijo, who helped me to pursue my higher studies in one of the most renowned research institute Tohoku University and accept my candidacy to work in his research group. I highly appreciate all his contributions of time, ideas, funding and continuous support throughout my doctoral studies. Secondly, I am thankful to MEXT scholarship Japan, to support my study financially and provide me an opportunity to continue my research under supervision of Professor Yoshifumi Saijo.

The members of “Saijo’s Lab” have contributed immensely to my research and I am especially grateful to Assistant Professor Takuro Ishii for his support and suggestions throughout my research journey. I really enjoyed working with Assistant Professor Takuro Ishii which makes my research journey quite easy and enjoyable. I learned indispensable lessons about both the scientific research and the life in general. The radiant support and guidance of Prof. Saijo and Assistant Prof. Takuro Ishii and their critical review of my manuscripts has led my research to prolific success that is essential to my professional career. The successful completion of these projects would not have been possible without their immense help. I really enjoyed working at Saijo Lab and learned a lot from everyone.

To my dissertation defense committee, Prof. Yoshifumi Saijo, Prof. Shin Yoshizawa, and Associate Prof. Kenichi Funamoto for their thoughtful questions and valuable comments which helped me to improve my PhD dissertation.

To all the smiling faces of Frontier Research Institute for Interdisciplinary Sciences (FRIS), for providing support of their engineering core facility for designing and 3D printing of micro-vascular 3D models. I am grateful to all the former and present colleagues and members of Saijo’s Laboratory, who have been friendly and helpful throughout my stay at Saijo lab.

To my all Pakistani and other friends in Sendai who became family in a foreign land. In particular I am highly indebted to Ms. Sumeyya Javaid, Dr. Freeha Khalid, Dr. Ahmed Raza, Dr. Hannan Ahmed, Mr. Sikandar Azam, Dr. Shreya Santra and Dr. Shraddha Gupta for always being there in the time of need and arranging gatherings, cooking delicious foods and most importantly never letting me feel alone.

I would like to thank my teachers and mentors Dr. Asad Ali Siyal, Engr. Adeel Mehdi, and Dr. Takuro Ishii who helped me a lot throughout my journey to reach where I am today. Last but not the least I am highly indebted to my loving family, especially to my parents for believing in me, providing endless support and letting me purse my academic goals. To my beloved brother Dr. Junaid Ahmed – the one who ignited the motivation and inspired me to achieve whatever little I have accomplished. To my mother, who supported, nurtured and took great impartial care of all of us, when we lost our father and never let us feel down – words simply cannot express how grateful I am. Without true support and unconditional love and personal sacrifice of my family, I would have never become the individual I am today.

- Anam Bhatti

Tohoku University,
Sendai, Japan
January 2024

Research Achievements

Publications

This research activity has led to several publications in international journals and conferences. These are summarized below.

International Journals:

1. **Bhatti, A.,** Ishii, T., Kanno, N., Ikeda, H., Funamoto, K., & Saijo, Y. (2023). Region-based SVD processing of high-frequency ultrafast ultrasound to visualize cutaneous vascular networks. ***Ultrasonics*****,** *129*, 106907. (**Published**). (Corresponds to Chapter 5).

2. **Bhatti, A.,** Ishii, T., Saijo, Y., Superficial Bifurcated Micro-flow Phantom for High-Frequency Ultrasound Applications, ***Ultrasound in Medicine and Biology,*** 2023 Oct 22. (**Published**). **Featured on the Cover Page of UMB journal Vol. 50(1).** (Corresponds to Chapter 3)

International Conference Papers:

1. **Bhatti, A.,** Ishii, T., & Saijo, Y. (2021, October). A Micro-flow Phantom for Superficial Micro-vasculature Imaging**.** **In** ***Journal of Physics: Conference Series*** (Vol. 2071, No. 1, p. 012054). IOP Publishing. (**Published**). (Corresponds to Chapter 2)

2. **Bhatti, A.,** Kanno, N., Ikeda, H., Ishii, T., & Saijo, Y. (2022, July). Development of an Imaging Framework for Visualization of Cutaneous Micro-Vasculature by using High Frequency Ultrafast Ultrasound Imaging. In *2022 44th Annual International Conference of the* ***IEEE Engineering in***

Medicine & Biology Society (EMBC) (pp. 190-193). IEEE. (**Published**). (Corresponds to Chapter 2)

Domestic Conference Proceedings:

1. **A Bhatti**, N Kanno, H Ikeda, T Ishii, Y Saijo, Visualization of subcutaneous flow tract using SVD filtering of ultrafast high-frequency ultrasound imaging, Proceedings of Symposium on Ultrasonic Electronics, 2021. (Corresponds to Chapter 2).

2. **A Bhatti,** T Ishii, N Kanno, Y Saijo, Visualization of cutaneous micro-vasculatures using SVD-based filtering of ultrafast high-frequency ultrasound, IEICE Technical Report; IEICE Tech. Rep., 2022. (Corresponds to Chapter 5)

3. **A Bhatti,** T Ishii, Y Saijo, Y-shaped Micro-Flow Phantom for Superficial Micro-vessels Imaging: Novel Fabrication Protocol, IEICE – US, Oct. 2023. (Corresponds to Chapter 3)

4. **A Bhatti,** T Ishii, Y Saijo, Volumetric Imaging of Superficial Micro-Vasculature using High-frequency Array Transducer: Phantom Study, UltraSonics Electronics (USE), Nov. 2023. (Corresponds to Chapter 6).

Presentations (International and Domestic)

1. **Anam Bhatti**, "Volumetric Imaging of Superficial Micro-Vasculature using High-frequency Array Transducer: Phantom Study", 44th Symposium on UltraSonics Electronics (USE), Japan, November 2023. (Oral Presentation). (Corresponds to Chapter 6).

2. **Anam Bhatti**, "Y-shaped Micro-Flow Phantom for Superficial Micro-vessels Imaging: Novel Fabrication Protocol", The institute of Electronics, Information and Communication Engineers, Ultrasonic group, IEICE –

US, - Japan, October 2023, (Oral Presentation). (Corresponds to Chapter 3).

3. **Anam Bhatti**, “Imaging of cutaneous vasculature using a novel approach of SVD-based filtering of high-frequency ultrafast ultrasound” - Netherlands – Japan Consortium, Netherlands, Feb 2023. (Oral Presentation). (Corresponds to Chapter 5).

4. **Anam Bhatti**, “Development of Imaging Framework for Visualization of Cutaneous Micro-vasculatures by using High-frequency Ultrafast Ultrasound Imaging” - 44th Annual International Conference of the IEEE Engineering in Medicine and Biology Society (EMBC), Scotland UK, July 2022. (Oral Presentation). (Corresponds to Chapter 2).

5. **Anam Bhatti**, “A micro-flow phantom for Superficial Micro-vasculatures Imaging” - ICoBE International Conference on Biomedical Engineering, Malaysia, September 2021. (Oral Presentation). (Corresponds to Chapter 2).

6. **Anam Bhatti**, “Subcutaneous Micro-vessels Imaging using High-frequency Array Transducer” -18th International Workshop on Biomaterials in Interface Science, Tohoku University, August 2023. (Oral Presentation). (Corresponds to Chapter 4).

7. **Anam Bhatti**, “A novel approach of SVD processing of ultrafast ultrasound to visualize cutaneous vasculatures”, First Collaborative Seminar on Blood Flow Measurements, Tohoku University, Feb 2023. (Oral Presentation). (Corresponds to Chapter 5).

8. **Anam Bhatti**, “Visualization of cutaneous micro-vasculatures using SVD-based filtering of ultrafast high-frequency ultrasound”, The institute of Electronics, Information and Communication Engineers, Ultrasonic group,

IEICE – US, Japan, September 2022. (Oral Presentation). (Corresponds to Chapter 5).

9. **Anam Bhatti,** "Visualization of Peripheral Micro-Vasculatures: A novel imaging modality using high-frequency ultrasound", 158th IDAC Biannual Meeting at Institute of Development, Aging and Cancer, Tohoku University, July 2022. (Oral Presentation). (Corresponds to Chapter 4).

10. **Anam Bhatti,** "Visualization of subcutaneous flow tract using SVD filtering of ultrafast high-frequency ultrasound imaging", 42nd symposium on UltraSonics Electronics (USE), Japan – November 2021, (Poster). (Corresponds to Chapter 2).

International Award:

1. **Best Paper Presenter Award**, A Micro-flow Phantom for Superficial Micro-vasculature Imaging, International Conference on Biomedical Engineering (ICoBE 2021).
2. **Young Scientist Award**, Volumetric Imaging of Superficial Micro-Vasculatures using High-frequency Array Transducer: Phantom Study, 44th Symposium on UltraSonics Electronics (USE 2023).

International Recognition:

1. **Featured on Cover Page** of International Journal "Ultrasound in Medicine and Biology (UMB)", Superficial Bifurcated Micro-flow Phantom for High-frequency Ultrasound Applications, Vol. 50(1), 2024.

Other Publications:

1. Okada, Y., Kanno, N., **Bhatti, A**., Ishii, T., & Saijo, Y. (2023). Robust flow vector estimation for echocardiography with extended Nyquist velocity using dual-PRF approach: a flow phantom study. *Japanese Journal of Applied Physics*, *62*(SJ), SJ1033.

2. Dharejo, F. A., Hao, Z., **Bhatti, A**., Bhatti, M. N., Ahmed, J., & Jatoi, M. A. (2017, October). Improved dictionary learning algorithm with mappings for single image super-resolution. In *2017 IEEE International Conference on Imaging Systems and Techniques (IST)* (pp. 1-6). IEEE.

3. Ahmed, J., Baloch, G. L., **Bhatti, A.**, & Klette, R. (2017, October). Coupled directionally structured dictionaries for single image super-resolution. In *2017 IEEE International Conference on Imaging Systems and Techniques (IST)* (pp. 1-6). IEEE.

4. **Bhatti, A.**, Siyal, A. A., Mehdi, A., Shah, H., Kumar, H., & Bohyo, M. A. (2018, February). Development of cost-effective tele-monitoring system for remote area patients. In *2018 International Conference on Engineering and Emerging Technologies (ICEET)* (pp. 1-7). IEEE.